

# III-Nitride-Based Optochemical Transducers for Gas Detection

Dissertation zur Erlangung des Doktorgrades der Naturwissenschaften (Dr. rer. nat.)  
der Justus-Liebig-Universität Gießen im Fachbereich 07 (Mathematik und Informatik,  
Physik, Geographie)

vorgelegt von

Konrad Maier

Juli 2018

Justus-Liebig-Universität Gießen /

Airbus Group Innovations



## Abstract

Customers of modern airplanes not only demand that manufacturers address more efficient propulsion systems but also pollution created by the overall aircraft system. One way of decreasing pollution is the replacement of kerosene burning auxiliary power units (APU) with hydrogen fuel cells. The usage of fuel cells requires a gas sensor system for safe application in an aircraft, and this can be achieved using a novel gas sensitive InGaN/GaN nanowire arrays (NWA) with an optical read out. These NWAs are investigated in this thesis and exhibit an efficient photoluminescence (PL) which extends to temperatures of 200°C and beyond and show a chemical sensitivity towards gases and liquids. The gas sensing test revealed that InGaN/GaN NWA can have a quenching or an enhancing PL when exposed to different gas atmospheres which depends on both the type of adsorbate and the operation conditions of the transducer. All groups of tested analytes have in common that they can be described using a Langmuir adsorption isotherm. However, the adsorption energy and the response direction is gas species dependent. Oxidizing gases such as O<sub>2</sub>, NO<sub>2</sub> and O<sub>3</sub> quench the PL intensity whereas hydrocarbons, under the certain conditions, can increase the PL. Evaluation of the Langmuir adsorption energy showed an approximately linear increase with temperature in the range from room temperature to 150°C. This phenomenon was attributed to a competitive adsorption process onto a limited number of adsorption sites on the InGaN/GaN surfaces. Hydrocarbons showed an insignificant gas response when these are diluted in nitrogen. However, a PL enhancing effect can be observed when these gases are diluted in synthetic air and this effect is increased at elevated temperatures. This behavior is attributed to an indirect gas sensing process which includes a surface oxidation reaction of the analytes and a removal of PL quenching pre-adsorbed oxygen and formation of combustion products such as CO<sub>2</sub> and H<sub>2</sub>O. CO<sub>2</sub> hardly shows any effect on the PL intensity but H<sub>2</sub>O shows an interesting effect on the PL intensity as it can be of PL quenching and PL enhancing nature depending on the operation conditions. In the low temperature and excitation energy regime water molecules are able to increase the surface recombination process but at elevated temperatures and due to electrochemically dissociated water molecules these recombination channels are passivated and the PL is enhanced.



## Kurzfassung

Auf den Anforderungslisten für moderne Flugzeuge stehen nicht nur effiziente Antriebssysteme, sondern ein möglichst ökologisches Gesamtflugzeugsystem. Eine Möglichkeit, die Umweltverschmutzung zu verringern, ist der Ersatz von kerosinbetriebenen Hilfsaggregaten (APU) durch Wasserstoff-Brennstoffzellen. Der Einsatz von Brennstoffzellen erfordert ein Gassensorsystem für den sicheren Betrieb in einem Flugzeug, was mit einem neuartigen gasempfindlichen InGaN/GaN-Nanodraht-Array (NWA) mit optischer Auslesung erreicht werden kann. Solche NWA, dessen Photolumineszenz (PL) auch bei Temperaturen über 200°C stabil ist und eine Sensitivität gegenüber Gasen und Flüssigkeiten aufweist, wurden im Rahmen dieser Arbeit untersucht. Gassensor-Tests ergaben, dass die PL des InGaN/GaN NWA sowohl verstärkt als auch reduziert werden kann wenn es unterschiedlichen Gasatmosphären ausgesetzt wird, was sowohl von der Art des Adsorbats als auch von den Betriebsbedingungen des Transducers abhängt. Bei allen untersuchten Gasen konnten Langmuir-Adsorptionsisothermen deren Adsorption beschreiben. Die Adsorptionsenergie und die Richtung des Gasresponses sind jedoch von der Art des Gases abhängig. Oxidierende Gase wie  $O_2$ ,  $NO_2$  und  $O_3$  reduzieren die PL-Intensität, während Kohlenwasserstoffe unter bestimmten Bedingungen die PL erhöhen können. Die Auswertung der Langmuir-Adsorptionsenergie ergab einen annähernd linearen Anstieg im Bereich von Raumtemperatur bis 150°C. Dieses Phänomen wurde auf einen konkurrierenden Adsorptionsprozess auf der InGaN/GaN-Oberfläche zurückgeführt. Kohlenwasserstoffe zeigten eine unwesentliche Gasreaktion wenn diese in Stickstoffhintergrund gemessen wurden. Ein PL-verstärkender Effekt kann jedoch beobachtet werden, wenn diese Gase in synthetischer Luft gemischt werden und dieser Effekt wurde bei erhöhten Temperaturen noch weiter verstärkt. Dieses Verhalten wird einem indirekten Gasdetektionsprozess zugeschrieben, der eine Oberflächenoxidationsreaktion der Analyten mit einer Verdrängung von adsorbiertem Sauerstoff und der Bildung von Verbrennungsprodukten wie  $CO_2$  und  $H_2O$  beinhaltet.  $CO_2$  hat kaum einen Einfluss auf die PL, aber  $H_2O$  zeigt einen interessanten Einfluss auf die PL-Intensität, da es je nach Betriebsbedingungen der NWA von PL-reduzierender als auch PL-verstärkender Natur sein kann. Im Niedrigtemperatur- und Anregungsenergiebereich sind Wassermole-

küle in der Lage, den Oberflächenrekombinationsprozess zu verstärken, aber bei erhöhten Temperaturen und durch elektrochemisch-dissoziierte Wassermoleküle werden diese Rekombinationskanäle passiviert und die PL erhöht.

---

## List of publications

### III-nitride based gas sensor related research:

#### Journals:

- [i] K. Maier, A. Helwig, G. Müller, P. Becker, P. Hille, J. Schörmann, J. Teubert, M. Eickhoff, Detection of oxidising gases using an optochemical sensor system based on GaN/InGaN nanowires, *Sensors Actuators B Chem.* 197 (2014) 87–94. doi:10.1016/j.snb.2014.02.002.
- [ii] K. Maier, A. Helwig, G. Müller, P. Hille, J. Teubert, M. Eickhoff, Photoluminescence Probing of Complex H<sub>2</sub>O Adsorption on InGaN/GaN Nanowires, *Nano Lett.* 17 (2017) 615–621. doi:10.1021/acs.nanolett.6b03299.
- [iii] K. Maier, A. Helwig, G. Müller, P. Hille, J. Teubert, M. Eickhoff, Competitive adsorption of air constituents as observed on InGaN/GaN nano-optical probes, *Sensors Actuators B Chem.* 250 (2017) 91–99. doi:10.1016/j.snb.2017.04.098.
- [iv] K. Maier, A. Helwig, G. Müller, M. Eickhoff, Photoluminescence detection of surface oxidation processes on InGaN/GaN nanowire arrays, *ACS Sensors.* (2018) doi:10.1021/acssensors.8b00417

#### Book chapter:

- [v] K. Maier, A. Helwig, G. Müller, M. Eickhoff, Luminescence Probing of Adsorption Processes Using InGaN/GaN Heterostructure Nanowire Arrays, in: J. Raivo, T.O. Kiang (Eds.), *Semicond. Gas Sensors*, 2nd ed., Woodhead Publishing. (submitted 2018).

#### Conferences:

- [vi] S. Paul, K. Maier, A. Das, F. Furtmayr, A. Helwig, J. Teubert, E. Monroy, G. Müller, M. Eickhoff, III-nitride nanostructures for optical gas detection and pH sensing, in: T. George, M.S. Islam, A.K. Dutta (Eds.), *SPIE Defense, Secur. Sens.*, International Society for Optics and Photonics, 2013: p. 87250K. doi:10.1117/12.2015221

**Other gas sensor related research:**

- [vii] K. Maier, A. Helwig, G. Müller, P. Hille, M. Eickhoff, Effect of Water Vapor and Surface Morphology on the Low Temperature Response of Metal Oxide Semiconductor Gas Sensors, *Materials (Basel)*. 8 (2015) 6570–6588. doi:10.3390/ma8095323.
- [viii] K. Maier, A. Helwig, G. Müller, Room-temperature dosimeter-type gas sensors with periodic reset, *Sensors Actuators B Chem.* 244 (2017) 701–708. doi:http://dx.doi.org/10.1016/j.snb.2016.12.119.
- [ix] K. Maier, A. Helwig, G. Müller, Towards MEMS Pellistor Spectrometers, *Procedia Eng.* 120 (2015) 142–145. doi:10.1016/j.proeng.2015.08.587.
- [x] M. Hardy, M.D. Doherty, I. Krstev, K. Maier, T. Möller, G. Müller, P. Dawson, Detection of low-concentration contaminants in solution by exploiting chemical derivatization in surface-enhanced Raman spectroscopy., *Anal. Chem.* 86 (2014) 9006–12. doi:10.1021/ac5014095.
- [xi] B. Bouxin, K. Maier, A. Hackner, G. Müller, F. Shao, J.D. Prades, F. Hernandez-Ramirez, J.R. Morante, On-chip fabrication of surface ionisation gas sensors, *Sensors Actuators B Chem.* 182 (2013) 25–30. doi:10.1016/j.snb.2013.02.049.
- [xii] L. Müller, K. Maier, A. Hellwig, M. Hoffmann, Low temperature catalytic combustible hydrogen MEMS gas sensor enhanced by Si-Pt nanostructures, in: 41th Int. Conf. Micro- Nano Eng., The Hague, 2015.

---

# Content

1	Introduction.....	1
1.1	Semiconductor gas sensors.....	2
1.2	History of III-nitrides: from research subject to mature technology.....	4
1.3	III-nitride materials: suitability for gas sensors with optical readout .....	5
1.4	Motivation for this work .....	7
1.5	Outline of the thesis.....	9
2	Physical basics.....	11
2.1	Basics of InGaN/GaN nanowire ensembles .....	11
2.1.1	General properties of Gallium Nitride.....	11
2.1.2	General properties of Indium Nitride.....	13
2.1.3	Polarization effects of III-nitrides .....	14
2.1.4	Semiconductor surfaces.....	18
2.1.5	Space charge layers at semiconductor surfaces.....	21
2.2	Basics of adsorption .....	25
2.2.1	Physisorption .....	26
2.2.2	Chemisorption .....	28
2.2.3	Main laws of adsorption .....	29
2.2.4	Multilayer Adsorption .....	34
2.2.5	Competitive adsorption .....	38
3	Materials preparation and functional assessment .....	41
3.1	Gas test rig.....	41
3.2	InGaN/GaN optical probing .....	45
3.2.1	InGaN/GaN nanowire transducer.....	45
3.2.2	PL sensor setups .....	50
4	Gas response of GaN/InGaN nano-optical probes .....	55

4.1	General response behaviour .....	55
4.2	Response to oxidizing gases .....	58
4.2.1	O <sub>2</sub> response .....	58
4.2.2	NO <sub>2</sub> response .....	60
4.2.3	O <sub>3</sub> response .....	61
4.3	Response to reducing gases .....	62
4.3.1	Alcohol response.....	62
4.3.2	Aliphatic hydrocarbons.....	64
4.3.3	General observation of the hydrocarbon response.....	65
4.4	Response to H <sub>2</sub> O vapour.....	67
5	Analysis of the adsorption phenomena.....	73
5.1	Concentration- and temperature dependence of the PL response.....	73
5.2	Competitive adsorption of air constituents on III-nitride surfaces.....	78
5.2.1	Two component Langmuir adsorption on III-nitride surfaces.....	80
5.3	Complex H <sub>2</sub> O adsorption.....	85
5.3.1	Competitive water adsorption model .....	86
5.3.2	Data fitting.....	88
6	Molecular mechanism of adsorption.....	91
6.1	Recombination and adsorption at non-polar III-nitride surfaces.....	91
6.2	Water adsorption at III-nitride surfaces.....	95
6.3	Surface oxidation processes and hydrocarbon response .....	99
6.4	Modelling the chemical sensitivity of InGaN/GaN nanowires.....	102
6.4.1	Qualitative considerations.....	103
6.4.2	Governing equations of the recombination model .....	106
6.4.3	Non-radiative recombination through intrinsic surface sites .....	107
6.4.4	Adsorbate effects on surface recombination .....	109

---

6.4.5	Steady-state solutions.....	110
6.4.6	Comparison to experiment.....	113
6.4.7	Adsorbate effects on photo-luminescence .....	115
7	Summary and Outlook.....	119
7.1	Summary.....	119
7.2	Outlook .....	122
7.2.1	Multifunctional fuel cell application in aircrafts.....	122
7.2.2	Further investigations .....	126
	Bibliography .....	129
	Danksagung.....	141
	Erklärung .....	143



# 1 Introduction

Like most technical inventions, gas sensors and chemical sensors derive their inspiration from nature. Gas sensing, or in nature better called smelling or olfaction, is a sense which many animals have and which is vital for their survival. This sense helps to find food, to detect predators, to find a suitable partner and many more. Even in the world of plants, smelling of odours is important for survival. On the one hand, plant scents, especially those of flowers, attract insects in order to distribute their seeds or pollen. On the other hand, they can use their scents actively to discriminate foreign pollen from their own ones. In this way, they can influence their reproduction behaviour to either promote diversity of their genes or to find a good match to their own ones. In general, basic forms of smelling or olfaction can be found in almost every living organism as chemical signals control many processes ensuring their reproduction or their survival. [1]

In order to make use of the information contained in odours, nature's creatures have developed different implementations of devices, capable of accessing this kind of information. In all cases the detectors in animals and humans employ sensors that make use of bio-chemical interactions of odour molecules with some kind of sensitive surface. These interaction processes are very complex and are not yet fully understood.

Like every other human sense, olfaction is mirrored in some form within our technical and industrial world. But smelling in nature is a rather complicated process and very difficult to copy in our technical world. There are multiple ways of identifying molecules. One possibility is measuring a physical quantity, as for instance a molecular mass or a light frequency, which is more or less uniquely associated with the chemical substance to be detected. Another possibility of assessing a molecule's identity is gathering chemical information by finding out how an unknown substance reacts

with a known substance. In many devices it is a combination of multiple measurements of different physical and chemical quantities in order to identify a substance. In any way, the task of smelling and of identifying certain analytes is so complex that there is not any single universal device that would serve all possible applications. As a consequence, there are very specialized devices, custom-designed to fulfil particular application needs. The most challenging problem in gas sensing is that there is an almost infinite number of cross contaminants that can potentially influence the output signals of gas sensors. In spite of strong efforts of developing better technical smelling devices, most of them fail to live up to nature's high performing olfactory systems. The most prominent example is sniffer dogs, employed by police forces around the world. So far, these could not be completely substituted by technical equipment. Also in the field of food control or food tasting, the human nose is the device of choice that could not yet be replaced by man-made technology. Nevertheless, both human and dog olfactory senses suffer from drawbacks, which call for technical implementations of the natural olfactory senses. These drawbacks are: limited attention span, highly subjective answers to identical chemical scents, and ensuing problems of performing repeatable tests. Many applications, in addition, call for technical solutions because these impose severe constraints with regard to time, space and cost. As a consequence, there is a big demand for technical solutions for detecting odours in a vast variety of applications.

## 1.1 Semiconductor gas sensors

Benchmark systems for detecting gases are many forms of laboratory equipment. Examples are mass-spectrometers (MS), gas chromatographs (GC), or Fourier transform infrared (FTIR) spectrometers. These systems feature large size, are expensive and require trained personal for operation. In contrast, practical applications in industrial or domestic environments require small-size, stand-alone devices, which do not require operator attention. In order to arrive at such devices, semiconductor materials and semiconductor technologies are being employed.

In electronics, silicon semiconductor devices have replaced the bulky and energy-consuming vacuum tubes of the radio equipment of the 1950ies and before [2]. The rapid

miniaturisation of transistors and their integration into silicon (Si) microchips, in particular, has not only replaced vacuum tubes. Most importantly, it has hugely boosted our capabilities in data processing, and thus laid the foundation for the digitalisation of our industries and our daily lives. Silicon technology has also greatly contributed to the evolution of sensor technologies. Prominent examples are the motion sensing devices widely used in cars, mobile phones and tablet computers [3,4]. Another important example is digital camera chips [5,6]. Whereas these latter forms of physical sensors have developed close to their physical performance limits, the development of chemical and gas sensors still continues to be a very active field of research.

Table 1.1 lists different types of solid state gas sensors that have emerged from such efforts. Many of these, however, have not yet reached a level of perfection and cost efficiency comparable to silicon devices. A widely used kind of low-cost gas sensors employs metal oxides (MOX) as gas sensitive materials. Such devices consist of screen-printed MOX layers which change their resistivity when the oxide surfaces react with contaminants in the ambient air. These sensors are highly sensitive, but lack in selectivity. Additionally, their operation requires high temperatures, some over 500°C [7], to reach full sensory performance. Better performing, but far more complex devices are sensors which involve spectroscopic measurement principles. Examples are dispersive and non-dispersive infrared (IR) adsorption or photo acoustic (PA) spectrometers. For a long time, such devices used to be very big, putting them into the category of laboratory analytical equipment. Lately, MEMS (micro-electro-mechanical systems) technologies have started to shrink such devices into tiny, low-cost devices, capable of in-field use [8–11]. Optical gas sensor systems become more and more suitable for high volume applications as light sources in the form of light emitting (LED) or laser diodes are becoming cheaper and as their emission spectra widen. A sensor principle, which will be the topic of this work and which profits from the COTS (commercial off-the-shelf) availability of optical components, are photoluminescence (PL) based gas sensors. Because of the well-separated excitation and emission spectra of the semiconductor transducers in these kinds of sensors, relatively simplistic optical setups can be used. The transducer materials used are pieces of nano-structured III-nitride semiconductors, i.e. materials whose family is in the focus of current research.

Table 1.1. Important types of solid state gas sensors and measured physical output parameters [12]

Type		Physical quantity
1	Semiconducting metal oxides	Electrical conductivity
2	Field effect gas sensors: diodes, transistors, capacitors	Work function
3	Piezoelectric sensors: Quartz crystal microbalances (QMB), surface acoustic wave (SAW), microcantilevers	mass
4	Optical sensors	Optical parameters: reflection, interferometry, absorption, fluorescence, refractive index or optical path length
5	Catalytic gas sensors: Seebeck effect, pellistors, semistors	Heat or temperature
6	Electrochemical gas sensors (potentiometric or amperometric)	Voltage or current in an electrochemical cell

## 1.2 History of III-nitrides: from research subject to mature technology

Nitride materials, such as gallium nitride (GaN) and its alloys with indium nitride (InN) and aluminium nitride (AlN), are rapidly developing into a semiconductor technology that is similarly mature like silicon, thus becoming enablers for devices and device applications which are inaccessible to the silicon technology. The main advantage of GaN and its alloys over silicon is that these are direct-bandgap semiconductors with a built-in polarization that makes them applicable in the fields of high temperature, high power electronics and opto-electronics. III-nitride semiconductors

have been studied intensively during the past decades. Because of their enormous potential it is expected that III-nitride technologies will undergo similar development efforts as it has been the case for crystalline silicon which is now the basis for the whole industry of micro-electronics and information technology.

The first promising research successes date back to some 50 years ago where first works on GaN based transistors were published [13]. As GaN materials have to be produced via epitaxial growth processes, appropriate substrates are mandatory. As bulk GaN crystals were not available then, the progress of research on GaN was very slow in the beginning. It was only in the 1980s that the nitride material science rapidly progressed as these materials could then be grown on sapphire substrates using GaN and AlN as nucleation layers [14,15]. In the 1990-ties p-type GaN was discovered using magnesium as a dopant [16]. Some years later, after high quality GaN films could be manufactured, the successful commercialization of GaN devices set in. GaN based light emitting (LED) and laser diodes found their way into consumer products such as Blue Ray discs and lighting bulbs. The inventors of high efficient GaN based LEDs were rewarded with the Nobel prize in 2014 [17]. Other successful products were high-electron-mobility transistors (HEMT) for high frequency applications [18].

III-nitride heterostructures, combining different III-nitride alloys were first successfully implemented in thin film devices such as LEDs or HEMTs. Recent developments in the epitaxial growth of III-nitride alloys go into the direction of nano-structured materials. Since the first successful attempts of molecular beam epitaxy of nanometre sized columns of III-nitrides on silicon substrates in 1998 [19,20] much progress has been made in terms of crystal quality, structural perfection and electronic properties [21–23].

### 1.3 III-nitride materials: suitability for gas sensors with optical readout

Besides their potential in high frequency, high power electronics and lighting applications, GaN based materials also have some properties that make them suitable as

transducer materials in gas sensors. Gas sensors can be found in all kinds of applications, ranging from industrial usage to automotive and domestic applications. As the operating requirements for gas sensors are in general quite harsh, gas sensor materials need not only to be gas-sensitive but also chemically resistant in their particular application environments and stable over prolonged periods of time.

As GaN is chemically inert with regard to most substances and as it is also temperature stable, GaN based sensors satisfy the first selection criterion of stability [24].

As the bulk properties of GaN and its alloys are sensitive to the physical and chemical interactions at their surfaces, GaN-based sensors also satisfy the second criterion of gas sensitivity [25–27].

Further, as GaN and its alloys are epitaxially grown on foreign substrates, it is possible to grow small columns of GaN and/or InGaN with diameters less than 100 nm. These columns stand close together, forming dense nanowire arrays (NWA) with surface-to-volume ratios several orders of magnitude larger than thin, flat films. GaN-based NWAs therefore potentially offer high levels of gas sensitivity.

Additionally, GaN is a direct-bandgap semiconductor, it is ideally suited for building opto-electronic devices. Focussing on applications in the field of gas sensors, a key observation was that GaN-based NWAs possess a photo-luminescence that can firstly be excited by commercial ultra-violet LEDs and that, secondly, the intensity of the resulting longer-wavelength luminescence light proved to be sensitive to the chemical environments in which the NWAs are operated. Although GaN-devices in the form of gas sensitive field effect transistors have already shown excellent gas sensing performance [26–29]. NWA-sensors offer additional advantages: due to the optical read out, a media separation between the chemical environment to be monitored and the sensor optics and electronics can be attained [30,31]. Such a media separation is a key advantage when the sensors are to be operated in harsh environments or in explosive gas atmospheres. As will be shown in the following, such media separation can be attained either through optically transparent sapphire substrates or through mechanically and chemically resistant optical fibres.

## 1.4 Motivation for this work

Air pollution is nowadays an omnipresent topic and since the Volkswagen Diesel engine scandal in 2015, which has now reached many other car manufactures, an increasing reduction of pollution is demanded both by the general public and by politics. Combustion engines in general produce two main environmentally problematic gases: one is  $\text{CO}_2$  which is a greenhouse gas that is accelerating the climate change, and secondly nitrous oxides (mainly  $\text{NO}$  and  $\text{NO}_2$ ) which are by-products of combustion processes formed at high temperatures and high pressures in oxygen-rich atmospheres. The latter gas is poisonous for humans and responsible for many kinds of illnesses and premature deaths. As a consequence, alternative propulsion technologies are required in the long run.

A topic not so much in the current focus is that air pollution is not only produced by cars and trucks but also by aircrafts both during travel in air as well as during taxiing on ground. A possible solution to this problem are all-electric aircrafts with hydrogen-powered fuel cells [32]. A more near-term approach towards more-electric aircrafts is replacing the auxiliary power units (APU) in conventional jet airplanes. APUs generate all the electrical power that is needed inside the aircraft. The electrically powered subsystems include a lot of electrical and electronic systems as well as the hydraulic system with all its hydraulic and pneumatic pumps. In the current state of the art, APUs are powered by conventional combustion engines which use kerosene as fuel.

Currently Airbus is working on fuel cell based APUs that are supposed to replace the conventional combustion based APUs. Such fuel cell-based systems offer several important advantages over conventional ones:

- (i) Fuel-cells, like conventional APUs, firstly generate all the electricity that is needed on board. As a by-product, fuel cells produce at their exhaust gas outlets reaction water and air that is severely oxygen-depleted.
- (ii) The produced water can be used as an on-board water supply, thereby obviating the necessity of taking on-board drinking water supplies which contribute one to three additional tons to the take-off weight of current airliners.

- (iii) The oxygen-depleted exhaust gas, thirdly, can be used to fill the airspace in the kerosene tanks that develops as jet fuel is consumed. Such inertisation is necessary to inhibit the formation of potentially explosive air-fuel gas mixtures in the kerosene tanks. Currently, this safety functionality is provided by pressurized  $N_2$  cylinders, which again contribute additional take-off weight.

In brief: fuel-cell APUs provide three important resources inside airplanes starting from the single and unavoidable resource kerosene. Fuel cell APUs thus promise technically less complex airplanes with a lower take-off weight and concomitantly higher payload potential.

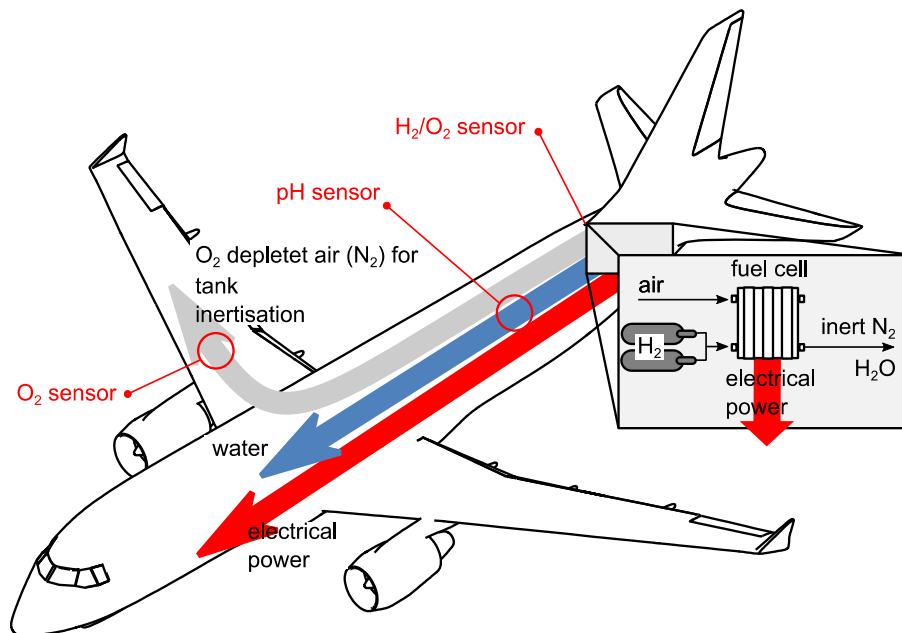


Figure 1.1. Aircraft application of a multifunctional fuel cell replacing the auxiliary power unit (APU). Potential applications for III-nitride based opto-chemical sensors are indicated in red.

For a safe operation of such fuel cell APUs, gas and liquid sensors are required to monitor and to ensure their proper operation. Monitoring requirements arise both at the inlet and outlet sections of the fuel cell:

- (i)  $H_2/O_2/N_2$  ratio at the fuel cell input
- (ii)  $O_2/N_2$  ratio in the fuel cell output

(iii) pH value in the output reaction water

The specific challenges in addressing these sensor applications are that measurements (i) and (ii) need to be performed in potentially explosive atmospheres. Measurement (iii) requires the sensors to be operated in potentially corrosive liquid environments. Apart from these specific challenges, non-specific challenges are met which need to be taken care of in every kind of sensor application. These non-specific challenges, in particular, relate to temperature and pressure changes in the sensor environment. As the temperature and pressure levels inside non-pressurized airplane compartments may change far more than in automobiles, the fuel cell sensors need to be able to work in extremely challenging environments.

Building on the potential of media separation, it was decided to seriously consider III-nitride based opto-chemical sensors for the above measurement challenges. In previous projects III-nitride based materials had proven to be suitable for oxygen sensing and when coated with a thin layer of platinum they also showed sensitivity towards hydrogen [31,33–35]. Although there had been promising research progress into this direction, many aspects of the sensing mechanism using of III-nitride materials and also their cross sensitivities still remained unclear.

## 1.5 Outline of the thesis

This thesis, consequently, aims at a more fundamental understanding of those surface processes that underlie the gas sensing operation of III-nitride based materials. For this reason different categories of test gases and measurement conditions were applied to III-nitride based opto-chemical transducers to unveil their surface reactions and sensing mechanisms.

Surface science offers a variety of measurement tools for analysing transducer surfaces. Typical examples are X-ray diffraction (XRD), low energy electron diffraction (LEED), X-ray and ultra-violet photo electron spectroscopy (XPS and UPS) among others. Unfortunately, these tools all need to be operated under idealised laboratory conditions and some of them even require vacuum conditions. In contrast, recent research on metal oxide gas sensors has shown that problems of sensor physics are best

treated using methods of “operando spectroscopy” which work under conditions as close to normal sensor operating conditions as possible [36]. Following this approach, InGaN/GaN transducers were operated under real life condition using a custom designed gas test rig and custom-designed opto-chemical setups.

In chapter 2 the most important physical concepts will be presented, that are relevant for the experiments carried out in this theses. Starting point is the basic semiconductor physics of III-nitride materials, particularly their bulk electronic and optical properties. Trying to build a bridge towards gas sensor applications, we turn to the physics of surfaces and to defects on surfaces. Finally, we take a detailed look at the adsorption of foreign species on semiconductor surfaces.

The third chapter deals with the experimental details of this thesis. The topics discussed there range from details related to the semiconductor transducers provided by the University of Gießen to the gas sensing equipment and the gas sensing tests that had been performed at the laboratories of AIRBUS GROUP INNOVATION at Ottonbrunn.

In the following chapters the experimental results are presented and discussed. These chapters also deal with the development of adsorption models that try to relate the observed changes in PL intensity to the electronic configurations of the adsorbates on the InGaN sensor surfaces.

The final chapter summarizes the conclusions that can be drawn from the present work and it also presents a short outlook and suggestions for follow-on work in this field.

## 2 Physical basics

In this chapter the basic physics of gas sensitive opto-chemical transducers are summarized. First, the semiconductor fundamentals of InGaN/GaN nanowires are briefly presented including electrical and optical properties of GaN and InN. References among others are standard literature of semiconductors [37–39] and those of III-nitride materials [40,41]. The second part of this chapter will cover the basics of gas adsorption on surfaces. Here, surface science textbooks are used as reference [42,43]. Both topics, semiconductor physics and adsorption, are the fundamental building blocks of semiconductor gas sensor physics.

### 2.1 Basics of InGaN/GaN nanowire ensembles

#### 2.1.1 General properties of Gallium Nitride

Gallium nitride is a III-V semiconductor with a bandgap of  $E_G = 3.39$  eV at room temperature and a subject of research since the 1970s. The fact that GaN is a direct bandgap semiconductor and that its bandgap is large enough to emit light in the near ultra violet (NUV) spectrum, made GaN the main building block of nowadays light-emitting devices (LED). As UV light can be converted into longer-wavelength light through conversion layers, modern LEDs are able to emit visible radiation with a daylight-like spectrum.

Nominally undoped GaN is an n-type semiconductor due to naturally occurring oxygen and silicon impurities [44,45]. Current research tries to intentionally dope GaN in order to improve its optical and electrical properties. N-type doping can be achieved using silicon (Si) which forms a donor level with a binding energy of  $\sim 30$  meV [46] below the conduction band. More recently, germanium (Ge) is used for n-type doping

which cause less degradation of the material at higher doping concentrations [47,48]. P-type doping is possible using magnesium (Mg) which forms an acceptor level  $\sim 200$  meV above the valence band [49].

## GaN crystal structure

GaN can form three different types of crystal lattices: sodium chloride, zincblende ( $\beta$ -phase) and wurtzite structures ( $\alpha$ -phase) [40,41]. The latter, wurtzite, is the most common and thermodynamically most stable phase and this structure is also realized in the GaN nanowires used in this work. The wurtzite crystal structure is part of the hexagonal crystal system. In Figure 2.1 (a) GaN in the wurtzite structure is shown with the red lines indicating the hexagonal lattice structure.

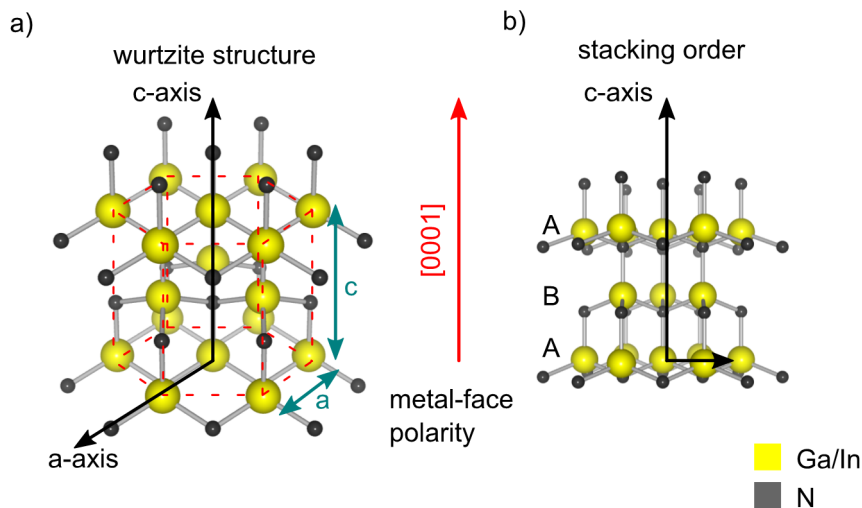


Figure 2.1. (a) Wurtzite crystal structure of gallium nitride (GaN) and indium nitride (InN). Each Ga/In-atom is surrounded by four N-atoms forming tetrahedrons with a central Ga atom. Likewise, each N-atom is tetrahedrally surrounded by four Ga-Atoms. (b) the stacking order of GaN/InGaN is alternating between two planes (ABABAB)

Each gallium atom has 4 nitrogen atoms as nearest neighbours, forming a tetrahedron. The same is valid when one starts from a nitrogen atom. When looking along the c-axis, the layers are alternating between gallium and nitrogen, forming an *ABAB*... stacking sequence, which is depicted in Figure 2.1 (b). The letter *A* indicates a layer with gallium and nitrogen on top which is followed by a similar layer but shifted in the lateral direction which is denoted as layer *B*.

The lattice constant of GaN in the wurtzite configuration along the a-axis is approx. 3.18 Å, and approx. 5.18 Å along the c-axis. As gallium nitride substrates are not yet available for homo-epitaxial growth, substrates with similar lattice constants are desirable. Today mostly silicon Si(111) substrates are employed which exhibit a lattice mismatch of 17 % to GaN. These large lattice mismatches and differences in thermal expansion coefficients induce undesirable crystallographic defects e.g. dislocations. A poor crystal quality is often the reason for the unintentional n-type conduction of gallium nitride.

Once crystallized, gallium nitride is a very stable material with a melting point of approx. 2500 °C, which makes it perfectly suited for high temperature applications.

Additionally, it is chemically highly inert which makes it also applicable in the field of chemical or gas sensors.

### Electronic and optical properties of GaN

GaN, like many III-V semiconductor materials, is a direct-bandgap semiconductor, which promotes optical transitions. GaN optical devices therefore show superior performance as demonstrated by the latest LED consumer product developments. The energy range of emitted photons extends from ultraviolet (UV) to red. Since a number of years, LEDs and lasers emitting in this energy range are commercially available.

Besides the application in optoelectronics, GaN is a very useful material in the field of high-power electronics. There are two reasons for its usage in this field. First, GaN has a very good heat conductivity (1.3 W/cm K) which is essential for power electronics where a large amount of energy is dissipated inside the electronic components. The second reason is that GaN has a high dielectric strength (breakdown field: 5 MV/cm). GaN has already been used in high performance transistors and high-performance applications for a longer time.

#### 2.1.2 General properties of Indium Nitride

Compared to GaN, the properties of Indium nitride (InN) are not that well characterized. The most striking difference to GaN is its small bandgap of only 0.7 eV. Much of the current research is concerned with the preparation of high-purity crystals.

## Crystal structure of InN

The crystal structure of InN is similar to that of GaN, with a wurtzite structure forming its most stable phase (see Figure 2.1 (a) and (b)). It can also crystallize in a zinc blende structure but as the wurtzite phase is the most stable and hence relevant in this work. When using silicon Si(111) as a growth substrate, a lattice mismatch of 8 % has to be tolerated. When growing InN the substrate temperature needs to be much lower than in GaN crystal growth ( $T_s \sim 475$  °C). When higher temperatures are used, the InN dissociates which renders its growth impossible.

## Electronic and optical properties of InN

Until recently the bandgap value of 0.7 eV of InN was hard to determine as it was and as it is still very difficult to produce pristine and defect-free InN crystals. In combination with the wider-bandgap materials of GaN ( $E_g = 3.4$  eV) and aluminium nitride (AlN), ( $E_g = 6.2$  eV), the family of III-nitride materials covers the whole light spectrum from the near infrared (NIR) up into the far ultraviolet (FUV) range.

InN exhibits an extraordinarily high electron mobility of approx.  $3200 \text{ cm}^2\text{V}^{-1}\text{s}^{-1}$  which would enable its use in high-performance electronic components. However, many technical obstacles still need to be overcome before this potential can be realized. In particular, lattice defects need to be removed and methods for p-type doping need to be established.

The most striking property of InN is a surface electron accumulation layer [50,51] which results in a downward band bending.

### 2.1.3 Polarization effects of III-nitrides

III-nitride materials with a wurtzite crystal structure exhibit large internal polarization effects which have a strong impact on their electrical and optical properties. The reason for this internal polarisation is the large difference in electronegativity of the gallium/indium and nitrogen atoms. Three types of polarization can be distinguished: spontaneous-, piezo- and pyro-electric polarization. The common reason for all these polarisation effects is that all originate from deviations of the ideal tetrahedral bond angles inside III-nitride materials.

In an ideal tetrahedron the covalent bonds to nearest neighbours have an angle of  $109.49^\circ$  in between neighbouring bonds and the projections of the polarisation vectors for each pair of Ga-N bonds add up to zero as indicated in Figure 2.2 (a). Due to the finite difference in electronegativity between N, on the one hand, and Ga and In, on the other hand, a complete transfer of valence charges between N and Ga or In atoms does not take place in real-life GaN or InN crystals. Further, the electrostatic forces acting between neighbouring lattice constituents put strain on the nearest-neighbour bonds. While there is compressive strain on the top vertical bond pointing along the c-axis, the c-axis components of the local electrical fields put bending strain on the back-bonds at the bottom, which point away from the c-axis. As chemical bonds are more easily bent than becoming compressed, the overall effect of the local electrical fields on the basic tetrahedron is a slight distortion of the bond angles at the back bonds as shown in Figure 2.2 (b). In such a distorted situation, the projections of the four polarisation vectors on the c-axis do no longer add up to zero and a finite spontaneous polarisation occurs.

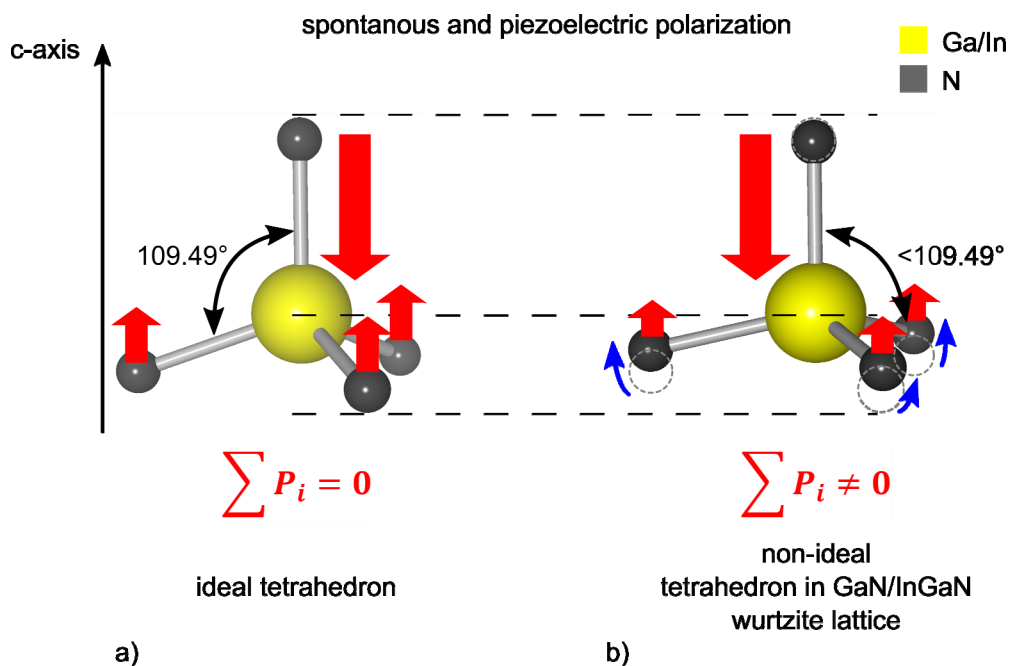


Figure 2.2. (a) In the ideal tetrahedron the projections of the polarization vectors along the c-axis add up to zero; (b) in a real-life GaN crystal the electrostatic forces acting between the lattice constituents deform the basic tetrahedral. In such a distorted situation a net finite polarisation remains.

Of course, the magnitude of this spontaneous polarisation will change when external fields or mechanical stress are additionally applied. The latter effect is called piezoelectric effect and when strain is induced by thermal expansions the piezoelectric effect is called pyroelectric effect.

The polarization effect only occurs if the crystal symmetry is not too high. This is true for the wurtzite structure, but here, the polarization effect can only be found along the  $c$ -axis and crystal planes perpendicular to this axis are polar. Planes parallel to the  $c$ -axis are non-polar. In Figure 2.3 the most important planes of wurtzite GaN or InN are shown. In this thesis, adsorption effects on III-nitride nanowires are studied and it is assumed that most analytes adsorb on the non-polar side walls.

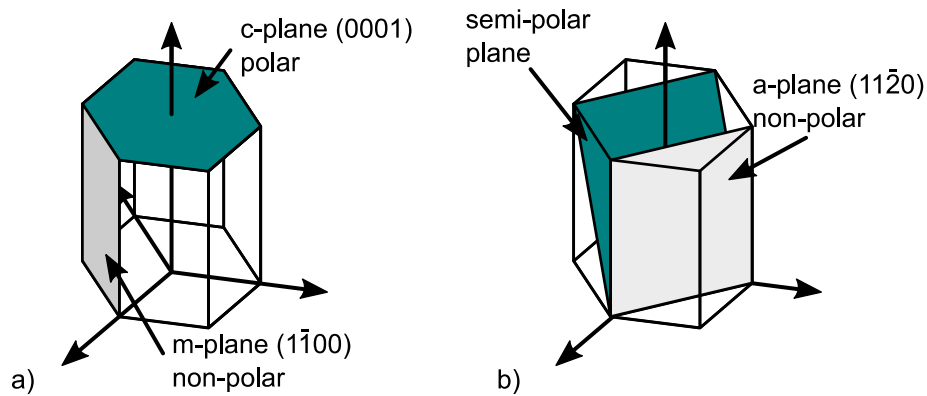


Figure 2.3. Important directions and planes of GaN wurtzite based structures (a) top  $c$ -plane showing polar properties and side  $m$ -planes with non-polar properties. (b) inside the hexagonal block is the polar  $a$ -plane and when semi-polar plane which is neither purely polar nor purely non-polar

When building heterostructures of GaN and InGaN along the  $c$ -axis, the lattice mismatch induces internal electric fields. These fields lead to effects on the band structure such as the quantum-confined Stark (QCSE) effect which is briefly discussed in the next section.

### Carrier confinement and quantum-confined Stark effect (QCSE)

The effect of polarisation on charge carriers in heterostructures is illustrated in Figure 2.4. When considering a direction where the polarization is negligible the band

profile of the heterostructure is built up from the individual semiconductor band profile resulting in a potential well which increases the electron hole pair density in the InGaN layer after photo-excitation. This accumulation process of charge carriers is called carrier confinement as shown in Figure 2.4 (a). Due to the spatial confinement of electron-hole pairs an efficient radiative recombination can be achieved. When considering an InGaN/GaN heterojunction in combination with its internal electric fields (spontaneous and piezoelectric polarization fields) the band profile is tilted, electrons and holes are shifted in opposite directions, thereby attaining a state of lower energy. As electron-hole-pairs are spatially separated, the recombination probability is decreased. This phenomenon is shown in Figure 2.4 (b) and called quantum-confined Stark effect (QCSE). Besides a reduced oscillator length, the QCSE also gives rise to a redshift as the effective energy gap between electrons and holes is reduced.

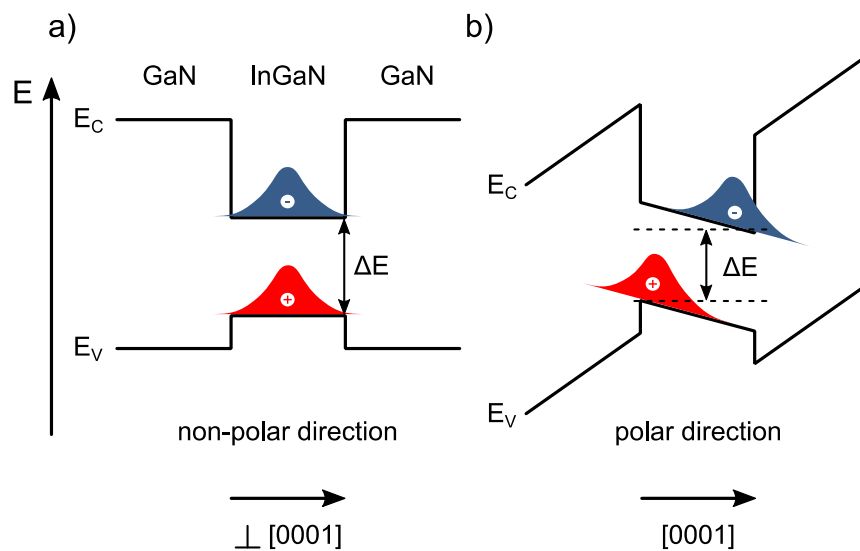


Figure 2.4. Carrier confinement and quantum-confined Stark effect in a GaN-InGaN-GaN heterostructure: (a) vanishing separation of electron-hole pairs along non polar directions; (b) spatial separation of electron hole pairs along polar directions.

The effect was first reported in [52] using AlGaAs quantum-well films. But as AlGaAs structures do not contain strong built-in polarisation fields, external electric fields had to be applied to trigger the QCSE.

As discussed in the previous section, the polarization along the InGaN/GaN c-axis can be induced due to piezoelectric effects, which corresponds to the situation in Figure

2.4 (b). The non-polar carrier confinement indicated in Figure 2.4 (a) is more likely to be observed in directions perpendicular to the InGaN/GaN c-axis. Controlling the QCSE in III-nitride materials is an essential task for development of next generation solid state lightning devices [53].

### 2.1.4 Semiconductor surfaces

The surface of a gas sensor material is the interface between the substance that has to be detected and the transducer. In the case of semiconductor gas sensors, chemical reactions of the analyte on the transducer surface alter the physical properties at the semiconductor surface which, in turn, influences the bulk of the semiconductor as well.

#### Surface states

Surface states can be categorized into two classes: intrinsic and extrinsic. Intrinsic states are created without any involvement of impurity atoms or structural defects on the surface. Intrinsic states are established even at perfectly pure or perfectly reconstructed semiconductor surfaces, whereas extrinsic ones are caused by imperfections at the semiconductor surfaces and by adsorbates that interact with the surface atoms. Surface states are essential for understanding the interaction of the semiconductor surfaces with adsorbates.

#### Intrinsic surface states

The electronic band structure of a semiconductor can be derived using Bloch functions. Bloch functions represent electronic wave functions in the periodic potential of a semiconductor crystal. From standard text books it is known that the periodic potential causes the forbidden energy region at the border of the Brioullin zones which can be derived from first order perturbation theory [37]. In this way the band structure of an infinitely extended semiconductor crystal can be derived.

The Bloch ansatz can be used for the calculation of wave functions and corresponding eigenstates of semiconductors with finite dimensions as well. There, the periodic potential jumps to the vacuum level upon reaching the surface. Figure 2.5 (a) shows a

1D periodic potential that abruptly ends at the surface. Wave functions corresponding to this potential distribution are standing Bloch waves with exponentially decaying tails. A simplified version is depicted in Figure 2.5 (b). States derived in this way are called Shockley states.

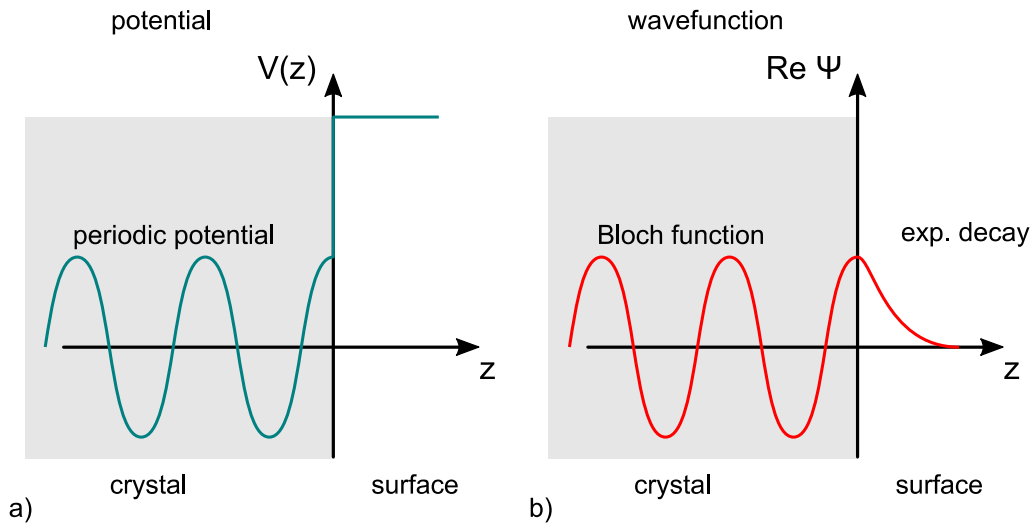


Figure 2.5. (a) Periodic potential Ansatz inside a semiconductor with a step to vacuum energy at the surface (b) standing Bloch wave function inside the semiconductor with an exponential decay component at the surface. (adapted from [42])

Another approach for the derivation of surface states is using the linear combination of atomic orbitals (LCAO) method. As the top layer is missing, surface atoms feature more loosely bound orbitals. Those orbitals that are still involved in back-bonds are different compared to the bulk ones, thus producing energy eigenstates closely localised at the surface. The model is generally called tight binding model and the states are called Tamm states. In Figure 2.6 (a) a schematic shows how the atomic states of surface atoms contribute to the surface density of states. These states can exhibit both acceptor- or donor-like character as indicated in Figure 2.6 (b).

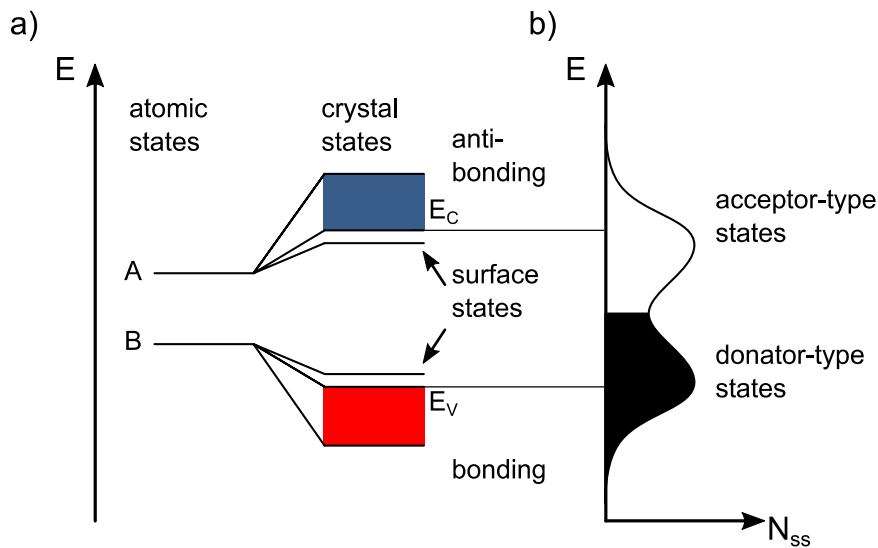


Figure 2.6. (a) atomic states of surface atoms induce new surface states due to the lack of binding partners at the surface (b) higher-energy states are likely to become electron acceptors and lower-energy ones, electron donors. (adapted from [42])

The surface states located close to the conduction band edge can take up electrons which means they are acceptor states or they can donate electrons when they are close to the valence band edge (donor type states). The semiconductor is electrically neutral when all surface donor states are occupied and all acceptor ones are vacant.

### Extrinsic surface states

Extrinsic surface states originate from imperfections of the crystal lattice at the surface. Deviations from an ideal reconstructed surface can have various reasons. Imperfections may be a result of missing atoms which affect the electronic structure at the surface. In the case of GaN, a missing nitrogen atom leaves a positively charged vacancy behind, which acts as an electron trap. Further, steps or terraces in the surface increase the amount of extrinsic surface states. Atoms at a step, for instance, have more broken bonds as an atom at an ideal surface.

The most important source of surface states in this thesis is adsorption. Adsorbates can be found in physisorbed states or in a more tightly bound chemisorbed states. Whereas the first type only causes small perturbations of the surface's electronic structure, the influence of the latter ones is more severe. Bonding and antibonding adsorbate-surface bonds then form new states at the surface.

All extrinsic states have in common that they are localized at those points where the deviations from the ideal surface occur. In contrast, intrinsic surface states are only localized in directions perpendicular but not parallel to the surface. This is a result of the translational symmetry on the surface.

### 2.1.5 Space charge layers at semiconductor surfaces

As described in the previous section, surface states can be electron acceptors or electron donors. When an acceptor-type state becomes occupied, the surface charge changes from neutral to negative. Donor-type surface states, in contrast, are neutral when occupied and positively charged when empty.

Considering GaN, which exhibits natural n-type conductivity due to unintentional impurities and acceptor-like surface adsorbate states, the situation depicted in Figure 2.7 can arise. On the left-hand side, a typical band profile of an n-type semiconductor is shown where the Fermi-level is slightly closer to the conduction band. The figure on the right-hand side shows the situation after electron charge has been transferred to acceptor type surface states and after the bulk and surface Fermi energies had lined up.

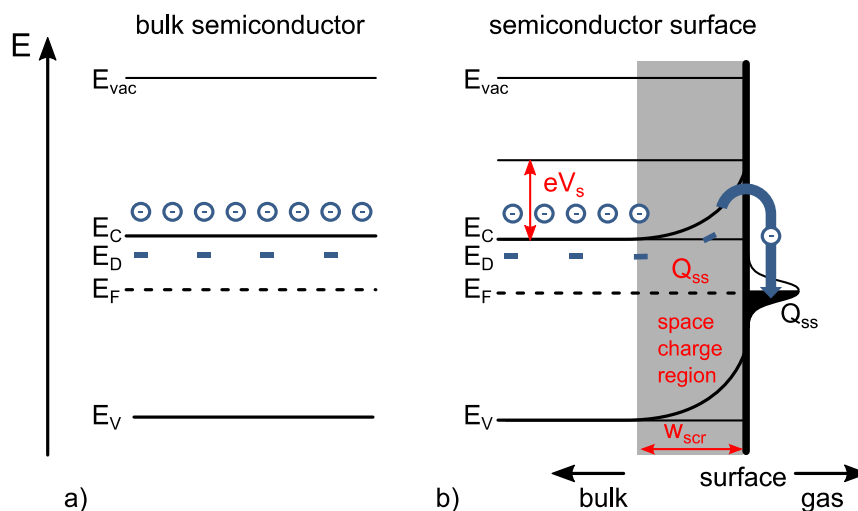


Figure 2.7. Band profile of an n-type semiconductor: (a) Band profile of a bulk material is shown on the left side. (b) The influence of occupied surface states on the band profile.

The surface state charge  $Q_{ss}$  is mirrored by charges inside the semiconductor ( $Q_{sc}$ ). In this way a space charge region is built up by ionizing donor atoms close to the surface. As most of the majority charge carriers are consumed, this area is called depletion zone. The position of the Fermi-level in the bulk material, i.e. far away from the surface, is determined by the doping concentration [54]. The energetic position of the acceptor states with respect to the conduction band edge  $E_C$  is fixed and determined by the chemical bond strength of the acceptor states. As indicated in Figure 2.7 (b) this bond strength ultimately determines how many negative adsorbates can be bound to the surface.

Assuming the surface band bending to be large compared to the thermal energy ( $|e V_s| \gg k_B T$ ), the occupation of donor states inside the semiconductor changes abruptly from zero to the full donor density when the bands begin to bend. In this situation it is legitimate to assume that the space charge in the semiconductor is uniformly distributed in the space charge region. The height of the surface potential  $V_s$ , caused by the band bending, can then be derived from Poisson's equation as a function of the length of the space charge region  $w_{scr}$ .

### Fermi Level Pinning

The band bending effect on n-type semiconductors can either result in accumulation or depletion layers, depending on the densities of acceptor- or donor-like adsorbates present on the surface. Acceptor adsorbates create an upward band bending (see Figure 2.7) while donor ones act in the opposite direction, bending the bands downwards and building up an accumulation layer at the surface. In both cases the band bending  $|e V_s|$  saturates at high surface state densities. This point of saturation is reached when the surface band bending becomes large enough to draw the surface Fermi energy below the band of adsorbate surface states. In this case the surface adsorbates start to discharge again and the surface band bending decreases again. At this point the surface Fermi energy becomes pinned inside the distribution of surface adsorbate states and the adsorbate density saturates. This saturation density is also called the Weisz limitation. In Figure 2.8 the Fermi level pinning is illustrated. Figure 2.8 (a) showing surface acceptor states being charged increasing the band bending and surface state levels. Figure 2.8 (c) shows the situation when surface states are above the

Fermi level and therefore these states are discharged reducing band bending and the surface state level. The equilibrium state is shown in In Figure 2.8 (b) with surface state levels pinned to the Fermi level.

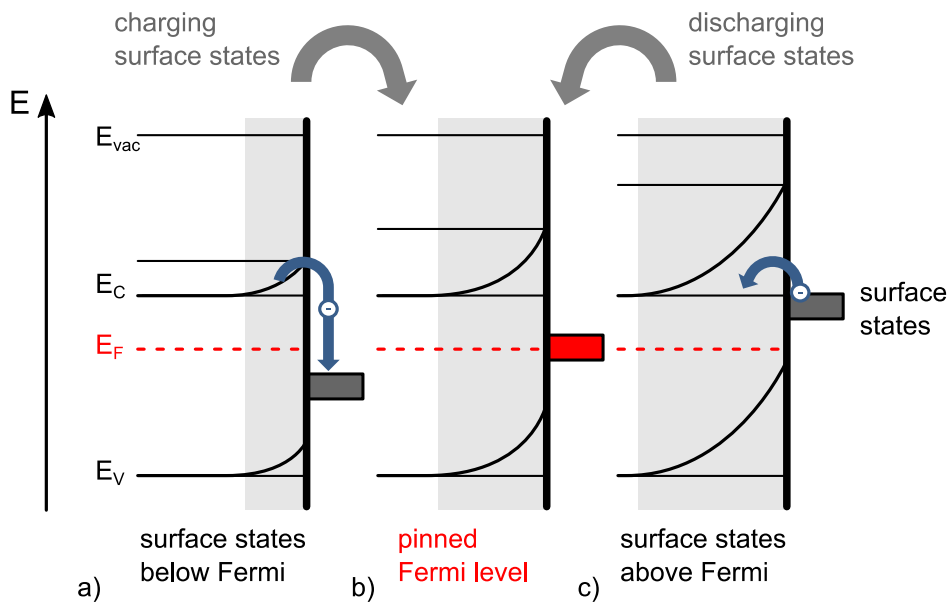


Figure 2.8. Fermi level pinning on an n-type semiconductor by acceptor-like surface states: (a) surface states below bulk Fermi level. Adsorbates become negatively charged, thus increasing the band bending (b) Fermi level pinned by surface states (c) surface states above bulk Fermi level. Adsorbates become discharged and band bending decreases.

According to ref. [55,56] the Fermi-level is pinned approx. 0.5 - 0.6 eV below the conduction band edge for GaN(0001) MBE layers.

### Surface band bending effect on nanowires

The band structure of semiconductors does not only depend on the bulk properties of the semiconductors and their varying degrees of surface band bending but also on the geometry of the semiconductor devices themselves. Especially when the dimensions are small and in the depletion region width  $w_{scr}$ , the electronic properties are strongly influenced by the surface properties of the semiconductor. For an approximate calculation of the band profile of InGaN/GaN nanowire structures with diameters in the range of 50-150 nm an analytical solution of Poisson's equation using cylindrical coordinates can be used:

$$\frac{1}{R} \frac{\partial}{\partial R} \left( R \frac{\partial}{\partial R} \Phi(R) \right) = \frac{-q}{\epsilon_r \epsilon_0} (p - n + N_D^+ - N_A^-) \quad [57] \quad (2.1)$$

Suppose that we are dealing with an n-type semiconductor with an outer diameter of  $R$ . To simplify it is assumed that in the outer depletion region with a width  $w_{scr}$  all donors are fully ionized ( $p - n + N_D^+ - N_A^- \approx N_D$ ) and that the net charge in the bulk ( $r < R - w_{scr}$ ) is negligible, an analytical solution of the above equation can be obtained:

$$\Phi(r_0, r) = \frac{q N_D}{4 \epsilon_r \epsilon_0} \left( r^2 - R^2 - 2r_0^2 \ln \left( \frac{r}{r_0} \right) \right) \quad [57] \quad (2.2)$$

where  $r_0 < r < R$  and  $r_0 := R - w_{scr}$

In Figure 2.9 some simplified situations of semiconductor nanowires with identical surface band bending but different diameters are depicted. For acceptor-type surface states on an n-type semiconductor, a depletion layer below the nanowire surface is built up. When the nanowire diameter decreases below a critical value  $R_{crit}$ , the nanowire is fully depleted with no bulk region, i.e. the respective band edges do not decrease down to the bulk level. This is indicated on the left-hand side of Figure 2.9. The image in the centre shows a nanowire with exact that critical diameter which is also fully depleted. On the right-hand side, a thicker nanowire with bulk material in the middle is shown.

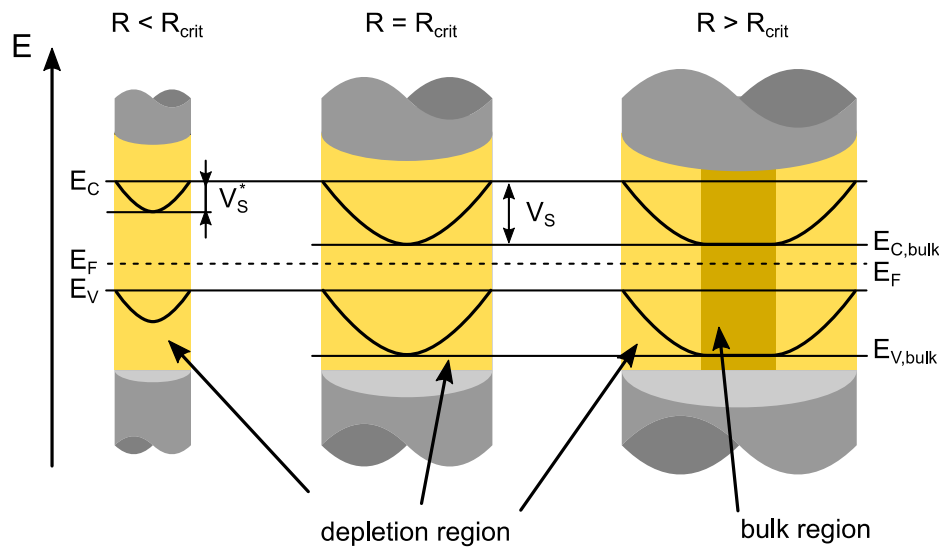


Figure 2.9. Band bending inside a nanowire. When the diameter decreases below a critical value the nanowire becomes fully depleted.

Whether the nanowire has a bulk core or the nanowire is fully depleted is determined by the thickness of the space charge region  $w_{scr}$ , i.e. by the doping concentration and by the band bending  $V_s$ . Typical values of  $V_s$  are in the range of  $k_B T$ . According to ref. [55] typical depletion layers of InGaN/GaN nanowires reach approx. 50 – 100 nm into the bulk. Here a Fermi level pinning of 0.5 eV below the conduction band and a doping density of  $10^{17} \text{ cm}^{-3}$  were assumed. Nanowires which have diameters of less than 100 nm should then be fully depleted, i.e. be in a state as shown on the left-hand side of Figure 2.9.

## 2.2 Basics of adsorption

The functioning of many gas sensing devices depends on physical interactions of specific kinds of analyte molecules with a transducer surface. The first step of the gas sensing mechanism is usually an adsorption process. The physics of adsorption strongly depends on the physical and chemical properties of those molecules that adsorb, called adsorbates, and on those surfaces on which these adsorb, called adsorbents. In this section a brief overview of the fundamental gas adsorption mechanisms is given. In order to get deeper insights into this topic, the reader is referred to the textbooks of surface physics [42,43,58].

Adsorption quantitatively describes the number of molecules  $N_A$  adsorbed on a unit surface area of adsorbent kept at a temperature  $T$  when a gas  $A$  abounds in the air ambient at the partial pressure  $p_A$  :

$$N_A = f(p_A, T) \quad (2.3)$$

There are two types of adsorption that are commonly distinguished from each other: physisorption and chemisorption. Physisorption, in general, is a fast and reversible process, in which the chemical identity of the adsorbing molecules remains intact and in which they do not form chemical bonds across the adsorbent/adsorbate interface. Upon chemisorption, chemical bonds between adsorbate and adsorbent are formed and the molecular nature of the adsorbates can be changed drastically. As in the process of chemisorption existing chemical bonds need to be broken and new chemical bonds to be formed, chemisorption requires thermal activation. Chemisorption, as a consequence, takes place at higher adsorbent temperatures than physisorption. As chemisorption bonds can be quite strong, chemisorbed molecules may fail to desorb again at moderate temperatures, thereby permanently altering the adsorbent surface. In gas sensing devices such heavily sticking adsorbates can give rise to baseline drift effects. The two different adsorption processes often occur in combination. An approaching molecule is first physisorbed onto the surface and after acquiring thermal energy from the adsorbent, chemisorbed onto the adsorbent. These two processes are described in more detail below, although in reality the distinction is not very sharp as physisorption can gradually turn into chemisorption.

### 2.2.1 Physisorption

Physisorption is a process in which the electronic structure of the adsorbed molecule is hardly perturbed. The bonding interactions are mediated by Van der Waals forces acting between adsorbent and adsorbate. In such interactions the adsorbing molecules induce electrical dipoles in the adsorbent surface, which influences the permanent or induced dipoles in the adsorbing molecules. The interaction potential resulting from such fluctuating dipole-dipole interactions is normally described by so-called Lennard-Jones potentials (Figure 2.10):

$$V(r) = \left[ \left( \frac{a}{r} \right)^{12} - \left( \frac{b}{r} \right)^6 \right] \quad (2.4)$$

where

- $r$  distance between interacting atoms
- $a$  repulsive component
- $b$  attractive component

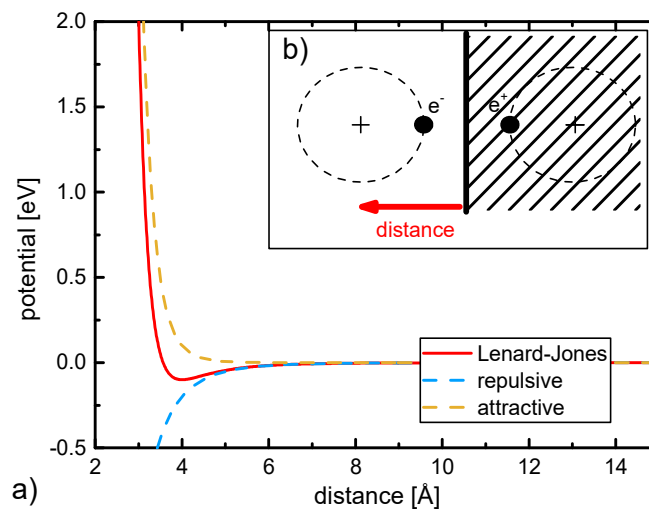


Figure 2.10. (a) Potential of a typical physisorption example; (b) mirror charge of an adsorbing hydrogen atom.

Typical physisorption energies lie in the range between 10 and 100 meV. As, at room temperature, the Boltzmann energy ( $k_B T \approx 25$  meV) exceeds most typical physisorption energies, physisorption is predominantly a low-temperature phenomenon. Physisorption, nevertheless, is also important at room temperature or above, as physisorption usually precedes the formation of tighter-bound chemisorption states.

Due to their strong permanent dipole moments and because of the presence of non-binding lone-pair orbitals on their O-atoms, water molecules play a special role among physisorbing molecules. Caused by the formation of weak hydrogen-bridge bonds ( $E_b \sim 0.4$  eV), liquid water has an anomalously high boiling point. On adsor-

bents, water molecules may also form relatively stable H-bridge bonds when the adsorbent surfaces are oxidized or hydrogen-terminated. In addition, a first monolayer of adsorbed H<sub>2</sub>O molecules may attract additional H<sub>2</sub>O molecules into multi-layer adsorbates. Such multi-layer adsorbates severely influence the adsorption of other molecules. Especially molecules that are soluble in water can accumulate inside pre-adsorbed water layers, which is not strictly speaking adsorption but absorption. Such absorption processes can play a major role in gas sensor physics which has been demonstrated using conventional MOX material at room temperature conditions [59].

### 2.2.2 Chemisorption

Chemisorption of molecules onto a surface involves the formation of covalent bonds between adsorbates and adsorbent. The electronic structure of the adsorbent lattice is strongly altered at the surface. In some cases a charge transfer between adsorbate and adsorbent does take place which is called ionosorption. Chemisorption in general involves breaking and rearranging of covalent bonds which results in binding energies for the new adsorbate-adsorbent complexes in the range from 0.5 to 5.0 eV [60]. Compared to physisorption the adsorbate-adsorbent distance is smaller in chemisorption. In most cases chemisorption processes are exothermic processes, releasing thermal energy.

Large energy gains in chemisorption often require that an adsorbing molecule is first broken down into single atoms to enable each constituent atom to gain binding energy by chemisorption at the adsorbent surface. A typical example is the adsorption of O<sub>2</sub> on metal oxide surfaces. While at moderate temperatures O<sub>2</sub> adsorbs in the form of O<sub>2</sub><sup>-</sup> ions, higher surface temperatures cause the O<sub>2</sub> molecules to break down into single O atoms, allowing both of them to adsorb in the form of O<sup>-</sup> ions, Figure 2.11 is a potential energy diagram that describes such a process. The curve for O<sub>2</sub> adsorption is the one with the shallower minimum and an equilibrium point farther away from the surface. Whereas in this first case the energy of the adsorbate is zero at large distances from the adsorbate surface, the second one starts out at a finite energy  $E_d$  which is the dissipation energy of the molecular analyte. This energy needs to be supplied by the adsorbent in the form of thermal energy to generate single atoms. These individual atoms can approach closer to the surface and bind tighter to the adsorbent.

The superposition of both potential energy curves produces a composite curve with two equilibrium points corresponding to molecular and to atomic adsorption. Both minima are separated by a potential hill, which explains that dissociative adsorption occurs at higher substrate temperature than molecular adsorption.

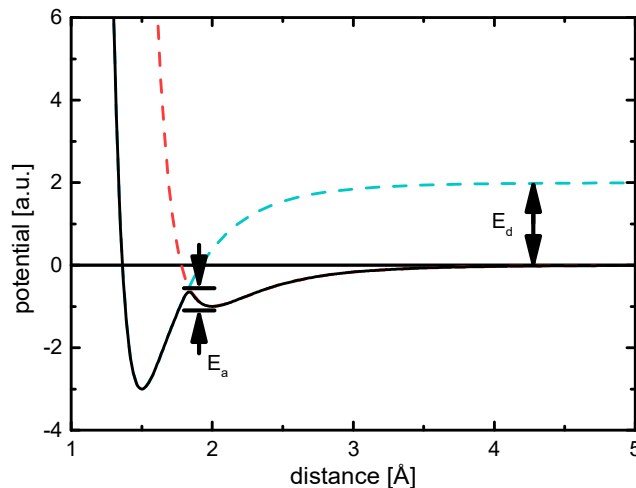


Figure 2.11. Potential energy curves describing molecular (black/red curve) and atomic or dissociative chemisorption (black/green curve).

### 2.2.3 Main laws of adsorption

When a gaseous medium is in contact with a surface, adsorbing molecules begin to occupy the surface. Instantaneously a reverse process starts which counteracts the adsorption process and which forces already adsorbed molecules back into the gas phase, which is called desorption. In thermal equilibrium the rates of adsorption and desorption are equal which results in a constant coverage of the surface over time. The time for reaching such an equilibrium can vary from less than milliseconds to more than hours or days [60].

A simple model of adsorption has been proposed by Langmuir [61]. The assumptions made in Langmuir's theory are:

- (i) adsorbent surface is homogenous
- (ii) adsorption process is reversible
- (iii) interactions between adsorbates are neglected

- (iv) maximum coverage is restricted to a monolayer
- (v) molecular, non-dissociative adsorption

### Adsorption kinetics

In the following the kinetics of adsorption is described.

From gas kinetics it can be derived that the time rate of impinging particles  $N_{imp}$  per area is [62]:

$$\frac{dN_{imp}}{dt} = \frac{p}{\sqrt{2 \pi m k_B T_{gas}}} \quad (2.5)$$

The rate depends on the partial pressure  $p$ , the temperature of the molecular gas  $T_{gas}$  and the molecular mass  $m$  of the impacting particles.  $k_B$  denotes Boltzmann's constant.

With the sticking probability  $S$ , which is the probability that an impacting molecule will actually rest on the substrate, one obtains for the adsorption rate:

$$\frac{dN_{ads}}{dt} = S \frac{dN_{imp}}{dt} \quad (2.6)$$

The sticking coefficient for activated adsorption is

$$S(\theta) = \sigma f(\theta) \exp\left[-\frac{\epsilon_{ads}}{k_B T}\right]. \quad (2.7)$$

The activation energy  $\epsilon_{ads}$  in the exponential Boltzmann term indicates that a certain amount of energy is required for forming bonds between adsorbate and adsorbent. The condensation coefficient  $\sigma$  accounts for the molecular orientation and the steric factor  $f(\theta)$  depends on the occupation  $\theta$  of the adsorbent. For non-dissociative adsorption, which is the case for the Langmuir model, the steric factor  $f$  is

$$f(\theta) = \frac{N_0 - N_{ads}}{N_0} = 1 - \theta. \quad (2.8)$$

The occupation  $\theta$  is defined as the ratio between the number of adsorbed molecules  $N_{ads}$  and the overall number of adsorption sites  $N_0$

$$\theta := \frac{N_{ads}}{N_0}. \quad (2.9)$$

The above equations can be combined into the adsorption rate and simplified by introducing a temperature-dependent adsorption rate parameter  $k_{ads}(T)$  that combines all prefactors except for the partial pressure and the steric factor:

$$\frac{d N_{ads}}{d t} = p \underbrace{\frac{1}{\sqrt{2 \pi m k_B T_{gas}}} \exp\left[-\frac{\epsilon_{ads}}{k_B T}\right] \sigma}_{=:k_{ads}(T)} (1 - \theta) = k_{ads}(T) (1 - \theta) p \quad (2.10)$$

Desorption of the adsorbed molecules can be described by:

$$\frac{d N_{des}}{d t} = \nu \exp\left[-\frac{\epsilon_{des}}{k_B T}\right] N_{ads} = k_{des} N_{ads}. \quad (2.11)$$

The rate of desorption is proportional to the number of adsorbed molecules and is temperature activated which is described by a Boltzmann term.  $\nu$  is a constant that is typically in the range of optical phonon frequencies of the adsorbent solid.

## Adsorption Equilibrium

### Langmuir

Adsorption isotherms are functions that relate the surface coverage of adsorbates  $\theta$  on a certain adsorbent to the adsorbate partial pressure  $p_A$  in the gas phase and to the temperature  $T$  of the adsorbent.

There are several ways for the derivation of the Langmuir equation describing the surface coverage with molecules. Here the Langmuir isotherm is derived using rate equations for adsorbing and desorbing molecules:

$$\dot{N}_{ads} = k_{ads} p_A (N_0 - N_{ads}) \quad (2.12)$$

where the adsorption is limited by the amount of already adsorbed molecules (coverage  $\theta = N/N_0$ ). The desorption process is only a function of  $N_{ads}$ :

$$\dot{N}_{des} = k_{des} N_{ads} \quad (2.13)$$

In thermal equilibrium adsorption and desorption should yield a state of zero net adsorption. This equation can be solved for the occupancy  $\theta$ :

$$\theta := \frac{N_{ads}}{N_0} = \frac{p_A}{p_A + \frac{k_{des}}{k_{ads}}} \quad (2.14)$$

At any given temperature the rate constants  $k_{ads}$  and  $k_{des}$  are constants and the coverage  $\theta$  approaches unity in the limit of high partial pressures.

If one assumes the adsorption and desorption processes to be thermally activated, following Boltzmann's laws as proposed in the adsorption kinetics in the previous section

$$k_{ads} \propto e^{-\frac{\epsilon_{ads}}{k_B T}} \rightarrow k_{ads} = k_{ads,0} e^{-\frac{\epsilon_{ads}}{k_B T}}, \quad (2.15)$$

$$k_{des} \propto e^{-\frac{\epsilon_{des}}{k_B T}} \rightarrow k_{des} = k_{des,0} e^{-\frac{\epsilon_{des}}{k_B T}}, \quad (2.16)$$

one obtains from equation (2.14):

$$\Theta_{Langmuir} = \frac{p}{p + P_{00} e^{-\frac{E_{ads}}{k_B T}}} \quad (2.17)$$

where

$$P_{00} = \frac{k_{des,0}}{k_{ads,0}} \quad (2.18)$$

and

$$E_{ads} = \epsilon_{ads} - \epsilon_{des}. \quad (2.19)$$

From statistical thermodynamics the so called Langmuir desorption pressure  $P_{00}$  can be calculated from the quantum volume [62,63]:

$$P_{00}(T, M) = \frac{k_B T}{V_Q(T, M)} \quad (2.20)$$

The quantum volume  $V_Q$  is defined as:

$$V_Q(T, M) = \left( \frac{h^2}{2 \pi M k_B T_{sub}} \right)^{\frac{3}{2}} \quad (2.21)$$

where

- $M$       molecular mass
- $h$       Plank's constant
- $T_{sub}$     temperature on substrate (adsorbent surface)

Typical values for the desorption pressure are in the range of  $10^{11}$  Pa. For instance, an oxygen molecule at room temperature ( $T = 25^\circ\text{C}$ ) has a desorption pressure of  $2.54 \cdot 10^{11}$  Pa.

In Figure 2.12 a set of Langmuir isotherms shows the temperature dependency of the adsorbent coverage over partial pressure of the adsorbate. In a half-logarithmic representation the s-shaped isotherms shift over orders of magnitudes along the pressure axis towards high values with increasing temperature.

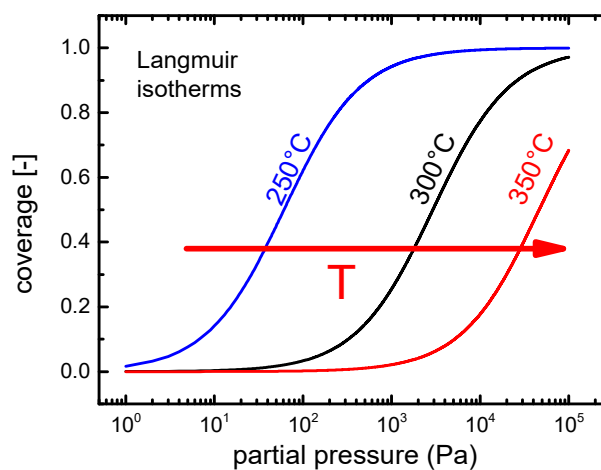


Figure 2.12. Langmuir coverages for different values of adsorbent temperature.

## Other adsorption isotherms

In the limit of very low coverages, the coverage with adsorbates is proportional to the partial pressure. This is the simplest case of an adsorption isotherm. It is called Henry-Isotherm.

$$\theta_{Henry} \propto p \quad (2.22)$$

For many systems where only low levels of adsorption ( $\theta \ll 1$ ) are considered, the Henry model is a good approximation.

The Freundlich isotherm follows a potential dependence of surface coverage and partial pressure of the adsorbent. The isotherm was determined solely empirically and is valid for gases up to a certain saturation pressure. The isotherm takes into account that the net rate of adsorption is reduced when the coverage is increased. [60]:

$$\theta_{Freundlich} \propto p^\alpha \quad (2.23)$$

As Langmuir assumes identity of all possible adsorption sites, the model fails if some adsorption sites are energetically more favourable than others. In this case these favourable adsorption sites are occupied first and as the enthalpy of adsorption becomes less negative for the rest of the adsorption sites. The adsorption velocity is then reduced additionally. An attempt describing this behaviour is using the Temkin isotherm:

$$\theta_{Temkin} \propto \ln[\alpha p] \quad (2.24)$$

In gas sensor theories Langmuir adsorption is the most commonly used one as it has proven to be applicable for many different kinds of sensors, especially when these are operated at elevated temperatures [64,65].

### 2.2.4 Multilayer Adsorption

The Langmuir adsorption model is self-limited to a monolayer of adsorbed molecules. In extreme cases all adsorption sites of the adsorbent are occupied and any further adsorption is terminated unless pre-adsorbed molecules desorb and offer empty adsorption sites for re-adsorption.

In 1938 Brunauer, Emmett and Teller [66] suggested a model that is an extension of the Langmuir model. The assumptions of the so-called BET model are similar to the single-layer Langmuir theory but multilayer adsorption is allowed. This model can be derived from a kinetic perspective by assuming a first-layer Langmuir adsorption and by allowing additional adsorbates to adsorb on this first layer of adsorbates. Repetition of this process allows water molecules to form multilayer adsorbates on gas sensor surfaces [59]. When the transducers are operated at low temperature many semiconductor gas sensors show sensitivity towards water soluble gases such as NO<sub>2</sub>, NH<sub>3</sub> and alcohols. This is an universal observation for all kinds of gas sensor materials such as conventional MOX [67–70], hydrogenated diamond [71–73] and III-nitride materials in flat and nano-structured configurations [26,27,74–76]. On MOX materials it was shown that nanostructured surfaces do not prevent building up BET layers of water adsorbates, but desorption rates at least seem to be enhanced [59], possibly due to the effect of increased desorption pressure [77,78]. As III-nitride materials tend to build up oxide layers at their surfaces, similarities of water adsorption can be expected at InGaN/GaN nanowire surfaces [79–82].

Multi-layer adsorbates can be built up as shown in Figure 2.13. In this graph, the adsorbent surface is sub-divided into  $N_{SA}$  individual cells to indicate potential adsorption sites. Each of these cells is assumed to be able to accommodate 0, 1, 2, ... ,  $n$  molecules. In such a multi-layer adsorption scenario the total number  $N_{\Sigma}$  of adsorbates per unit area becomes:

$$N_{\Sigma} = N_{SA}(0 \theta_0 + 1 \theta_1 + 2 \theta_2 + \dots) = N_{SA} \sum_{i=1}^{\infty} i \theta_i \quad (2.25)$$

with the values of  $\theta_i$  standing for the probabilities that a particular site will be occupied with 0, 1, 2, ... ,  $n$  adsorbates. Here the lowest indexed occupation  $\theta_0$  stands for unoccupied adsorption sites. The higher indexed occupations  $\theta_i$  with  $i > 0$  denote occupations with one and more than one adsorbates. As each adsorption site must be accounted to one index, the summation over all indices must equal to unity:

$$\theta_0 + \theta_1 + \theta_2 + \dots = \sum_{i=0}^{\infty} \theta_i = 1 \quad (2.26)$$

The total occupation is similarly defined as in the case of the simple Langmuir adsorption:

$$\theta_{\Sigma} = \frac{N_{\Sigma}}{N_{SA}} = \sum_{i=1}^{\infty} i \theta_i \quad (2.27)$$

Unlike in the simple Langmuir case, and as easily visible from the above equations,  $\theta_{\Sigma}$  in the BET case is no longer limited to values below one.

In a dynamic situation, as in humidity sensing tests, the numbers of molecules at each site can change via adsorption and desorption processes via interactions with  $\text{H}_2\text{O}$  molecules in the gas phase. In each of these processes, an adsorption site initially in the coverage fraction  $\theta_i$  can either change into fraction  $\theta_{i+1}$  or fraction  $\theta_{i-1}$ , respectively. These exchange processes are visualized in Figure 2.13 for the three cases of zero, one and two layers already adsorbed.

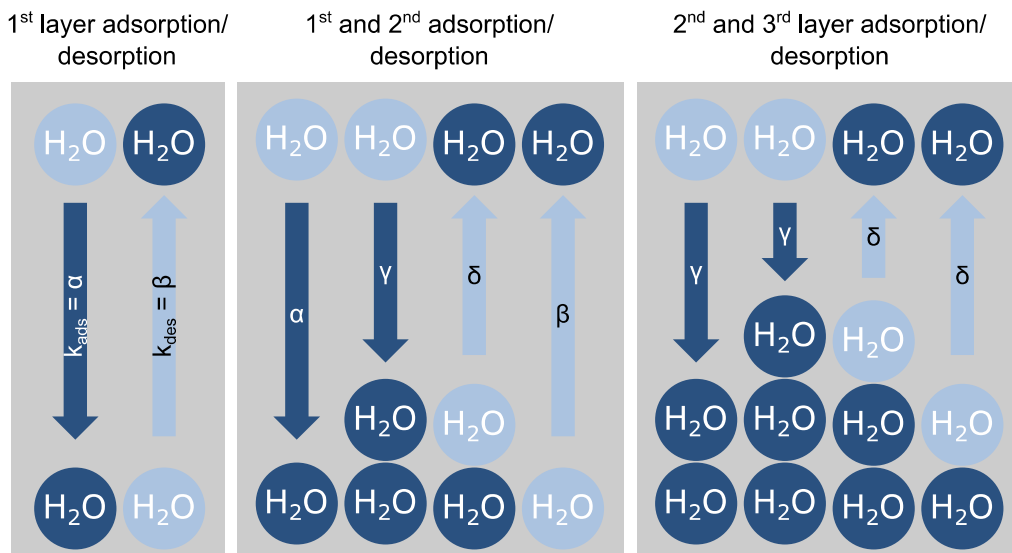


Figure 2.13. Formation of multi-layer BET adsorbates on a sensor surface. The three boxes indicate adsorption-/desorption processes occurring with a bare substrate, with a substrate covered with one monolayer and with two monolayers of  $\text{H}_2\text{O}$  molecules.

The isotherm for BET type adsorption can be described by:

$$\theta(p, T) = \frac{p}{1-p} \frac{b_{BET}(T)}{[1 + p (b_{BET}(T) - 1)]} \quad (2.28)$$

with  $b_{BET}(T)$  standing for the so-called BET constant:

$$b_{BET}(T) = \exp \left[ \frac{\epsilon_1 - \epsilon_n}{k_B T} \right] \quad (2.29)$$

The parameters in the square brackets stand for the adsorption energies for the first layer monolayer ( $\epsilon_1$ ) and the follow-on layers ( $\epsilon_n$ ).

In Figure 2.14 some BET isothermes for different values of the ratio of  $\epsilon_1$  and  $\epsilon_n$  are visualized. Here  $\epsilon_n$  is denoted as heat of liquefaction  $\epsilon_{lf}$ . In the special case ( $\epsilon_1 = \epsilon_{lf}$ ) and at very low gas concentrations the BET adsorption isotherm is closely approximated by a simple Langmuir adsorption isotherm. At concentrations higher than about 10% rel. humidity, significantly more water is adsorbed as predicted by the Langmuir theory. As in real-life sensor applications humidity levels higher than 10% rel. humidity are expected, BET water adsorption therefore cannot be ruled out.

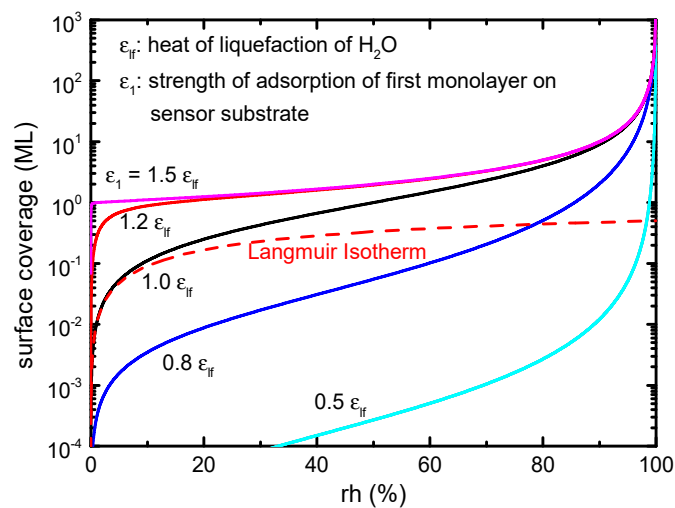


Figure 2.14. BET coverage of water in monolayers (ML) at 293 K as a function of the relative humidity. The degree of BET adsorption critically depends on the strength of adsorption  $\epsilon_1$  of the first monolayer on the substrate. The full and broken lines at  $\epsilon_{lf}$  0.8 show that Langmuir adsorption isotherms approximate BET ones in the limit of low humidity.

## 2.2.5 Competitive adsorption

In the previous sections adsorption of only one kind of molecular species was considered. Work on semiconductor gas sensors has shown that such sensors often exhibit considerable levels of cross-sensitivity. Such cross-sensitivity is plausible as, on a semiconductor surface, there is only a very limited number of adsorption sites whereas potential analyte species can go into the hundreds or even thousands. In such cases competitive situations arise in that different molecules may try to adsorb on one and the same adsorption site. Such situations of competitive adsorption can be treated by an extension of the above-described Langmuir adsorption theory.

As stated before, the single-component Langmuir theory assumes that the time rate of change of the surface coverage of species A is the difference of an adsorption term proportional to  $(1 - \theta_A)$  and a desorption term proportional to  $\theta_A$ . This approach is easily extended to two and more competing species, by considering a differential equation for each competing species and by modifying the respective adsorption terms. In the simplest case of two competing species the corresponding equations read:

$$\frac{d\theta_A}{dt} = k_{adsA}(T) p_A [1 - \theta_A(t) - \theta_B(t)] - k_{desA}(T) \theta_A(t), \quad (2.30)$$

$$\frac{d\theta_B}{dt} = k_{adsB}(T) p_B [1 - \theta_A(t) - \theta_B(t)] - k_{desB}(T) \theta_B(t). \quad (2.31)$$

In steady state, the two rate equations can be solved for the  $\theta_A$  and  $\theta_B$ :

$$\theta_A = \frac{p_A}{p_A + \frac{k_{desA}(T)}{k_{adsA}(T)} \left[ 1 + p_B \frac{k_{adsB}(T)}{k_{desB}(T)} \right]} \quad (2.32)$$

$$\theta_B = \frac{p_B}{p_B + \frac{k_{desB}(T)}{k_{adsB}(T)} \left[ 1 + p_A \frac{k_{adsA}(T)}{k_{desA}(T)} \right]} \quad (2.33)$$

Assuming that  $k_{ads}(T)$  and  $k_{des}(T)$  exhibit an Arrhenius-type temperature dependence with energy parameters  $\varepsilon_{ads}$  and  $\varepsilon_{des}$ , both steady-state solutions can be rephrased in the form:

$$\theta_A = \frac{p_A}{p_A + P_{00A}(T) \exp\left[-\frac{E_A}{k_B T}\right] \left[1 + \frac{p_B}{P_{00B}(T)} \exp\left[\frac{E_B}{k_B T}\right]\right]} \quad (2.34)$$

In these latter equations the equilibrium adsorption energies  $E_A$  take the form:

$$E_A = \varepsilon_{desA} - \varepsilon_{adsA} \quad (2.35)$$

and similarly for  $E_B$ .  $P_{00A}$  and  $P_{00B}$  are the Langmuir desorption pressures of species A and B, respectively, and  $V_{QA}$  and  $V_{QB}$  their quantum volumes.

Similarly, one obtains for the occupation with species B:

$$\theta_B = \frac{p_B}{p_B + P_{00B}(T) \exp\left[-\frac{E_B}{k_B T}\right] \left[1 + \frac{p_A}{P_{00A}(T)} \exp\left[\frac{E_A}{k_B T}\right]\right]} \quad (2.36)$$

In Figure 2.15 the isotherm for competitive adsorption for two components with two different adsorption energies are shown ( $E_A = 0.7$  eV and  $E_B = 0.5$  eV). In this example the component B covers all adsorption sites until the partial pressure of component A is increased and both components are at equilibrium at about 50 Pa of component A. For comparison the isotherm for similar parameters of component A is drawn. When neglecting component B the surface is covered by A for orders of magnitude earlier than with competitive adsorption.

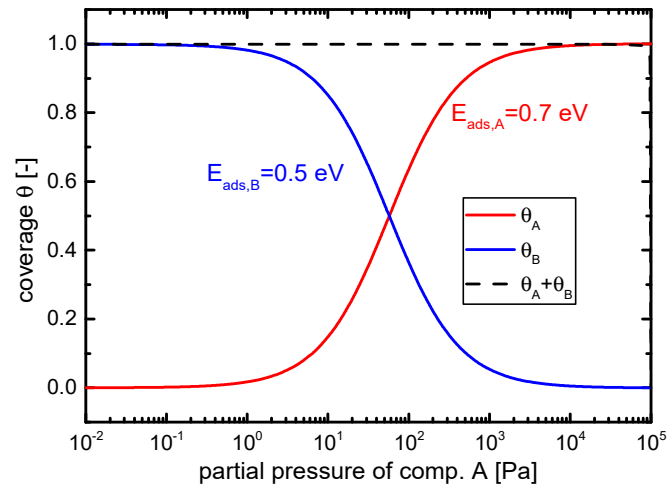


Figure 2.15. Adsorption isotherms for competitive adsorption for two adsorbates with 0.7 eV and 0.5 eV. The dashed line shows simple Langmuir adsorption isotherm for component A for comparison.

Competitive adsorption is well known in chemistry [83] and is particularly important in the field of chromatography [84–86]. However, only little research about competitive adsorption in the field of gas sensor physics has been reported so far.

## 3 Materials preparation and functional assessment

This section summarizes those experimental details that are related to the preparation of the InGaN/GaN opto-chemical transducers and to their experimental assessment. In the first part, special attention is paid to the characterisation of the opto-chemical transducers as gas sensors. The second part briefly describes how the InGaN/GaN nanowire samples provided by the University of Gießen. This section also summarizes all materials characterisation work that was carried out at the University of Gießen before delivery of the opto-chemical transducers to AIRBUS Group Innovations. These results include scanning electron microscope (SEM) images and low-temperature photoluminescence spectra. In the last section the experimental details of the photoluminescence measurements in terms of an extended preliminary sensor characterization are given. The test equipment was developed towards establishing a new sensor technology. The equipment is not meant to replace laboratory analytical tools or measurement equipment but the sensors still give an interesting insight into the physics and chemistry at InGaN/GaN nanowire exposed to different gas atmospheres.

### 3.1 Gas test rig

Most experiments in this work involve experiments on gas sensors exposed to a well-controlled environment of test gas and a defined carrier gas flow. The parameters that have to be controlled are gas flow, pressure, temperature and humidity. A custom-designed gas test rig consisting of several mass flow controllers (MKS) with a 1% of their full range accuracy [87], valves and pressure regulators, allow controlling these quantities. Figure 3.1 shows a schematic sketch of the test rig at Airbus Group Innovations with its key components.

The system contains five test gas supplies. The test gases of interest are contained in pressurized gas cylinders. The cylinders are delivered from a commercial gas supplier with the test gases of interest being diluted in a background carrier gas. Background gases are typically synthetic air (SA) or nitrogen ( $N_2$ ). Synthetic air is composed of 80% nitrogen and 20% oxygen. Unlike real air, synthetic air is almost pure and, most importantly, almost absolutely dry. The residual concentrations of normally occurring air contaminants is in the sub ppm level [88]. A typical test gas that is supplied in pre-mixed pressurized gas cylinders is nitrogen dioxide ( $NO_2$ ), which is a key representative from the group of oxidizing gases. Another example is Ethylene ( $C_2H_4$ ), which is a typical representative from the group of combustible gases. In most cases one is interested in the relationship between test gas concentration and sensor response. Therefore the concentration of the test gases is further diluted using similar background gas as already in the test gas cylinders. At the gas test rig nitrogen is supplied by a huge liquid nitrogen reservoir and synthetic air from a big array of SA-containing cylinders.

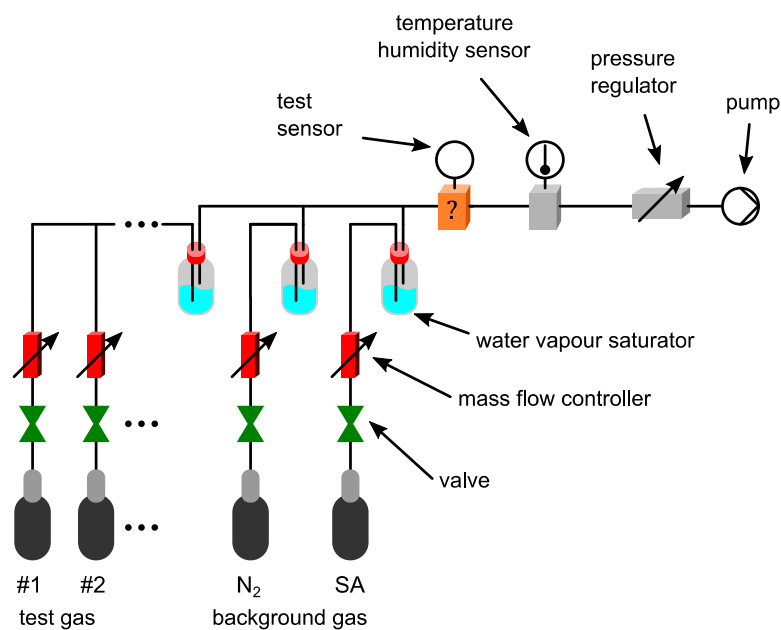


Figure 3.1. Schematics of the gas test rig at Airbus Group Innovations for controlling gas flows in the range from 0 to 1000 sccm and pressures in the range from 0 to 2 bar (abs.). Up to 5 test gases can be mixed with backgrounds of either nitrogen or synthetic air. Humidity can be added using gas vapour saturation bottles (bubbler). The temperature is usually set by the sensor setup itself.

As real life applications of gas sensors often involve measurements in ambient atmosphere containing non-negligible amounts of humidity, cross sensitivities against water vapour are an important issue. This is a strong motivation for testing the humidity response of gas sensors in a sensor test rig. In order to add humidity to the gas mixture of interest the gas test rig, bubblers (vapour saturation bottles) can be optionally inserted into the gas lines. In principle the bubblers add humidity by pushing gas through the water inside the bottles and the headspace volume over the water. It is assumed that the humidified gas is almost completely saturated meaning that the water concentration is equal to the vapour pressure of water at ambient temperature.

The vapour pressure is the pressure where the vapour of a substance is in thermodynamic equilibrium with its condensed phase. The vapour pressure depends on temperature and can be found in tables whose data were experimentally determined. In addition, there are also equations available that approximate the vapour pressure of water. The most common approximation for the relationship between vapour pressure  $p_{0,H2O}$  and the temperature  $T$  is the Antoine equation which is derived from the Clausius-Clapeyron [60] relation:

$$\log_{10} p_{0,H2O} = A - \frac{B}{C+T} \quad (3.1)$$

$A$ ,  $B$ ,  $C$  are parameters that have to be chosen from a table corresponding to a certain temperature range. Alternatively the vapour pressure can be satisfactorily calculated using

$$p(\text{mmHg}) = \text{Exp} \left[ 20.438 - \frac{5044}{T(\text{K})} \right]. \quad [60] \quad (3.2)$$

Besides for the purpose of humidification, the bubblers can also be used for injecting other substances into the gas lines as well. The requirement for the substance, of course, is that it abounds in liquid form at room temperature. A range of alcohols, for example, fulfils this requirement. Using gas bubblers, alcohol vapour concentrations in the range of their lower explosive limit levels (LEL) can be dosed (several thousands of ppm).

A different approach of adding vaporised liquids into a test gas line is using liquid injectors. Liquid injectors allow small amounts of liquid to be fed into the gas flow of

the test rig. An extremely slow screw-driven syringe steadily supplies the test liquid to an evaporation chamber whose temperature can be adjusted to the liquid's boiling point. The substance is converted from the liquid to the gaseous state and the resulting gas is mixed with the constantly flowing background carrier gas of the test rig.

Ozone is another important test gas which is potentially harmful because of its high oxidizing power. As ozone is not long-term-stable, it cannot be stored in pressurized gas cylinders. It therefore has to be generated on-demand. Here a commercial ozone generator (Ansyco) is used for ozone gas tests. A UV light source is generating oxygen radicals out of the molecular oxygen of synthetic air. When these radicals meet with excess oxygen of the SA supply, ozone is produced. With this setup ozone concentrations of up to approximately 0.5 ppm in SA background are achievable. The  $O_3$  concentration is measured by a dedicated ozone analyser (Ansyco) and the concentration can be manually adjusted through the current of the UV light lamp of the ozone generator. As oxygen is required to form ozone it is not possible to investigate solely ozone in an inert background gas such as nitrogen.

Gas sensors, like almost any sensor, are sensitive towards temperature changes. The opto-chemical InGaN/GaN transducers which are the main subject of this thesis, are no exception. For measurement the InGaN/GaN transducers are firmly mounted inside a macroscopic test chamber on top of a heatable substrate holder. Due to the good thermal contact, the transducer temperature is very close to the temperature of the substrate heater. In case active heating is not performed, the transducer temperature is close to ambient temperature ( $\sim 25^\circ\text{C}$ ). A small amount of overheating occurs due to the LED illumination and the ensuing non-radiative recombination processes, which occur inside and at the surfaces of the InGaN/GaN transducers. This amount of overheating is estimated to be lower than  $\Delta T \sim 5$  K. The surface temperature of the transducers is additionally influenced by heat conduction and convection from the transducers into the test gas flow. Changing flow conditions may therefore affect the surface temperature of the opto-chemical transducers and thereby change their response amplitude. In order to avoid such complications, the test setup is typically driven using constant and relatively high gas flows up to 1000 standard cubic centimetres per minute (sccm) or 500 sccm in case smaller test chambers are used. Such high flow rates also allow for a rapid exchange of the gas atmospheres inside the test

chambers. The volume of test chambers that are used in this thesis is in the range of approx.  $1 \text{ cm}^3$  which results theoretically in a gas exchange time of  $\sim 0.1 \text{ s}$ . Of course the real gas exchange time is expected to be larger as turbulence flow conditions and vortices may occur inside the measurement chamber. These gas exchange times also set a lower limit to the measurable gas response and recovery speeds of the opto-chemical transducers.

Besides flow and gas composition, the gas pressure can also be adjusted. The pressure ranges from approx. 100 up to 2000 mbar (abs.) using a downstream pressure controller (Bronkhorst) and a suction pump for providing vacuum. Typically the pressure level is set to the laboratory's ambient pressure by detaching the vacuum pump and the pressure controller.

The gas test rig is controlled by a LabVIEW program enabling long time measurements. Time constants of gas sensors are often mainly determined by adsorption and desorption processes which can range in the orders of minutes or hours.

## 3.2 InGaN/GaN optical probing

The experimental part in this thesis involves photoluminescence probing of InGaN nanowire samples. In this section the principle of manufacturing the nanowire transducers is explained and the optical and mechanical setup of the sensor systems.

### 3.2.1 InGaN/GaN nanowire transducer

The growth of the InGaN/GaN nanowire arrays, using a plasma assisted molecular beam epitaxy process (PAMBE), was carried out at the laboratories of the University of Gießen. For this reason only a brief overview of the deposition process is given. More detailed information about these kind samples can be found for instance in ref. [22,23,89].

The InGaN/GaN nanowire samples used in this thesis were grown on a silicon substrate with a (111) surface orientation. As described in chapter 2, the lattice constant of silicon (111) is close enough to the GaN lattice constants to allow for the growth of

high-quality nanowires. The molecular beam epitaxy (MBE) growth process was carried out without any catalyst for triggering the GaN crystal growth. The process is self-organised and the nanowires grow at arbitrary sites as indicated in Figure 3.2 (a). The widths and heights vary and are strongly dependent on the MBE growth parameters. Typically their widths ranged from a few tens of nm to slightly over 100 nm while their height ranged from one to several  $\mu\text{m}$ .

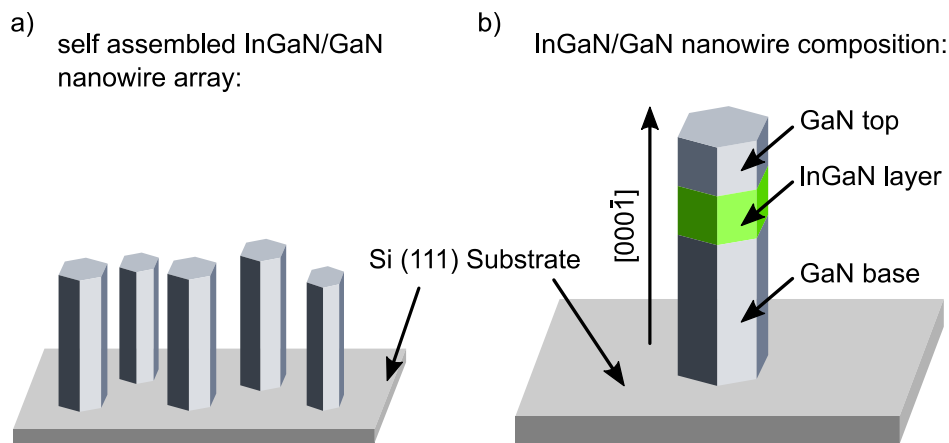


Figure 3.2. a) MBE nanowire growth starting from heated silicon substrates results in arrays of InGaN/GaN nanowires with slightly different dimensions. b) Sketch of a typical nanowire setup. A GaN base is followed by a lower-bandgap InGaN layer and an on-top GaN layer.

By changing the MBE process settings during the growth process it is possible to build up nanowires consisting of multiple materials. A typical example is shown in Figure 3.2 (b). This example contains an InGaN layer inserted in between the GaN base layer and the GaN top layer. The result is an InGaN/GaN heterojunction with unique optical properties which can be engineered according to the application requirements imposed on the nanowires.

## Samples

InGaN/GaN samples provided by the University of Gießen for gas sensing purposes, grown on a silicon (111) substrates, all have a GaN base. The total height is in the range of  $1\ \mu\text{m}$  and the width is between 50 and 100 nm. As the sketch of a representative nanowire in Figure 3.2 (b) indicates, a middle layer with an InGaN composition can be inserted between a GaN base and a GaN top part. The InGaN part was grown

under a simultaneous flux of Ga and In during the MBE deposition. The growth temperature had to be reduced during the InGaN part as InN is less stable than GaN during high-temperature growth.

The schematic drawing in Figure 3.2 (b) shows an isolated nanowire. However, the MBE growth process on a bare silicon (111) substrate results in a dense arrangement of neighbouring InGaN/GaN nanowires. In Figure 3.3 (a) a scanning electron microscope (SEM) graph shows an on-top view onto an InGaN/GaN NWA grown on silicon. The top view reveals the hexagonal shape of the nanowires and the density of the nanowires on the substrate (approx. 80 per  $\mu\text{m}^2$ ). The distance between neighbouring nanowires is in the range of their diameters, i.e. in between 50 and 100 nm.

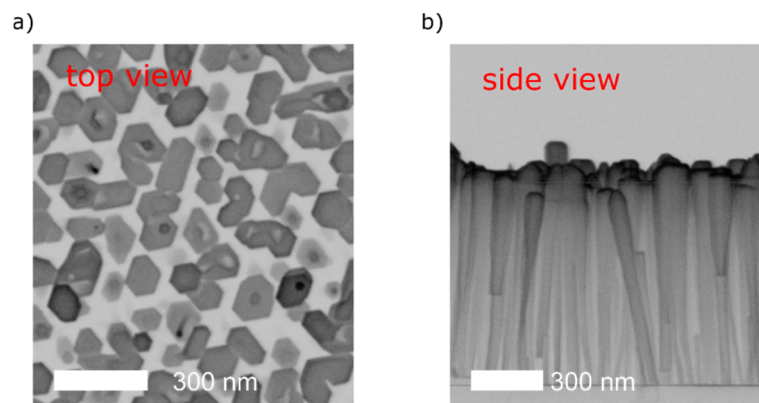


Figure 3.3. SEM graphs of a nanowire ensemble grown by a self-assembling MBE growth process under nitrogen rich conditions. a) The diameters of the hexagonally shaped nanowires is approx. between 50 and 100 nm. b) The height of these nanowires is in the range of 850 nm.

Figure 3.3 (b) shows a vertical cross section of the NWA, revealing a grass-like superstructure. This set of nanowires is approx. 800 nm high, each nanowire featuring a GaN base and an InGaN/GaN top. Due to discrepancies in the lattice constants between the GaN and InGaN layers these nanowires experience a widening of their diameters starting approx. around midterm of the nanowire growth. This view also emphasises the density of nanowires. When it comes to gas sensors a large surface to volume ratio of the transducer is advantageous for a good sensor response as the chemical interactions occur at the nanowire surfaces, while the radiative recombination processes, which constitute the output signal, occur in the nanowire bulk.

The InGaN/GaN nanowires investigated here, exhibit a pronounced PL in the green spectral range with a maximum peak at about 2.5 eV [22]. The origin of the PL is found in the InGaN part of the nanowire [22,90]. Figure 3.4 (a) shows a PL spectrum measured over a wide range of temperatures on samples similar to those shown in Figure 3.4 (a). The PL was excited using a Helium Cadmium (HeCd) laser with a wavelength of 325 nm. When probing the photoluminescence of an array of nanowires the PL spectrum is an average over many individual nanowire spectra. As the nanowires slightly vary in size and composition, the spectra vary as well. Therefore the PL spectra shown in Figure 3.4 (a) are broadened versions of individual nanowire spectra.

The PL is thermally quenched when the temperature is increased. But even at temperatures above 375 K the PL is relatively high and, as it will be shown in the results sections that follows, that the PL signal is strong enough even at 150°C. In Figure 3.4 (b) the temperature dependency of the maximum PL signal is shown.

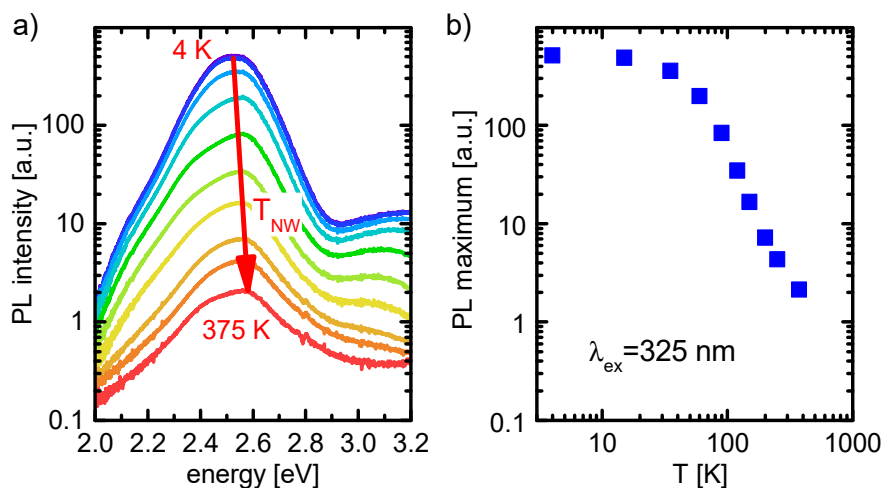


Figure 3.4. a) PL emission spectra of the InGaN/GaN transducers measured at different temperatures between 4 K and 375 K. b) Temperature dependence of the extracted peak luminescence intensity. (Data provided by Uni Gießen)

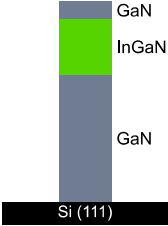
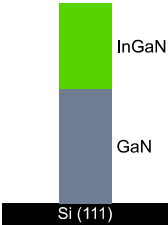
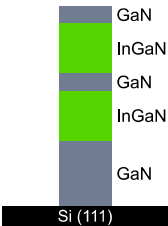
Additionally to the temperature-induced quenching of the photoluminescence the PL peak shows a slight blue shift. The PL emission at elevated temperature is energetically higher than those at lower temperatures. This effect is caused by local In accumulations that increases the local potential minima and therefore lower the energy of PL photons. This is a commonly known effect in InGaN alloys [22].

## Overview NWA samples

The InGaN/GaN nanowire samples that were employed in this thesis are listed in Table 3.1. All samples consist of a GaN base that was grown on the silicon (111) substrate. Then an InGaN layer was grown on top of the base. Sample A additionally was covered with a GaN top layer and sample C even consists of two InGaN layers separated by a GaN barrier layer. In the right column of Table 3.1 the growth times for each layer are listed. The growth duration correlates to the height to the corresponding layer.

The characteristics of the PL emission spectra depend on the nanowire composition. In order to be able to compare measurements, most measurements in this thesis were carried out using sample type A. However similar results are expected for the other type of samples as the PL signal generally was integrated with the existing detection unit. Slight variation of gas responses might be applicable in future projects using pattern recognition techniques when transducer arrays with different sample types are employed.

Table 3.1. Overview of samples that were measured in this thesis. Sample A, B, C consists of a GaN base followed by one or more layers of InGaN. Growth times and PL emission peak (405 nm excitation) are listed in the right column.

	NW Composition	NW Growth parameters
<b>Sample type A</b>		Base GaN: 135 min InGaN section: 90 min Top GaN: 4 min Peak luminescence: 2.59 eV
<b>Sample type B</b>		Base GaN: 135 min InGaN section: 90 min Peak luminescence: 2.41 eV
<b>Sample type C</b>		Base GaN: 135 min InGaN sections: 45 min GaN barriers and top: 4 min Peak luminescence: 2.65 eV

### 3.2.2 PL sensor setups

In this thesis two different sensor setups were used for probing the photoluminescence of the above-described InGaN/GaN nanowire ensembles. The sensors do not take spectra of the nanowires but an integrated PL value over a relatively broad spectral range. A near ultraviolet LED with 365 nm peak wavelength is used as an excitation source. The photon energy is high enough to generate electron hole pairs in the GaN bulk material which has a band gap of 3.4 eV. The PL light detection can be performed with a photodiode or, if a higher sensitivity is required, a photomultiplier can be attached to the system.

For extracting the information contained in a reduced or enhanced photoluminescence two different setups were used. Both setups use the same UV LED as an excitation energy source. The two different PL measurement setups were used in different ways with light guides. The first employs a glass fibre optical wave guide and the second a dichroic mirror system.

### Optical fibre setup

The first configuration is shown in Figure 3.5 (a). Here an optical fibre separates the optical components from the gas measurement chamber. The system allows to be operated in harsh environment and combustible atmospheres as long as the electronics of excitation and detection unit is sufficiently separated by the glass fibre.

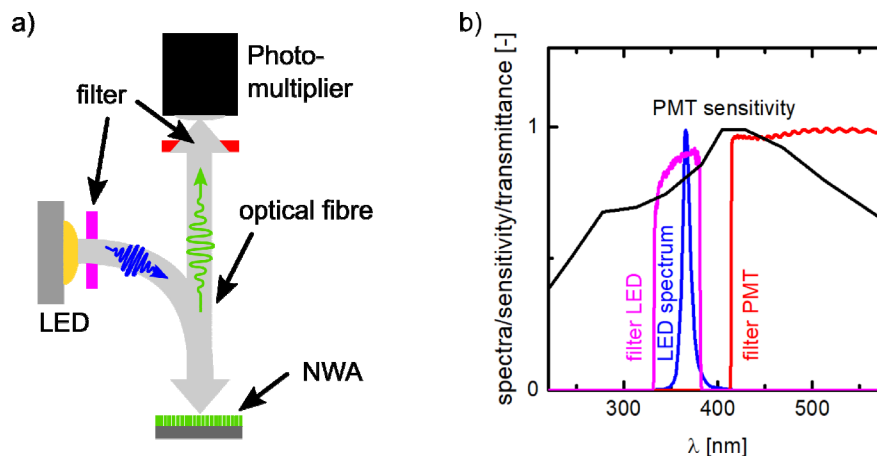


Figure 3.5. a) Schematics of the optical setup featuring two light fibres for light guidance and an optochemical InGaN/GaN transducer. The fibre itself is inserted into the gas tight measurement chamber. b) Spectra of the key optical components of the PL sensor setup

The excitation photons are produced with an UV LED (365 nm, Roithner UVLED-365-330-SMD [91]). The first band pass filter is inserted to cut off the longer wavelengths of the LED spectrum. The characteristics of the optical components are shown in Figure 3.5 (b). The light is coupled into the optical fibre which is guided into the gas measurement chamber. An InGaN/GaN nanowire sample, as described in the section before (see e.g. Figure 3.3), with a sample size of approx. 1 cm<sup>2</sup> is placed in the measurement chamber. The gas tight chamber can be actively heated by heat rods and a

temperature controller. The system can be operated from room temperature up to 150°C without damaging the optical fibres. The excitation light shines directly onto the nanowire sample which creates electron-hole pairs in the InGaN/GaN semiconductor. Recombination of the electron-hole pairs generates PL which can be reduced or enhanced depending on the surface reactions that occur on the transducer surface. The PL light is coupled into the fibre and due to the y-shape of the optical fibre package is partially guided to the detection unit. The PL detector is a photomultiplier tube with adjustable gain (PMT, Hamamatsu H5784 [92]). As shown in Figure 3.4 (a), the spectral response is broad-banded which requires an additional filter before the detection unit, cutting out the shorter wavelengths of the reflected excitation light.

The fibre based configuration loses a large amount of light as most of it is not optimally coupled into and out of the fibre. The PL detection unit, therefore, has to feature a sufficiently high gain. Additionally, the excitation LED has to be a power LED with an optical power of several hundred mW.

The LED is driven by an adjustable constant current power supply (Peak electronics) and can be operated up to 1200 mA. The photomultiplier output current is internally converted to an output voltage by an internal current to voltage converter. Thereafter, a National Instruments data acquisition board (NI 6211) connected to a LabView program logs the photomultiplier's output signal. Additionally, the LabView program controls the output current of the constant current driver of the LED and it optionally allows pulsed excitation light to be produced. The on-time of the LED can be reduced to a couple of milliseconds. These on-times exceed the lifetimes of photogenerated charge carriers in semiconductors by several orders of magnitude. The reason for pulsing the LED is to minimize the heat generation inside the LED and to minimize the operating time as the LED degrades over time.

### Dichroic mirror setup

The second opto-chemical sensor system used in this thesis is shown in Figure 3.6 (a). The central item in this set-up is a dichroic mirror that separates the excitation light path from the PL light path to the detector.

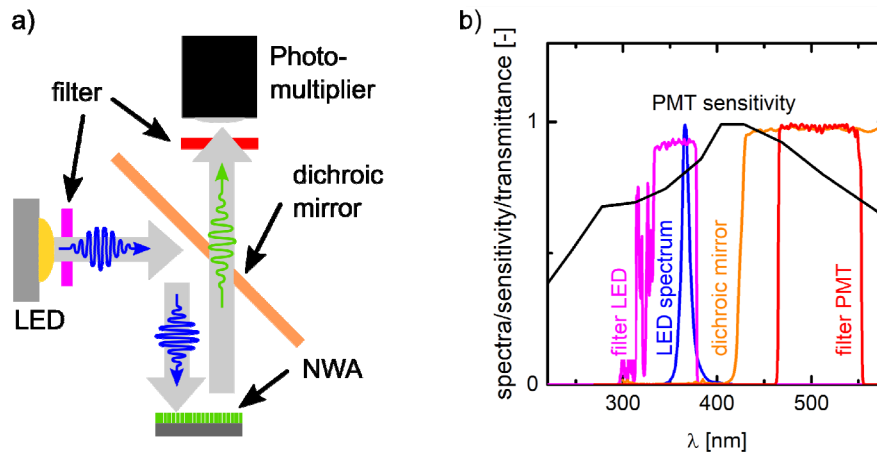


Figure 3.6. a) Optical setup for of the InGaN/GaN nanowire transducer using a dichroic mirror for guiding excitation and photoluminescence light. b) Spectra of the key optical components of the PL sensor setup

The properties of the key optical components reveal from Figure 3.6 (b). The excitation source is similar to the fibre optic sensor described above. An UV LED (365 nm, Roithner UVLED-365-330-SMD [91]) emits the excitation photons and the lower-energy photons are filtered out by an initial excitation filter. The dichroic mirror has a high pass character and higher-energetic light, as emitted by the LED, is reflected under an angle of  $45^\circ$  towards the gas measurement chamber containing the InGaN/GaN transducer. A sapphire lens separates the sensor optics from the measurement chamber. The focal lengths of the lenses are chosen in a way that the illumination covers almost the entire InGaN/GaN transducer which has a square footprint with 1 cm side length. The transducer itself is mounted on a heated copper sample holder plate. The sample holder is temperature-controlled and can be heated up to  $150^\circ\text{C}$ . Upon UV illumination the transducer emits PL light which is similarly quenched or enhanced depending on the gas ambient within the test chamber as for the fibre optics setup described above. The green-coloured PL light passes through the sapphire lens, the dichroic mirror and the detection filter. Any residual excitation light should be filtered out and the detector should solely detect PL light emitted by the transducer.

The losses of light in the fibre-setup are huge when compared to the dichroic mirror setup. Additionally, the illuminated spot is small in the fibre variant ( $A_{illum} < 1 \text{ mm}^2$ ) and it is 100 times larger in the dichroic mirror setup ( $A_{illum} \approx 1 \text{ cm}^2$ ). As a consequence the input light intensity in the fibre setup has to be orders of magnitude higher

than in the dichroic setup when using the same PL detection technique. Whereas in the fibre setup a photomultiplier tube (PMT, Hamamatsu H5784 [92]) has to be used to detect the small amounts of PL light, a simple silicon photo diode offers enough sensitivity in the dichroic mirror case. When using a PMT in the dichroic mirror setup it is possible to investigate the influence of excitation light intensity on the PL response in addition to other parameters such as temperature and, of course, the test gas ambient.

Operation and data acquisition can be performed using similar electronics as for the fibre based setup with a commercial LED driver block and a National instruments DAQ board. More flexibility provides additional benchtop equipment such as constant current supplies (Keithley source meter K2400) and high precision bench multimeter (Keithley K2001). Both instruments can be operated with a custom-designed LabView program. The program allows adjustment of the LED current which is almost proportional (see Figure 3.7) to the output intensity and switching from continuous to pulsed operation with adjustable duty cycles.

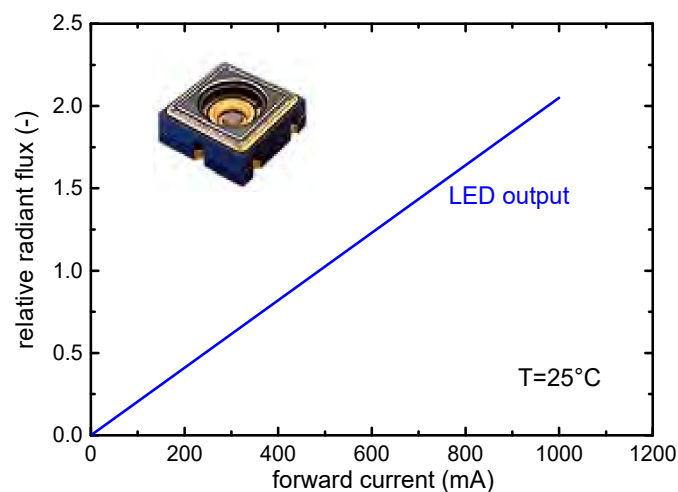


Figure 3.7. Relative radiant flux and forward current of the LED (Roitner UVLED 365 330 smd) shows a linear dependency. Extracted from datasheet [91].

## 4 Gas response of GaN/InGaN nano-optical probes

The InGaN/GaN nanowire transducers exhibit a broad-range gas sensitivity. In this section the gas response towards different sets of gases is presented. The gases tested comprise the main air constituents of oxygen and water vapour as well as typical air contaminants, such as nitrogen dioxide ( $\text{NO}_2$ ) and ozone ( $\text{O}_3$ ). A third test gas category is hydrocarbons, i.e. a group of target gases relevant to a wide variety of gas sensing applications. Besides pure aliphatic hydrocarbons also species with OH-functional groups, i.e. alcohols are investigated.

The experiments shown in this section were carried out using the gas test rig and the PL probing setup as already described in chapter 3. During the gas sensing tests, a constant total flow of either 500 or 1000 sccm was maintained upon switching from background gas, i.e. nitrogen or synthetic air, to mixtures of test gas and background gas with different mixing ratios. Both the fibre optic and the dichroic mirror setups were used in these experiments.

### 4.1 General response behaviour

In Figure 4.1 a set of data points is shown where the transducer temperature was varied from room temperature up to  $150^\circ\text{C}$  under a constant flow of pure synthetic air. As a measure of the PL intensity the photomultiplier output voltage was used. The data show that the PL intensity decreases with temperature but still remains reasonably high up to the temperature limit of our gas sensing tests. While a linear extrapolation of the observed data suggests that the PL signals may actually stay detectable up to temperatures of more than  $300^\circ\text{C}$ , the high-temperature limit in practical gas sensing tests was limited to about  $150^\circ\text{C}$  by the temperature durability of the mechanical components in the two PL probing setups. The background PL intensity levels

observed, either in synthetic air or in nitrogen, served as references for the assessment of those PL intensity changes that occurred upon exposure to test gases other than nitrogen or synthetic air.

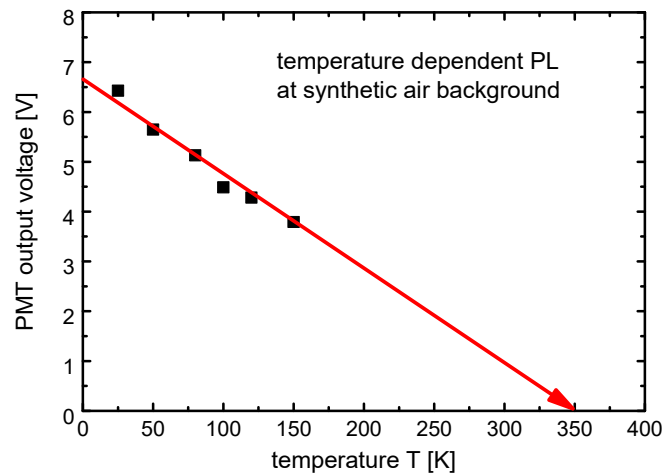


Figure 4.1. Variation of the PL baseline signal with transducer temperature for a NWA transducer operated in a background of pure nitrogen.

In the following gas response data are shown as obtained for various gases and at different transducer temperatures. As an illustrative example, Figure 4.2 shows a set of gas response data which are typical for this chapter. In these measurements the InGaN/GaN transducers were operated at room temperature (a) and at 120°C (b) while applying the test gas sequence illustrated in (c). In the first set of experiments exposure pulses with increasing ethane concentrations admixed to synthetic air were used. In the second and third sets, the ethane was replaced by methane or ethanol, respectively. In the last experiment  $\text{NO}_2$  was used, also diluted in synthetic air. The PL response is the change in the PL intensity relative to the level solely in background gas at the same measurement temperature. In the case of the measurement shown in Figure 4.2, the PL is enhanced for all gases except  $\text{NO}_2$ , which falls into the category oxidising gases, which are all PL quenchers, as shown later in this chapter.

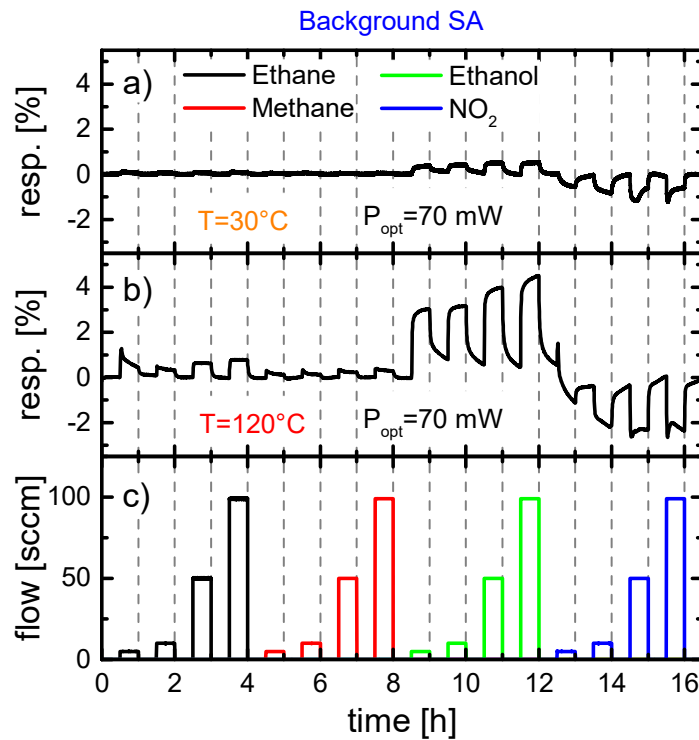


Figure 4.2. Response of an InGaN/GaN transducer to different sets of gas exposures as observed at two different transducer temperatures. Background gas was pure synthetic air.

From this series it becomes evident that upon changing the gas atmosphere the PL intensity can change in both directions: whereas hydrocarbons increase the PL,  $\text{NO}_2$  decreases the PL.

For the purpose of interpretation, gas response values were extracted from the raw data using

$$R_{gas} = \frac{V_{gas} - V_0}{V_0} \quad (4.1)$$

with  $V_0$  and  $V_{gas}$  being the photomultiplier output voltages under clean carrier gas and test gas exposure, respectively. The photomultiplier output voltage correlates with the radiative recombination rate of the InGaN/GaN transducers. According to this response definition we get a positive response in the case of PL enhancement ( $V_{gas} > V_0$ ) and a negative response in the case of PL quenching ( $V_{gas} < V_0$ ).

## 4.2 Response to oxidizing gases

### 4.2.1 O<sub>2</sub> response

O<sub>2</sub> is by far the most important background gas in gas sensing tests performed in ambient air. For this reason, the changes in the PL intensity level are important that occur as increasing amounts of O<sub>2</sub> are admixed to pure nitrogen (N<sub>2</sub>).

In Figure 4.3 the PL response to a sequence of alternating flows of nitrogen and oxygen/nitrogen mixtures is shown. In this set of measurements higher concentrations of oxygen are shown. Upon exposure to oxygen the PL intensity is quenched which is in accordance with earlier observations on GaN/AlGaN nanowire heterostructures [30]. At these high O<sub>2</sub> concentrations the PL response is almost saturated. For this reason, similar measurements were also carried out over a much wider concentration range extending from several hundred ppm up to 20%. In addition, all measurements were repeated at higher temperatures to assess the temperature dependence of the PL response.

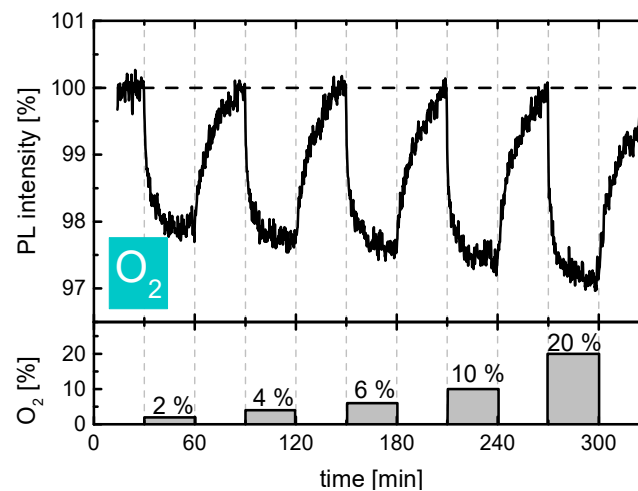


Figure 4.3. Response of the PL intensity to increasing concentrations of O<sub>2</sub> admixed to a flow of dry N<sub>2</sub>. During this experiment the transducer was kept at room temperature.

The PL quenching behaviour indicates an enhanced non-radiative recombination rate of photogenerated charge carriers at the InGaN/GaN surface. As O<sub>2</sub> exhibits a positive electron affinity of approx.  $E_{A,O_2} = 0.45$  eV [93], adsorbed oxygen is likely to trap electrons thus forming negatively charged adsorbates. These charged adsorbates in turn

attract photogenerated holes from the interior of the nanowires which allows them to recombine non-radiatively with the trapped electrons.

The O<sub>2</sub> response velocity at different temperatures is visualized in Figure 4.4. There, the gas response data, gathered at temperatures between 25°C and 150°C, are overlaid. For comparison the response curves were scaled with respect to their maximum values, meaning that 100 % corresponds to the maximum quenching effect at each temperature. The data reveal that higher temperatures reduce both the response and the recovery time constants of the PL quenching response. If one assumes a Langmuir type adsorption process with adsorption and desorption time constants following Arrhenius-type temperature dependencies, a much stronger impact of temperature would have been expected. This lack of temperature sensitivity likely arises from the fact that at the surfaces of the InGaN/GaN transducers non-thermal UV activated processes interfere with purely temperature-activated ones. On the other hand, directly measured response velocities are also likely to be limited by system-related time constants, as for instance gas exchange times in the gas test rig or in the PL response setup. In order to minimize such external effects, all PL response tests were carried out at comparatively large gas flow rates [71,72,94–96].

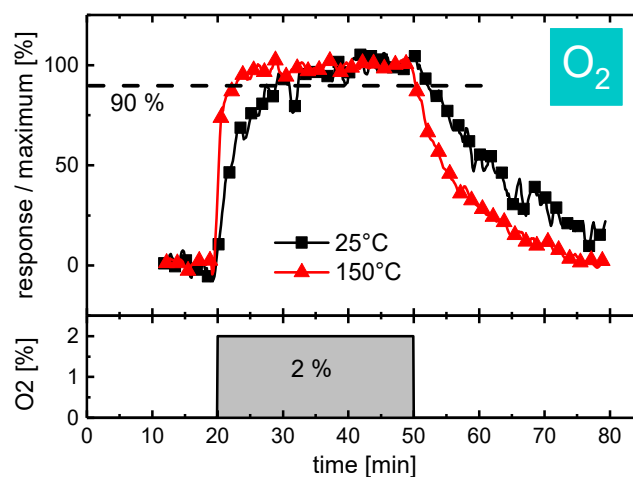


Figure 4.4. Response to an O<sub>2</sub> pulse applied in a background of dry N<sub>2</sub> and as measured at increasing transducer temperatures. For clarity the responses have been normalized to their values attained at the end of the O<sub>2</sub> pulses.

A detailed discussion of the measurements will be given in chapter 5 and 6.

## 4.2.2 NO<sub>2</sub> response

The next test gas in the oxidizing gases series is nitrogen dioxide. NO<sub>2</sub> is a toxic gas and a potential threat for the population in cities with heavy traffic as NO<sub>2</sub> derives from combustion engines, especially from diesel engines [97]. The air composition of the ambient atmosphere is approx. 80 % nitrogen and 20 % oxygen while air contaminants such as NO<sub>2</sub> normally abound in the range of ppm or sub-ppm levels. The NO<sub>2</sub> test gas coming from the gas test rig is admixed to synthetic air which simulates the NO<sub>2</sub> contamination in the ambient air. As NO<sub>2</sub> is more strongly oxidising than O<sub>2</sub> ( $E_{A,NO_2} = 2.27$  eV [98]), it competes for electrons, photogenerated in the interior of the InGaN/GaN nanowires with the much more numerous O<sub>2</sub> molecules in the background synthetic air. Additionally, this competition also involves a competition for the same kinds of surface sites.

In Figure 4.5 the PL response of an InGaN/GaN transducer to a sequence of NO<sub>2</sub> gas pulses ranging from 1 ppm to 50 ppm is shown. Similar to solely sensing oxygen as in the previous section, the PL response is a quenching one and occurs at much lower concentrations of NO<sub>2</sub> than the O<sub>2</sub> response. The minimum detectable NO<sub>2</sub> concentrations are orders of magnitude lower than those for O<sub>2</sub>, amounting to approx. 500 ppb only. Again, as for O<sub>2</sub>, NO<sub>2</sub> exposure tests were performed at increasingly higher transducer temperatures as discussed further below.

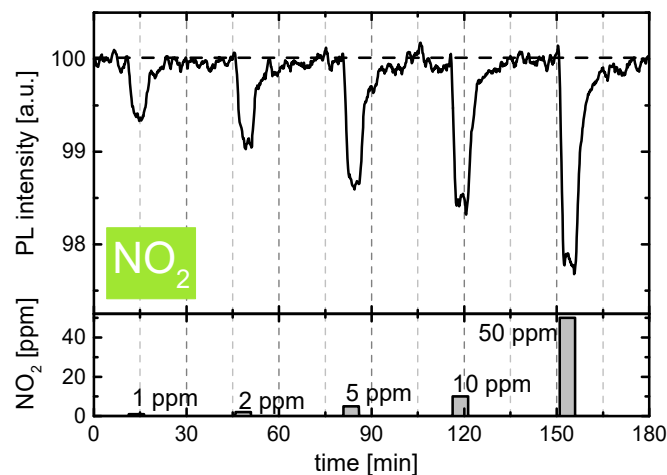


Figure 4.5. Response of the PL intensity to a sequence of NO<sub>2</sub> exposure pulses with concentrations ranging between 1 ppm and 50 ppm with the transducer being kept at room temperature.

### 4.2.3 O<sub>3</sub> response

Like NO<sub>2</sub>, ozone can also be found in the ambient air and can be harmful to the human health. The gas tests were carried out with synthetic air as background gas and ozone was created by an ozone generator. In this device the oxygen of synthetic air is radicalized by UV light exposure. Figure 4.6 shows the PL response of an InGaN/GaN sample when exposed to a series of ozone exposure pulses. Again, the background was synthetic air and a constant gas flow of 1000 sccm was maintained. The accessible ozone concentration with this setup and this air flow ranged from approx. 90 ppb up to 330 ppb. It can be seen that even at the very lowest concentrations ozone is able to quench the photoluminescence below its level in synthetic air. Similar to the measurements with NO<sub>2</sub> the O<sub>3</sub> exposures occurred in parallel with the oxygen exposures originating from the synthetic air backgrounds, meaning that two molecules with PL quenching properties are simultaneously present. In order to assess the temperature dependence of the O<sub>3</sub> response, this series of measurements was again repeated at increasingly higher temperatures.

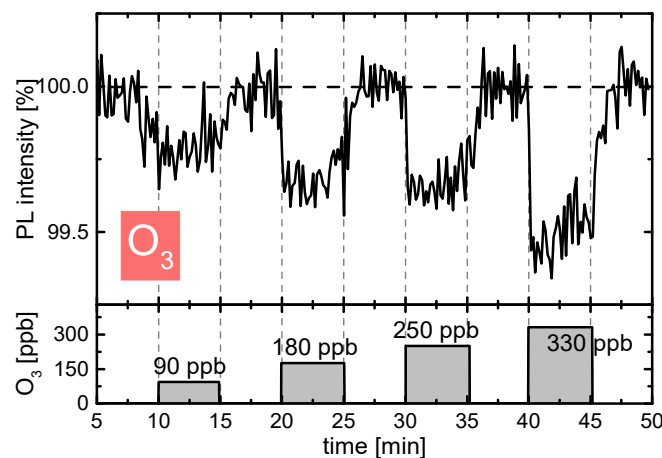


Figure 4.6. Variation of the PL intensity in response to a sequence of O<sub>3</sub> concentration steps between 90 and 330 ppb applied at room temperature.

Similar to NO<sub>2</sub>, O<sub>3</sub> is highly reactive with a high electron affinity  $E_{A,O_3} = 2.103$  eV [99]. Consistent with this high electron affinity, minimum detectable O<sub>3</sub> concentrations of about 50 ppb were observed.

### 4.3 Response to reducing gases

In this section the PL response of the NWA transducers towards reducing gases is presented. These gases include alcohols and aliphatic hydrocarbons. In contrast to oxidizing gases, reducing gases have negligible or negative electron affinities [100]. Therefore, these molecules should not be able to trap photogenerated electrons and a reduction of the PL is not to be expected.

At the beginning of this chapter, Figure 4.2 showed the response for ethane, methane, ethanol and  $\text{NO}_2$  revealing some initial information: at room temperature neither ethane nor methane exhibited any sizeable gas response. This has been previously observed with  $\text{H}_2$  and ethane [101]. At elevated temperatures a PL enhancement for ethane and ethanol can be observed. Other than  $\text{H}_2$  and ethane, ethanol shows a much stronger enhancement effect, already at concentrations one order of magnitude lower than the other hydrocarbons, both at room temperature and at  $120^\circ\text{C}$ . As expected  $\text{NO}_2$  reveals as a quenching gas, showing a very different behaviour than all hydrocarbons (see previous section or ref. [76]).

#### 4.3.1 Alcohol response

In Figure 4.7 PL response data for ethanol diluted in  $\text{N}_2$  (a,b) and SA (c,d) are shown. The ethanol pulses, depicted in panel (e), follow a downward staircase sequence. The data clearly show that the responses for ethanol with nitrogen background are negligible at both temperatures. When the background gas is SA, the ethanol shows a clear enhancing effect, already at room temperature and even more at elevated temperatures. The response values obviously scale with the ethanol concentrations.

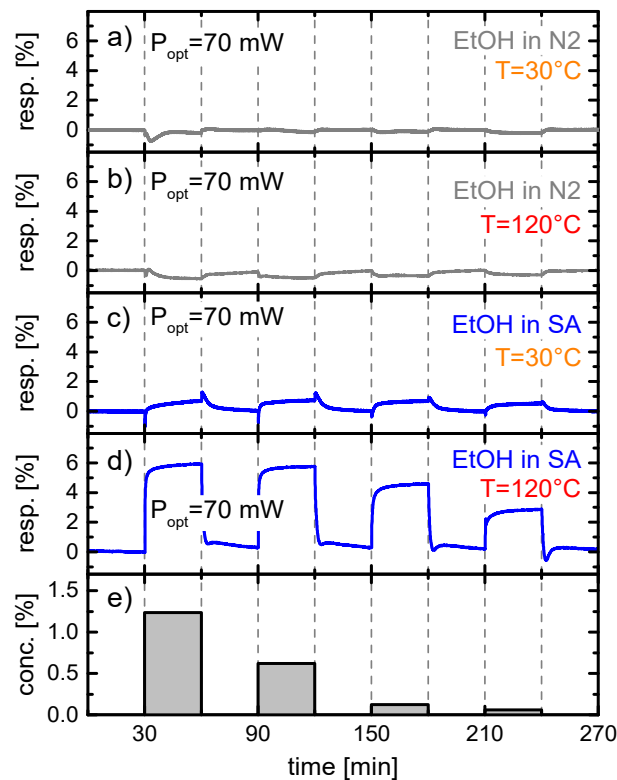


Figure 4.7. PL response of an InGaN/GaN transducer towards staircases of ethanol concentration steps as applied in backgrounds of N<sub>2</sub> (a, (b) and SA (c, d). Transducer temperature and excitation light conditions are indicated in the insets. Panel (e) shows the timing of the ethanol and background gas flows

Similar measurements as for ethanol were repeated for alcohols with longer and shorter C-chain backbones. Besides ethanol, which was presented above, the alcohols methanol and propanol were tested. Again, the measurements were carried out at two temperatures (30°C and 120°C) and with different background gases (N<sub>2</sub> and SA). In Figure 4.8 the observed gas responses are presented. On the left hand side, the results with nitrogen background are shown. Obviously, no response is observed regardless of analyte molecule or transducer temperature. This is in agreement with the previously performed ethanol measurements. On the right hand side, the results of similar measurements with SA background are shown. The response is comparatively small at 30°C but increases up to levels of approx. 5-6% at 120°C. The minimum detectable concentrations scale in the order of several hundreds to several thousands of ppm, varying with the carbon chain length following the order of propanol, ethanol, and methanol, i.e. in inverse order with the stability of the alcohols.

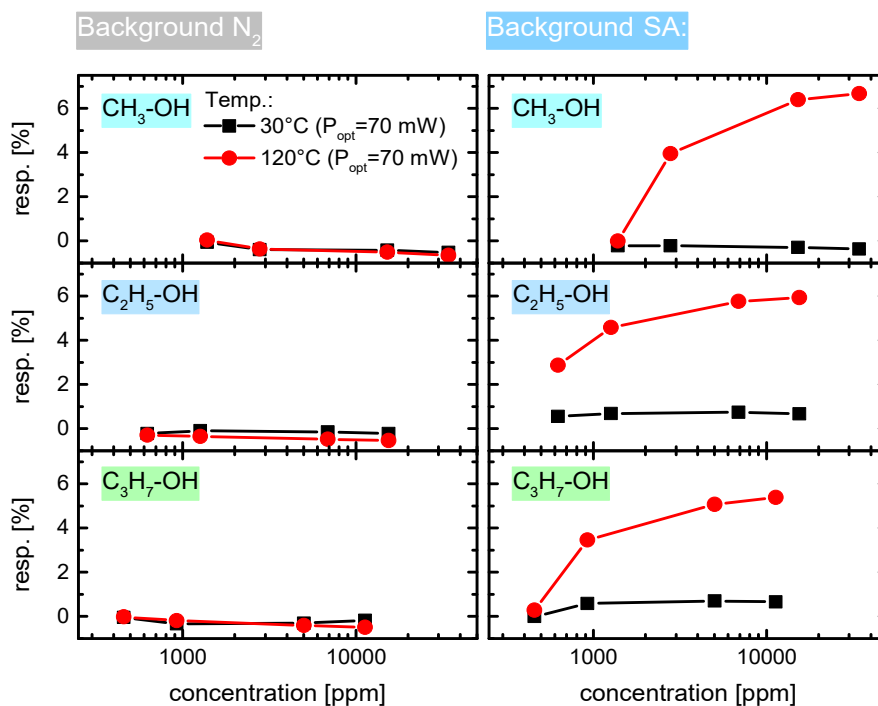


Figure 4.8. Impact of background gas and transducer temperature on the PL enhancement effect of alcohols with C<sub>1</sub> to C<sub>3</sub> chain lengths.

### 4.3.2 Aliphatic hydrocarbons

Similar data as for the alcohols presented above, were also assessed for a range of aliphatic hydrocarbons. Aliphatic hydrocarbons are non-cyclic and can be saturated containing only single C-C bonds or unsaturated containing double C-C bonds. In contrast, however, they do not contain any functional groups such as the hydroxyl groups of the previously discussed alcohols. A set of saturated hydrocarbons with varying C-chain lengths was tested. Methane (CH<sub>4</sub>), ethane (C<sub>2</sub>H<sub>6</sub>) and propane (C<sub>3</sub>H<sub>8</sub>) measurements are shown in the left-hand graphs of Figure 4.9. Similar to previous measurements, the transducer temperature was set to 30°C and 120°C. A very small enhancement effect is observable at elevated temperatures. The response seems to increase with the C-chain lengths of the molecules. Except for propane, the room-temperature responses are within the limits of the measurement accuracy and can therefore be neglected.

On the right-hand side of Figure 4.9 graphs are shown that summarize the responses observed on a set of hydrocarbons with the same carbon chain length (3), but differing in bond order; i.e. single, double and triple C-C bonds. Here, it is apparent that the responses of the unsaturated molecules are higher and that the responses set in earlier when the bond order is increased. This latter effect may be attributed to the stronger C-C bonds in saturated as compared to unsaturated hydrocarbons. Essentially, this explanation is in line with the one proposed for the effect of different carbon chain lengths.

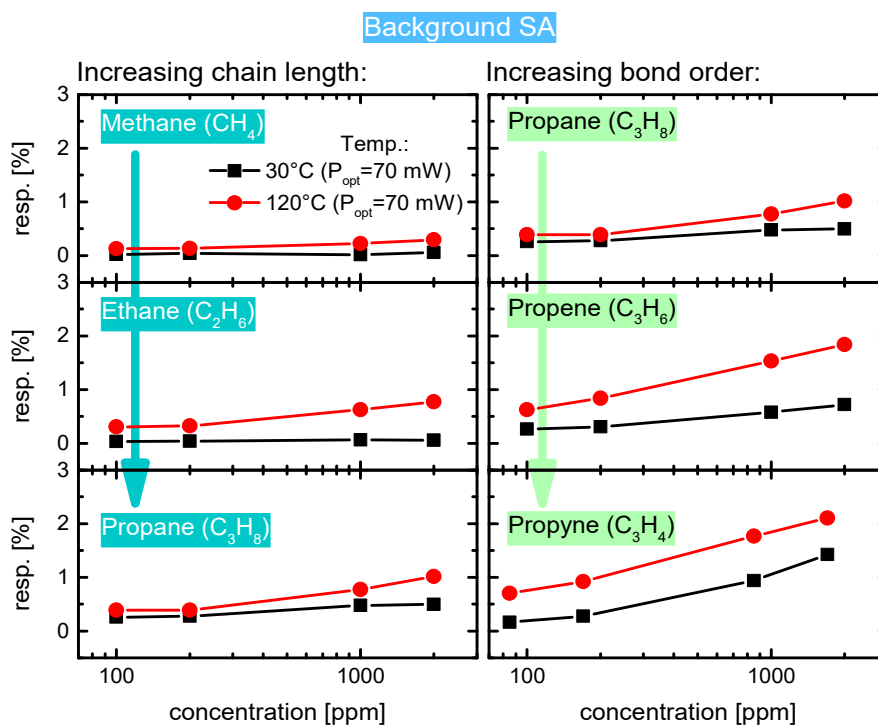


Figure 4.9. (left) scaling of PL enhancement effect with hydrocarbon chain length; (right) scaling with bond order, i.e. single-, double-, triple C-C bonds.

### 4.3.3 General observation of the hydrocarbon response

Overall, the data showed that the PL response of the NWA transducers is sensitive towards reducing gases. The effect is small for aliphatic hydrocarbons but more pronounced for alcohols. In both cases background oxygen is mandatory for obtaining a sizable response. An explanation for this observation could be that hydrocarbons, in contrast to oxidizing gas species, follow an indirect sensing mechanism, similar to the

one on conventional MOX surfaces, where reducing analytes are detected indirectly through the consumption of surface oxygen ions. Unlike in resistively interrogated MOX gas sensors, UV light activation in InGaN/GaN transducers are likely to enhance the oxidation rate at moderate surface temperatures. On InGaN surfaces, such oxidation processes firstly reduce the density of PL quenching surface oxygen ions and, secondly, these also produce  $\text{CO}_2$  and  $\text{H}_2\text{O}$  as combustion products. While  $\text{CO}_2$  shows no significant PL response, water is able to enhance the PL as shown in Figure 4.10 and as further explained in the next section. Both effects, surface oxide reduction and water production potentially lead to an enhanced overall PL response.

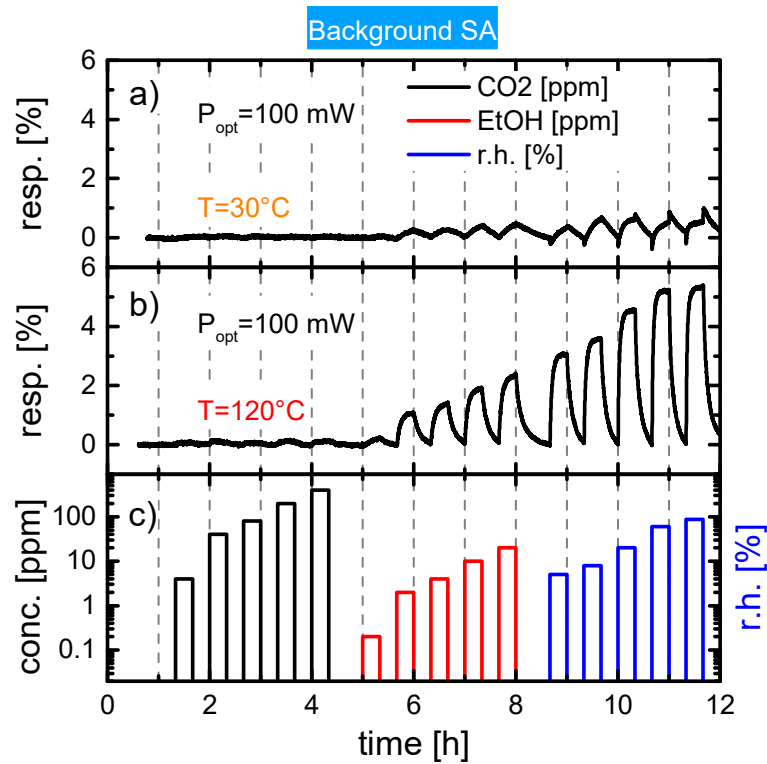


Figure 4.10. PL response towards  $\text{CO}_2$ , EtOH, and  $\text{H}_2\text{O}$ . All measurements were performed in a background of SA and at transducer temperatures of  $30^\circ\text{C}$  (a) and  $120^\circ\text{C}$  (b), respectively.

## 4.4 Response to H<sub>2</sub>O vapour

Besides O<sub>2</sub>, water vapour is the second most abundant air constituent. As a consequence, it is also present in most conceivable gas sensing scenarios. In this section the results of PL measurements at various H<sub>2</sub>O concentrations are presented. In a first measurement series the optical power of the LEDs was set to 7 mW. Losses due to filters and lenses are neglected. The measurement consists of a series of water vapour exposure pulses with the relative humidity (r.h.) ranging from approx. 4% to 85%. The temperature of the nanowire sample for each single series of water pulses was kept constant. The same series was then repeated at three different temperatures. Figure 4.11 shows two measurement sequences with the transducer temperature set to 30°C and to 120°C, respectively. The PL response is normalized to the initial value of the measurement. The data show that upon onset of each water pulse PL quenching is initially observed. At transducer temperatures close to room temperature the PL signal stays quenched until the end of the water pulse. At higher transducer temperatures the PL intensity rises slowly during the humidity pulse. After terminating the water vapour flow, the PL level slowly approaches its zero-humidity baseline level again. This re-approach takes place with a long time constant of approx. 20 min, both at high and at low transducer temperature. At high transducer temperatures, however, a rapid overshoot of the PL intensity over its zero-humidity baseline level is observed before the PL actually starts to re-approach its baseline level again.

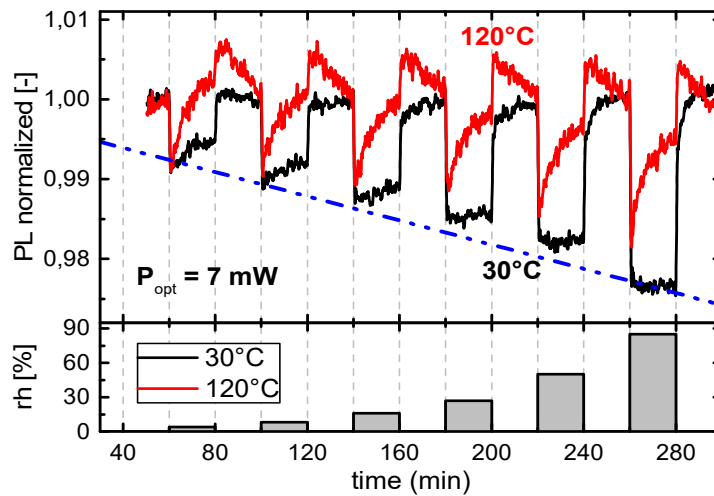


Figure 4.11. Normalized PL response to a sequence of water vapour pulses diluted in dry nitrogen gas (grey boxes). The optical excitation power was set to approx. 0.7 mW. Transducer temperatures were 30° (black) and 120°C (red).

The experiment was repeated with a higher LED excitation power. In Figure 4.12 similar data are shown, however, with the UV LED set to 200 mW optical power. The NWA transducer temperatures were again 30°C and 120°C. As observed before at lower excitation power, the PL signal is first quenched upon onset of each water vapour pulse and then turns into a less quenched or even an enhanced PL signal. In contrast to the low-excitation power case, the transition from quenching to enhancing response is much faster and more pronounced. After the termination of each water pulse a PL overshoot is observed which decays again as the transducers are operated under dry background conditions again.

When comparing low and high temperature PL signals at 200 mW excitation power one can see that the initial quenching is almost negligible and overcompensated by the subsequent enhancing phase. Furthermore the enhanced PL signal is almost independent of the r.h. value of the gas flow and seems to be saturated. The PL value for the saturated state is indicated by the red dashed line.

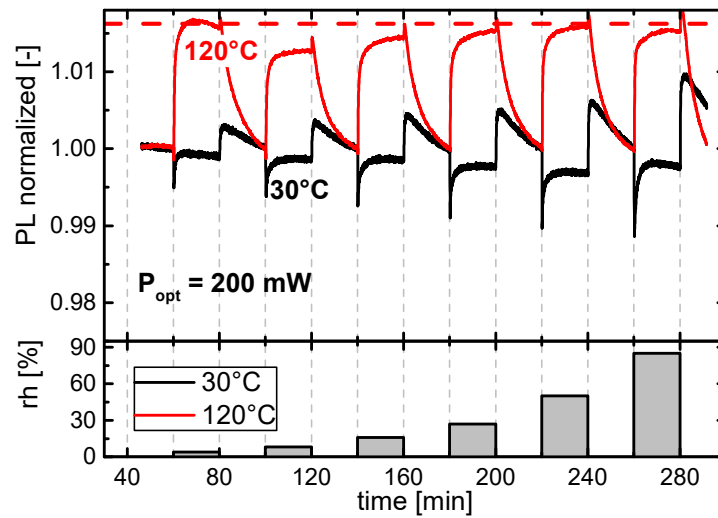


Figure 4.12. Normalized PL response as measured for series of water vapour pulses (grey boxes) at much higher excitation power ( $P_{opt} = 200$  mW). Nanowire temperatures were 30° (red) and 120°C (black).

In the following, variables connected to PL quenching phenomena are labelled with (Q) while others connected with PL enhancement are labelled with (E). As water causes both enhanced and quenched PL it is useful to distinguish both responses from each other. In the following we denote the relative PL reduction with  $\Delta PL_Q$  and the subsequent PL enhancement change with  $\Delta PL_E$ .

Not only has the temperature an influence on the PL response towards water, the excitation intensity severely affects the PL response, too. In Figure 4.13 the influence of LED intensity on the transition from initial quenching (Q) to enhancing (E) is shown. Here, the height of the water vapour pulse was set to 50% rel. humidity. The graph clearly shows how UV light promotes the enhancing effect after the initial quenching has occurred.

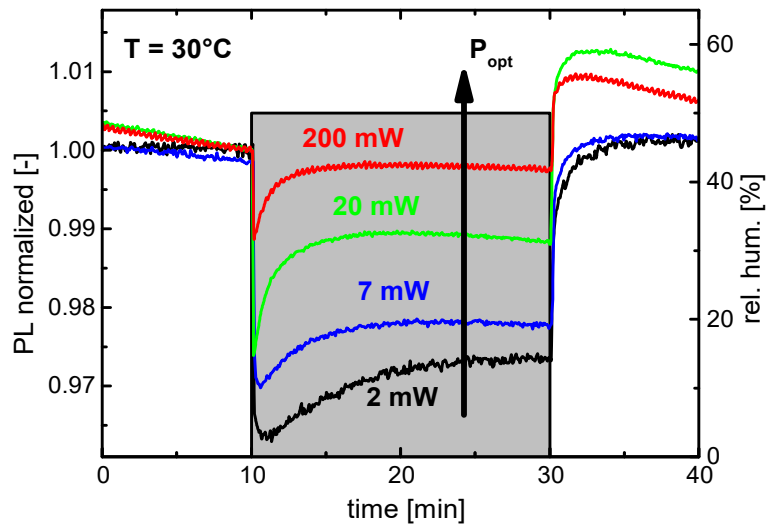


Figure 4.13. Normalized PL intensity response to a humidity exposure pulse ( $rh = 50\%$ ) applied in dry  $\text{N}_2$  ambient for different LED-light intensities.

All experiments so far were carried out in dry nitrogen background. In Figure 4.14 a  $\text{H}_2\text{O}$  exposure test was performed with an intermediate optical power level of 20 mW at a transducer temperature of  $30^{\circ}\text{C}$  and in a background of dry synthetic air. Compared to the previous results obtained in backgrounds of dry  $\text{N}_2$ , the enhancing effect in backgrounds of dry synthetic air is more rapid and more pronounced. This result is surprising on first sight as  $\text{O}_2$  was observed to cause PL-quenching when  $\text{H}_2\text{O}$  is absent. The results of Figure 4.14 therefore point to a cooperative effect of  $\text{H}_2\text{O}$  and  $\text{O}_2$  in which the oxygen seems to catalyse the Q-E transition in the PL response.

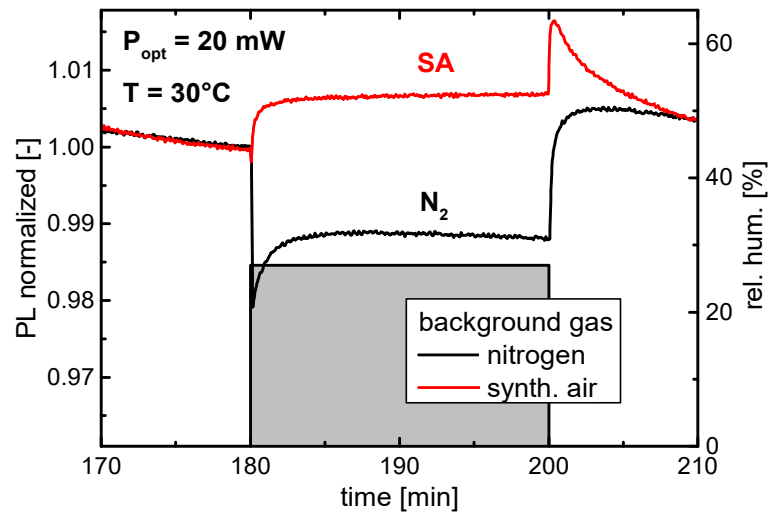


Figure 4.14. Effect of background atmosphere on the PL response to a humidity-exposure pulse: (black dataset) background of dry N<sub>2</sub>; (red dataset) background of dry synthetic air (SA).

All experiments in this section showed that water plays a double role. The first one is a PL quencher in which water creates a surface recombination channel for photogenerated charge carriers. This process is fast as shown in the short quenching response times. In contrast, the second role of water is a counteracting PL enhancer. In this situation water vapour hinders surface recombination by blocking potential adsorption sites for other PL quenching water molecules. As the enhancing effect increases with temperature or UV light intensity it is likely that the quenching H<sub>2</sub>O molecules are more tightly bound than the quenching H<sub>2</sub>O adsorbates. In addition, both types of adsorbates appear to compete for adsorption sites which is similar to the situation of NO<sub>2</sub> and O<sub>3</sub> competing with pre-adsorbed oxygen.



## 5 Analysis of the adsorption phenomena

In chapter 4 gas response data for major groups of analytes relevant to the field of gas sensors have been presented: air components, such as oxygen and water vapour, oxidizing air pollutants, such as  $\text{NO}_2$  and  $\text{O}_3$  and reducing gases, in particular alcohols and aliphatic hydrocarbons. Whereas chapter 4 has focused on presenting raw data, the present chapter turns to a more quantitative analysis of these data.

### 5.1 Concentration- and temperature dependence of the PL response

The PL data presented in the previous chapter revealed that the PL of the NWA transducers can be both enhanced and quenched, depending of the type of test gas. In the case of water vapour quenching and enhancing PL responses can be observed during a single exposure pulse. These three kinds of response are schematically illustrated in Figure 5.1 alongside with the way in which gas response data are extracted from such PL response transients. A quenching response is observed for oxidizing gases such as  $\text{O}_2$ ,  $\text{NO}_2$  and  $\text{O}_3$  (Figure 5.1 a), an enhancing response is observed for all kind of hydrocarbons (Figure 5.1 b) and both kinds of response are observed in the case of water vapour (Figure 5.1 c).

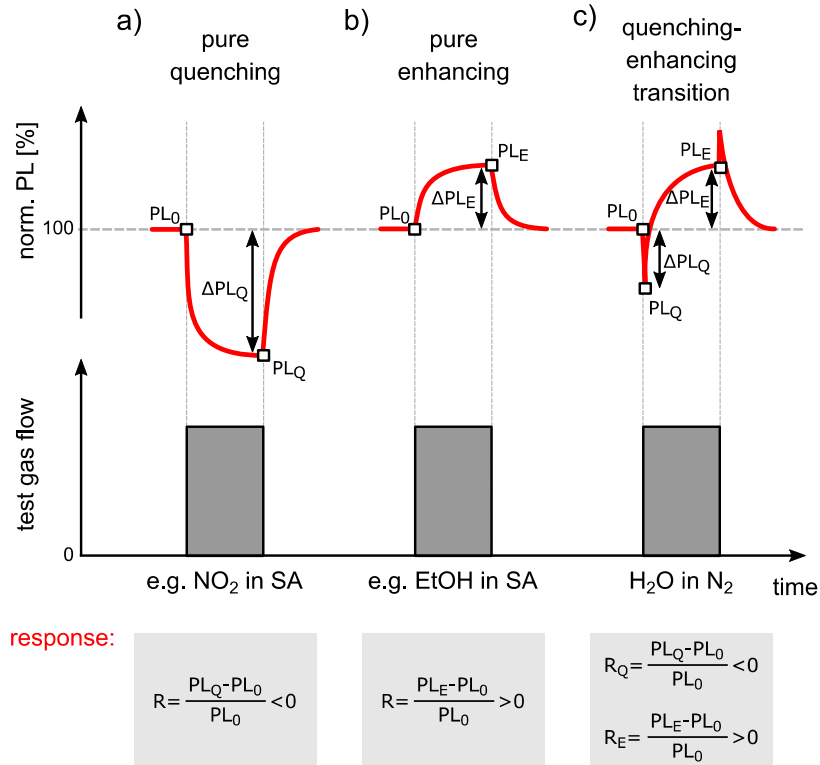


Figure 5.1. Extraction of gas response data from PL response transients of NWA transducers: a) pure quenching response, b) enhancing response, c) transition from quenching to enhancing response.

In Figure 5.2 response data are shown for O<sub>2</sub> and H<sub>2</sub>O diluted in N<sub>2</sub> and NO<sub>2</sub> and O<sub>3</sub> diluted in SA backgrounds. The data points in this graph were extracted from the raw data as explained in Figure 5.1 and, where available, mean values of repeated measurements were calculated. The data for water vapour were extracted from raw data acquired at high LED light intensities where reducing PL responses are largely negligible. Water-related quenching responses will be discussed later in this chapter. For reasons of data reduction all response curves in Figure 5.2 were fitted to Langmuir adsorption isotherms

$$R_{LAR,x}(p, T) = \theta_{Lang}(p, T) R_{max,x}(T). \quad (5.1)$$

with  $\theta_{Lang}(p, T)$  standing for the Langmuir adsorption isotherms and  $R_{max,x}$  for the saturated PL response of gas  $x$  in the limit of very large concentrations. In the follow-

ing we call this model LAR model because it involves **L**angmuir **a**dsorption and **r**e-combination processes of photogenerated charge carriers. The parameter  $R_{max,x}$  which mainly depend on the recombination processes, are explained in more detail in chapter 6 and 7. In this chapter the main focus is on the Langmuir isotherms and the LAR adsorption energies that can be extracted from such fits.

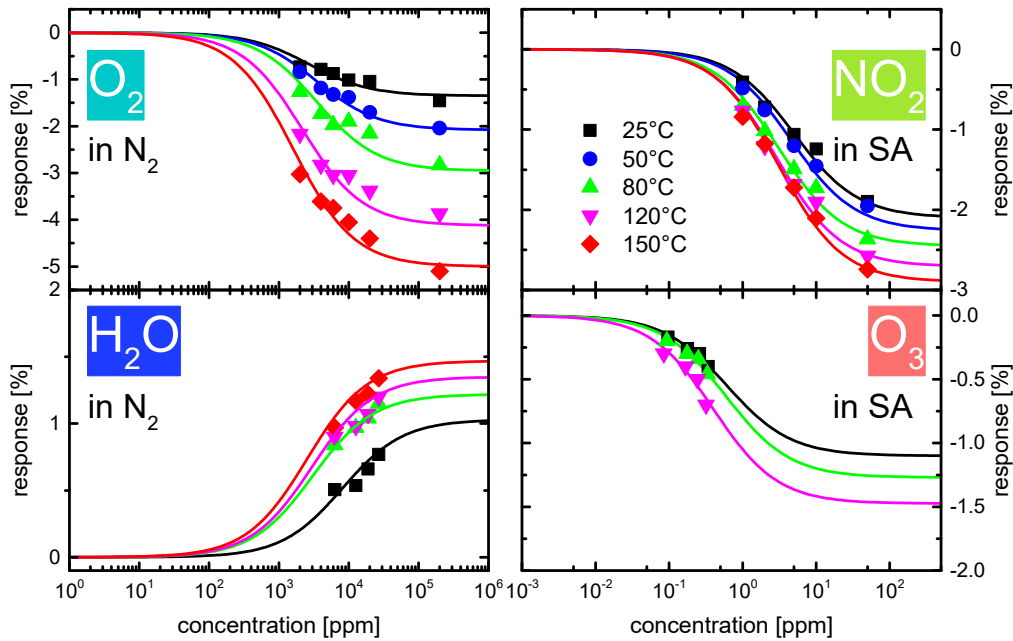


Figure 5.2. Overview of the gas response of the In/GaN NW transducer upon exposure to  $O_2$  and  $H_2O$  at nitrogen background and  $NO_2$  and  $O_3$  at synthetic air for temperatures between  $25^\circ C$  and  $150^\circ C$ .

Overall, Figure 5.2 shows that experimental PL response data can be well fitted with Langmuir adsorption isotherms. Turning to the individual gases in more detail, one can see that the data for  $O_2$  and  $NO_2$  are best fitted and that the acquired data more or less cover the most interesting concentration ranges. In the cases of  $H_2O$  and  $O_3$  relevant data is missing. In the case of  $H_2O$ , lower  $H_2O$  concentrations were difficult to produce as water bubblers require a minimum airflow to ensure stable operation conditions. Higher concentrations are physically impossible as these would correspond to more than 100 % saturation. In the case of ozone, higher concentrations would have been desirable. However, due to the chemical instability of ozone and instrumental limitations only concentrations below 1 ppm could be produced.

Among all gases investigated, the response to ethanol could be studied over the widest concentration range, as this substance could be provided both from pressurized gas cylinders as well as from vapour saturation bottles. The data points in Figure 5.3 (a) show the response data as plotted against the ethanol concentration for each value of transducer temperature. The full lines, on the other hand, show LAR fits, which were performed as described above or in ref. [76,101]. The calculated curves obviously reproduce the experimental data quite well - over a concentration range of no less than 5 orders of magnitude. The Langmuir adsorption energies determined from these fits are listed next to the individual curves. The saturated values of the PL response, observed in the limit of high ethanol concentrations, systematically increase as the transducer temperature is increased. The data in Figure 5.3 (b), on the other hand, show that the saturation response also depends on the LED light intensity. This light-intensity dependence, however, is much less pronounced than the temperature dependence.

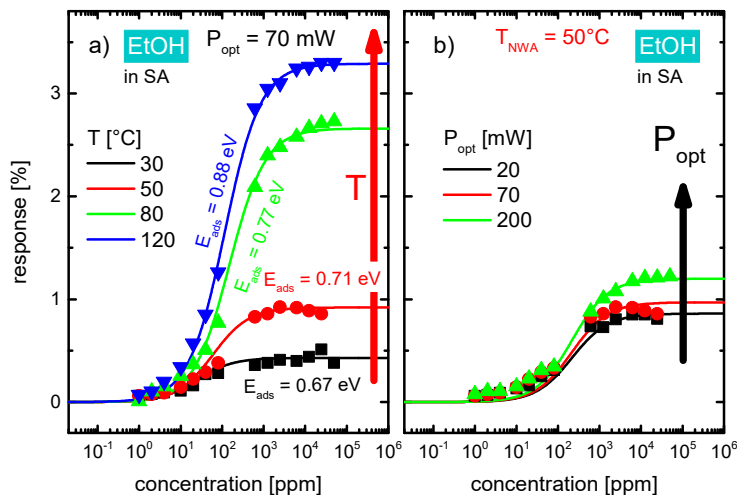


Figure 5.3. (a) Concentration and temperature dependence of the ethanol enhancement effect.  $E_{ads}$  values represent LAR adsorption energies; (b) dependence of the ethanol enhancement effect on PL excitation light intensity.

The maximum response parameter  $R_{max}$  increases approx. linearly with the transducer temperature as shown in Figure 5.4. The factors for ozone are more guesses than real extrapolations from experimental data as high concentration data were not accessible with the available experimental setup.

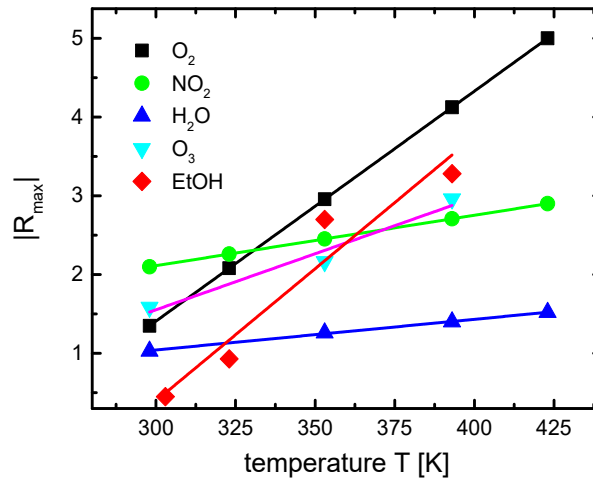


Figure 5.4. Temperature dependence of the maximum recombination parameter  $R_{max}$  as obtained from fitting equation 9.2 to the data of Figure 9.8.

Another important parameter that can be extracted from LAR fits is the half maximum concentration  $c_{1/2}$ . This parameter determines the concentration at which the gas response reaches 50% of its saturation value. The parameter  $c_{1/2}$  thus determines the position of the sensitivity window of a specific transducer for a given gas species. Mathematically  $c_{1/2}$  can be obtained by equating the LAR fit function (5.1) to one half of the maximum response:

$$R_{LAR,x}(c_{1/2}, T) = \frac{1}{2} R_{max,x}(T) \Rightarrow \theta_{Lang}(c_{1/2}, T) = \frac{1}{2}. \quad (5.2)$$

It is obvious that  $c_{1/2}$  becomes a function of the Langmuir adsorption energy. In Figure 5.5  $c_{1/2}$  is plotted against the adsorption energy. Molecules with similar masses lie on the same dotted lines. Slight variations of the adsorption energy have a huge impact on the half maximum concentration  $c_{1/2}$ , which can be seen from the inserted data points that were extracted from the LAR fits. The higher the adsorption energy  $E_{ads}$  the lower  $c_{1/2}$ , which means that LAR isotherms shift towards lower concentration ranges. Figure 5.5 shows that slightly higher adsorption energies result in exponentially increased gas sensitivities.

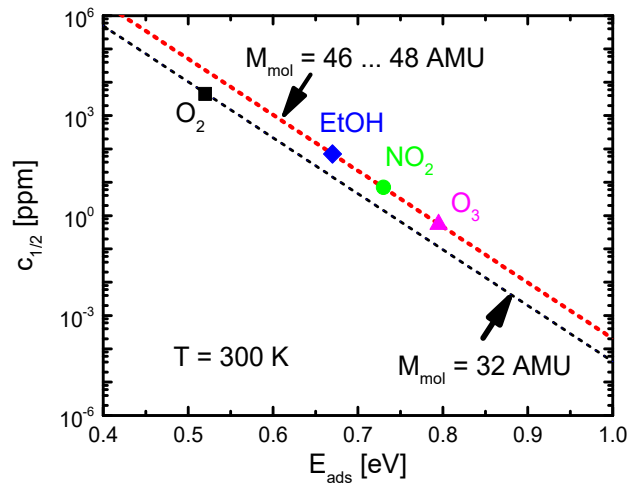


Figure 5.5. Concentration of half maximum response  $c_{1/2}$  with respect to the adsorption energy. The lines represent theoretical  $c_{1/2}$  values as a function of  $E_{ads}$  for different adsorbates with different molecular weight. The data points for  $O_2$ , EtOH,  $NO_2$  and  $O_3$  were extracted from LAR fits.

## 5.2 Competitive adsorption of air constituents on III-nitride surfaces

Focusing on the positions of the sensitivity windows in Figure 5.2 and Figure 5.3, it can be seen that increasing NWA temperatures mainly impact the magnitudes of the saturated responses,  $R_{max}$ , but hardly the positions of the sensitivity windows. The sensitivity window for each gas is more or less independent on temperature.

In order to emphasize the strong influence of the temperature on the Langmuir type adsorption, Figure 5.6 shows adsorption isotherms as calculated for a range of temperatures, assuming at the same time that the adsorption energy is a fixed, species-dependent constant. Within such a model, the calculated adsorption curves should continually shift towards higher concentrations as the transducer temperature is raised. Concentrating on  $O_2$  and comparing the experimental data to this expected theoretical behaviour, a huge discrepancy is observed: all experimental data scatter around a single Langmuir isotherm, independent of the transducer temperatures at which the respective data had been collected.

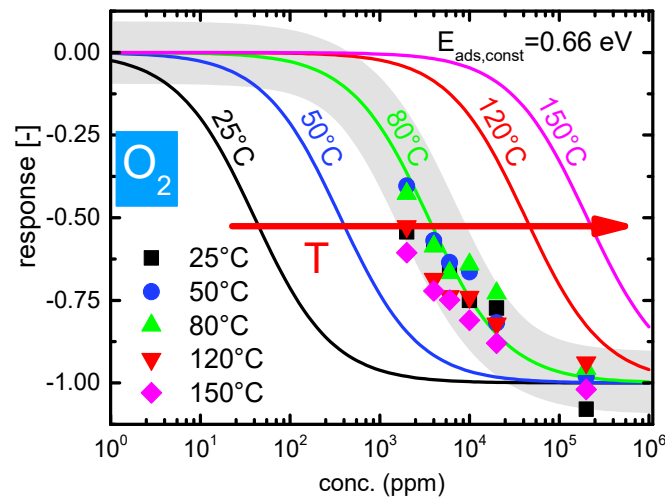


Figure 5.6. Comparison of normalized PL response data for  $O_2$  versus predictions based on Langmuir isotherms with a constant and species-specific value of  $E_{ads}$  (here 0.66 eV). Whereas all experimental response data more or less fall on top of each other, irrespective of the temperature at which these had been gathered, theory predicts a huge shift of the sensitivity windows with temperature.

Mathematically, this discrepancy can be resolved by assuming that the adsorption energy is not a species-dependent constant but rather temperature-dependent. This, however is in contrast to the generally accepted textbook-versions of the Langmuir adsorption theory which assume exposure to a single gas and a constant, gas-specific adsorption energy [64]. Allowing fits with temperature-dependent adsorption energies, the fitted  $E_{ads}(T)$  values vary linearly with the transducer temperature as shown in Figure 5.7. The dotted lines in this graph indicate extrapolations of the individual data sets towards cryogenic temperatures. A straight forward interpretation of this data would mean that at very low temperatures the adsorbates physisorb with very low binding energies and that physisorbed species re-arrange bonds and relax into increasingly tighter-bound chemisorption states as more and more thermal energy becomes available. Another approach at explaining the linear increase in adsorption energies with temperature is involving a process of competitive adsorption. This approach has been published in [101].

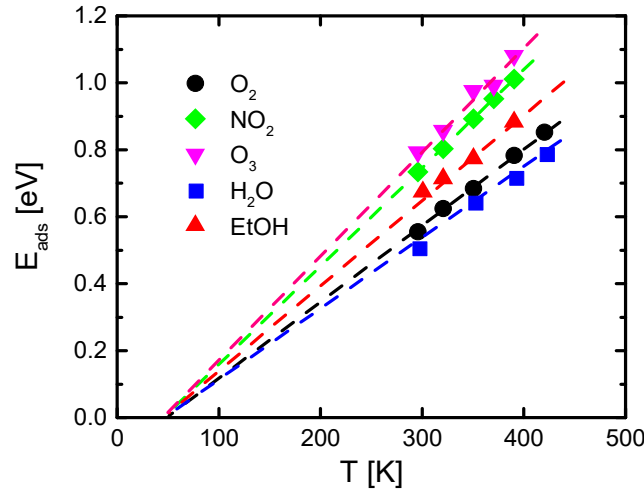


Figure 5.7.  $E_{\text{ads}}$  as a function of the adsorbent temperature  $T$ . The data points were evaluated from the PL response data of Figure 9.8. Broken lines are linear extrapolations towards cryogenic temperatures.

### 5.2.1 Two component Langmuir adsorption on III-nitride surfaces

In all measurements that were carried out in this thesis at least two different components are present in the test gas. As a consequence, a modified adsorption model based on competitive adsorption is introduced.

As derived in chapter 2, in the case of simple Langmuir adsorption, the surface coverage  $\theta_{A,SL}$  for a single gas species  $A$  depends only on the partial pressure  $p_A$  of this gas and on the temperature  $T$  of the adsorbent:

$$\theta_{A,SL}(p_A, T) = \frac{p_A}{p_A + P_{00A}(T) \exp\left[-\frac{E_A}{k_B T}\right]} \quad (5.3)$$

The only parameter in this equation is the adsorption energy  $E_A$  which is a characteristic measure for the bond strength between adsorbate and adsorbent.

When considering a second adsorption process of a gas species  $B$  which takes place in parallel to species  $A$  and in which the adsorbates compete for adsorption sites, the surface coverages for  $A$  and  $B$  become (see chapter 2):

$$\theta_A(p_A, p_B, T) = \frac{p_A}{p_A + P_{00A}(T) \exp\left[-\frac{E_A}{k_B T}\right] \left[1 + \frac{p_B}{P_{00B}(T)} \exp\left(\frac{E_B}{k_B T}\right)\right]} \quad (5.4)$$

$$\theta_B(p_A, p_B, T) = \frac{p_B}{p_B + P_{00B}(T) \exp\left[-\frac{E_B}{k_B T}\right] \left[1 + \frac{p_A}{P_{00A}(T)} \exp\left(\frac{E_A}{k_B T}\right)\right]} \quad (5.5)$$

The above equations show two adsorption isotherms similar to equation 5.3, except for the bracketed terms on the far right-hand side of each denominator. These latter terms depend on both partial pressures and therefore describe the competition of A and B for adsorption sites. Introducing an effective adsorption energy by

$$E_{eff,A}(p_B, T) = -k_B T \ln \left[ \exp\left(-\frac{E_A}{k_B T}\right) \left[1 + \frac{p_B}{P_{00B}(T)} \exp\left(\frac{E_B}{k_B T}\right)\right] \right], \quad (5.6)$$

the adsorption isotherm for gas species A reduces to the familiar Langmuir form:

$$\theta_A(p_A, p_B, T) = \frac{p_A}{p_A + P_{00A}(T) \exp\left[-\frac{E_{eff,A}(p_B, T)}{k_B T}\right]} \quad (5.7)$$

In this latter form, all the competition between gas species A and B is absorbed in the effective adsorption energy  $E_{eff,A}(p_B, T)$ . This equation shows that the competition of adsorbate species A with species B lowers its effective adsorption energy below its single-component Langmuir value  $E_A$ . Concomitantly the surface coverage  $\theta_A(p_A, p_B, T)$  also drops below its corresponding single-component coverage  $\theta_A(p_A, T)$ . The same considerations also apply for gas species B as A also competes for adsorption sites with B.

In Figure 5.8 response data of an optimised InGaN/GaN nanowire sample with a pronounced gas sensitivity towards  $O_2$  is shown. Additionally calculated coverage values for  $N_2$  and  $O_2$  using equations (5.4) and (5.5) are plotted with  $E_{O_2} = 0.95$  eV and  $E_{N_2} = 0.75$  eV representing the adsorption energies for gas species A and B, where A stands for oxygen and B for nitrogen respectively. The square points are experimental data which fairly well approximate the mathematical model. The total coverage is indicated by the red line and is approx. one over the whole concentration range. In the low  $O_2$  concentration range the InGaN/GaN surface is almost completely covered by nitrogen. At higher  $O_2$  concentrations the nitrogen molecules are partially replaced by

oxygen. At approx. 3000 ppm  $O_2$  nitrogen and oxygen are present in equal concentrations at the InGaN/GaN surface. At higher concentrations the  $O_2$  molecules completely replace the  $N_2$  ones at the surface.

The experimental data provide PL response data and do not give direct information about the surface coverage. In this model it is assumed that  $O_2$  molecules act as surface recombination centres for photogenerated electron hole pairs whereas nitrogen ones do not influence the PL yield directly. This assumption seems plausible as nitrogen is inert in most chemical reactions.

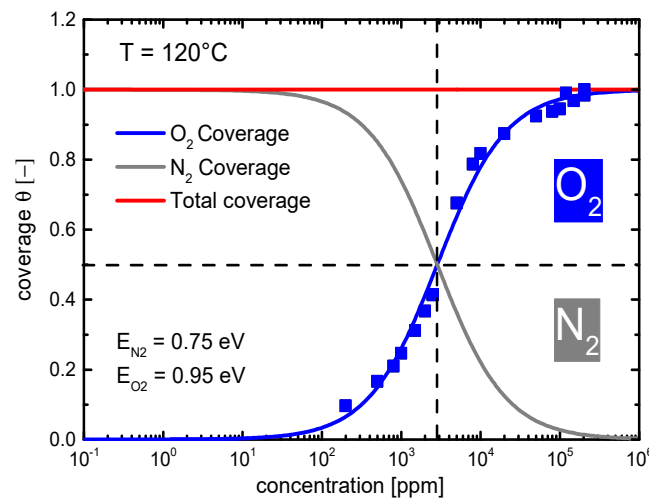


Figure 5.8. Calculated surface coverage of oxygen and nitrogen as the  $O_2$  concentration is raised. Measurement data of InGaN/GaN PL response measurements at  $120^\circ\text{C}$  are represented by square points and show good agreement with the theoretical curves.

Besides fitting the Langmuir shaped PL response curve in Figure 5.8 the model of competitive adsorption can explain the temperature-dependent adsorption energy as shown in Figure 5.9. Again, oxygen response data are used as an illustrative example and the effective adsorption energy according to equation is plotted against the transducer temperature. Using the same quantum chemical adsorption energies for oxygen and nitrogen (with  $E_{O_2} = 0.95$  eV and  $E_{N_2} = 0.75$  eV) as used in the fit of Figure 5.8, the adsorption energies extracted from the LAR fits of the previous section can be approximated. The calculated temperature dependence of the effective adsorption energy consists of a linearly increasing part and a saturation region. The curve is principally determined by two parameters: the difference of the adsorption energies of

the two components and the absolute adsorption energy of the species of interest (here  $O_2$ ).

In this figure the effective adsorption energy for nitrogen is illustrated, too. As nitrogen's direct influence on the PL yield is neglected, this information cannot be directly supported by experimental data. The dashed lines in Figure 5.8 show the effective adsorption energies for a different set of quantum chemical adsorption energies for  $O_2$  and  $N_2$  ( $E_{O_2} = 1.45$  eV and  $E_{N_2} = 1.25$  eV). The dashed lines overlap with their solid counterparts in the linear range. However, the effective adsorption energy saturates at higher temperatures. The steepness of the curve is represented by the energy difference of  $E_{O_2}$  and  $E_{N_2}$ . Their saturation values are determined by their absolute values.

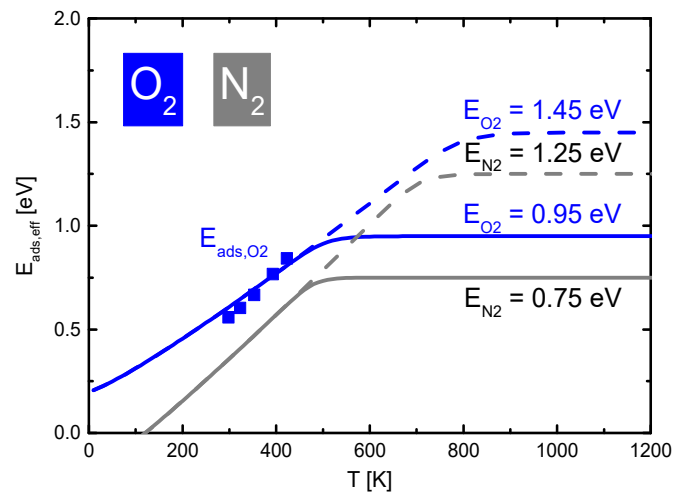


Figure 5.9. Effective adsorption energies  $E_{ads,eff}(T)$  with respect to temperatures for a competition between oxygen and nitrogen. The thick line represent  $E_{ads,eff,O_2}(T)$  and the thin lines  $E_{ads,eff,N_2}(T)$ . The dashed lines were obtained by using a higher set of quantum-chemical binding energies. Data points of  $E_{ads}(T)$  for  $O_2$  are taken from Figure 5.7.

A similar analysis can be carried out using PL data of  $H_2O$ ,  $NO_2$  and  $O_3$ . Using the same set of quantum-chemical binding energies and assuming two component competitive adsorption, one is able to simulate the linear increase of the adsorption energy. The adsorption energies and the effective adsorption energy curves are shown in Figure 5.10 (a). The saturation values of the effective adsorption is plotted in Figure 5.10 (b)

which shows an almost linear relationship with their corresponding electron affinities.

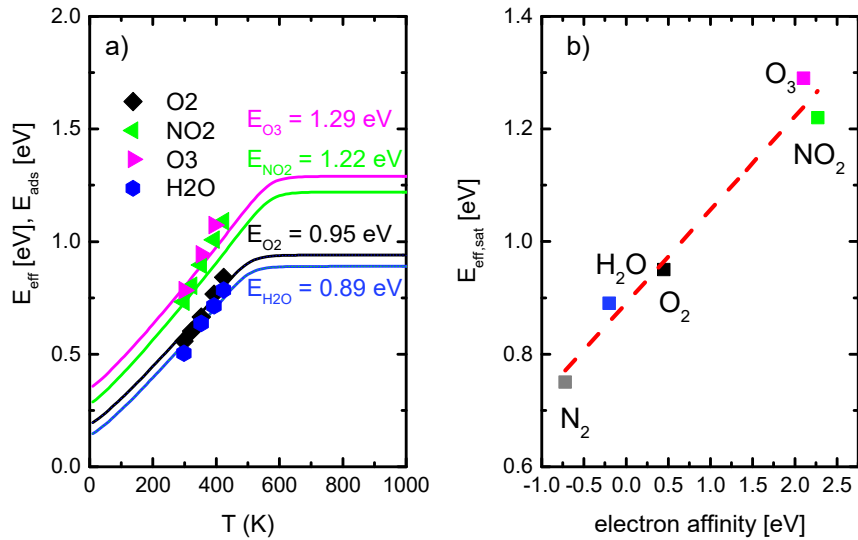


Figure 5.10. a) Variation of the effective adsorption energies of the investigated air constituents. Data points of  $E_{\text{ads}}(T)$  are taken from LAR fits. b) Saturated values of the effective adsorption energies as a function of the electron affinity of the air constituents.

In Figure 5.11 the PL response data are fitted using the LAR model where an effective adsorption energy has been introduced. The O<sub>2</sub> and H<sub>2</sub>O response data can be simulated using the model. The simulated curves seem less accurate as the original LAR fitted curves allowing arbitrary adsorption energies for each temperature. However the model of competitive adsorption helps to reduce the amount of free parameters to only one adsorption energy for each species, valid for all temperatures.

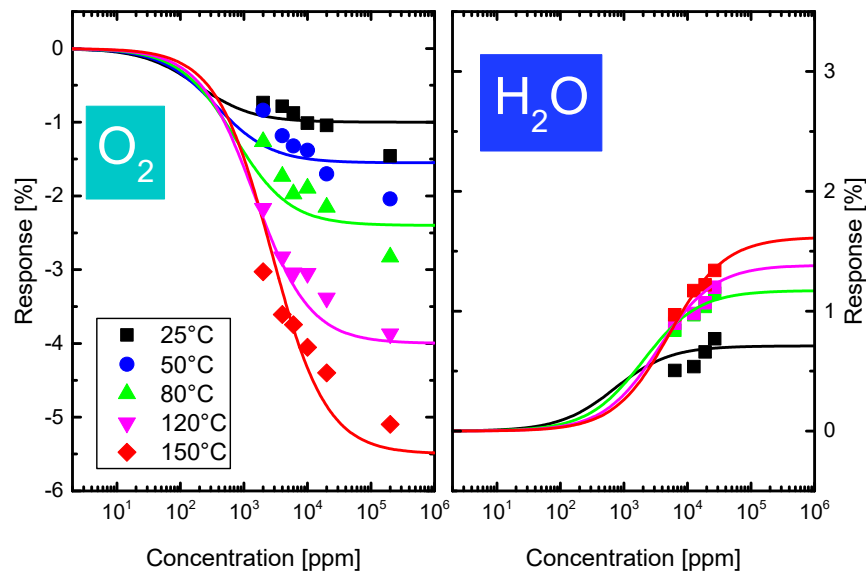


Figure 5.11. Experimental PL response data with the experimental data fitted to the competitive adsorption model.

### 5.3 Complex H<sub>2</sub>O adsorption

The experiments presented in the chapter 4 before show how water influences the PL response of InGaN/GaN nanowires. The PL response depends on the environmental conditions and can change from a quenching to an enhancing behaviour. Conditions where H<sub>2</sub>O acts as a PL quencher are low humidity, low light intensity and low temperature. Conditions that promote an enhancing effect on the InGaN/GaN nanowires are high humidity, higher light intensity and higher temperature. Table 5.1 lists these conditions together with possible hints with regard to the underlying molecular processes at the NWA surfaces. A detailed molecular picture will be given later after introducing the numerical model for simulating the PL response data.

Table 5.1. (left column) Experimental conditions under which adsorbed H<sub>2</sub>O molecules act as luminescence quenchers or luminescence enhancers; (right column) possible clues to the adsorbate forms and their associated formation processes.

H <sub>2</sub> O as a PL quencher	
<b>Low humidity</b>	Single (isolated) H <sub>2</sub> O adsorbates
<b>Low light intensity</b>	Photogenerated electrons and holes not involved in adsorbate formation
<b>Low temperature</b>	No re-arrangement of chemical bonds during adsorbate formation
H <sub>2</sub> O as a PL enhancer	
<b>High humidity</b>	Multi-molecular, more complex adsorbates
<b>High light intensity</b>	Photogenerated electrons and holes involved in adsorbate formation
<b>High temperature</b>	Re-arrangement of chemical bonds during passivating adsorbate formation

### 5.3.1 Competitive water adsorption model

The above data suggest that adsorbed water vapour can play a double role in the PL response of InGaN/GaN nanowire arrays. In this section a rate equation model is introduced where water adsorbates can form either quenching (Q) or enhancing (E) species. In this model it is assumed that both kinds of adsorbates compete for a limited number of adsorption sites according to a competitive adsorption model (see chapter 2). The combination of a competitive adsorption model and the two-fold role of water vapour, simultaneously being a PL-quencher or a PL-enhancer, can be seen as a measurement with two gas species: PL-quenching H<sub>2</sub>O<sub>Q</sub> and PL-enhancing H<sub>2</sub>O<sub>E</sub>. The governing rate equations for the surface coverage  $\theta_Q$  for quenching H<sub>2</sub>O and  $\theta_E$  for enhancing H<sub>2</sub>O are:

$$\frac{d\theta_Q}{dt} = r_{ads,Q}(p_{H_2O}, T) (1 - \theta_Q(t) - \theta_E(t)) - r_{des,Q}(T) \theta_Q(t) \quad (5.8)$$

and

$$\frac{d\theta_E}{dt} = r_{ads,E}(p_{H_2O}, T, P_{opt}) (1 - \theta_Q(t) - \theta_E(t)) - r_{des,E}(T) \theta_E(t). \quad (5.9)$$

The rate parameters in the above equations account for the observed behaviour.

$$r_{ads,Q}(p_{H_2O}, T) = s_Q r_{H_2O}(p_{H_2O}, T) \exp\left(-\frac{E_{ads,Q}}{k_B T}\right). \quad (5.10)$$

$$r_{des,Q}(T) = r_{0,Q} \exp\left(-\frac{E_{des,Q}}{k_B T}\right). \quad (5.11)$$

$$r_{ads,E}(p_{H_2O}, T, P_{opt}) = s_E r_{H_2O}(p_{H_2O}, T) \left(\frac{P_{opt}}{P_{opt,max}}\right)^\gamma \exp\left(-\frac{E_{ads,E}}{k_B T}\right). \quad (5.12)$$

$$r_{des,E}(T) = r_{0,E} \exp\left(-\frac{E_{des,E}}{k_B T}\right). \quad (5.13)$$

The rate parameter  $r_{H_2O}(p_{H_2O}, T)$  denotes the gas-kinetic collisions rate of water molecules on the adsorbent surface and can be expressed as

$$r_{H_2O}(p_{H_2O}, T) = \frac{p_{H_2O}}{\sqrt{2\pi M_{H_2O} k_B T}} A_{ads}. \quad (5.14)$$

Here, the impact rate per adsorption site depends on the partial pressure  $p_{H_2O}$ , the molecular mass  $M_{H_2O}$  and the size of the H<sub>2</sub>O-adsorption sites  $A_{ads}$ .

Furthermore Boltzmann terms with activation energies  $E_{ads,Q}$ ,  $E_{ads,E}$  for adsorption in equations (5.10) and (5.12) and  $E_{des,Q}$ ,  $E_{des,E}$  for desorption in the equations (5.11) and (5.13) are introduced along with corresponding rate pre-factors. Additionally, the adsorption terms for the quenching and enhancing species contain a sticking coefficient  $s_Q$  and  $s_E$  that represents the probability of an impacting H<sub>2</sub>O molecule of actually staying on the surface. In order to account for the influence of UV light on the formation of enhancing H<sub>2</sub>O adsorbates, a normalized optical power factor  $\frac{P_{opt}}{P_{opt,max}}$  with

an exponential factor  $\gamma$  is inserted in the adsorption rate term for enhancing water adsorbates in equation (5.12).

### 5.3.2 Data fitting

The competitive adsorption model for quenching and enhancing type water molecules can be used to simulate the gas response transients and compare it to the experimental data. The response value is a linear combination of the occupation number of both adsorbates:

$$R_{H_2O,sim} = \alpha_Q \theta_Q + \alpha_E \theta_Q \quad (5.15)$$

The prefactors have opposite signs and  $\alpha_Q < 0$  and  $\alpha_E > 0$  and thus enable a transition from quenching to an enhancing PL response during water exposure. With this model the experimental data can be reproduced mathematically using the parameters listed in Table 5.2.

Table 5.2. Model parameters yielding the PL response data displayed in the right-hand column of Figure 5.12.

Parameter	value
$s_Q$	$3.5 \cdot 10^{-2}$
$E_{ads,Q}$	$\sim 0$ eV
$r_{0,Q}$	$10 \frac{1}{s}$
$E_{des,Q}$	$\sim 0$ eV
$s_E$	$2.4 \cdot 10^{-6}$
$\gamma$	0.5
$E_{ads,E}$	0.4 eV
$r_{0,E}$	$5 \cdot 10^{-2} \frac{1}{s}$
$E_{des,E}$	$\sim 0$ eV

The parameters in Table 5.2 were obtained in an iterative way by fitting a simulated gas response transient to the measurement data. The differential equations (5.9) and (5.10) for the occupancy of quenching and enhancing type H<sub>2</sub>O were solved using Mathematica's nonlinear differential equation solver with standard configuration. The water vapour exposure pulses were modelled by a function  $p_{H_2O}(t)$  consisting of an array of idealized box-like exposure pulses. In reality a smoother curve is expected. The results for the occupancies  $\theta_Q(t)$  and  $\theta_E(t)$  were inserted in equation (5.15) for the calculation of the theoretical gas response. Appropriate values for  $\alpha_Q$  and  $\alpha_E$  were chosen to match the experimental PL response transients. The simulation results with the best suited parameter set and a comparison with the experimental data are shown in Figure 5.12 with the left-hand side showing the experimental data and the right-hand side the simulated response functions. The calculated data show a fairly good agreement with the experimental data. In particular these data mimic the typical characteristics of the transition from quenching to enhancing behaviour.

More details on the molecular mechanism of the applied model will be given in chapter 6.

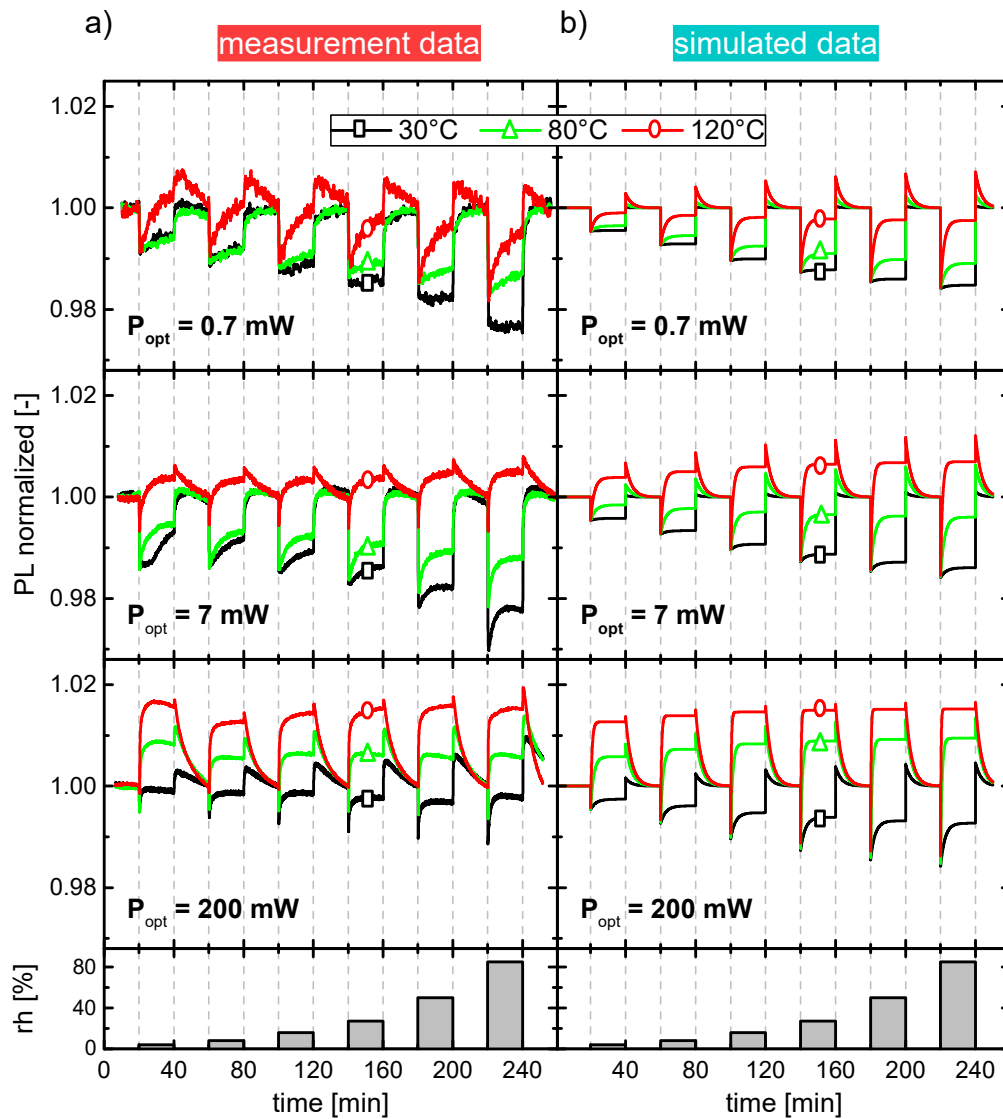
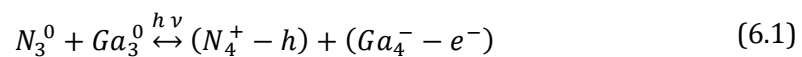


Figure 5.12. Experimental data (a) and simulated data (b) of PL response measurements towards  $\text{H}_2\text{O}$  under different experimental conditions. The plots from top to bottom show PL transients for three transducer temperatures at increasingly higher excitation light energies. The bottom graph shows the humidity profile. The simulations were carried out with the parameters listed in Table 5.2

## 6 Molecular mechanism of adsorption

### 6.1 Recombination and adsorption at non-polar III-nitride surfaces

The adsorption process at InGaN/GaN surfaces depends on the bonding configurations at the semiconductor surface. As stated in the chapter 2 the bulk InGaN/GaN material has a tetrahedral coordination which is achieved by an electron transfer from N towards Ga and In atoms. In the notation of the so-called 8-N rule [102,103], these states are denoted by  $N_4^+$ ,  $Ga_4^-$  and  $In_4^-$ . The superscript (+/-) denotes the ionic charge of the atom and the subscript denotes the number of bonds that are needed to form completely filled or empty valence shells. Due to a lack of bond partners, the InGaN/GaN constituents are not able to form 4 bonds at the surface. This results either in a high dangling bond concentration or in reconstructed surfaces with three-fold bonded N-Ga(In) sites. In this three-fold bond configuration the lattice constituents can be denoted as  $N_3^0$ ,  $Ga_3^0$  and  $In_3^0$ . The latter uncharged, reconstructed situation of a neighbouring N-Ga pair at a non-polar  $(\bar{1}\bar{1}00)$  nanowire lateral surface is shown in Figure 6.1 (a). With N being a potential electron donor and Ga an electron acceptor, the N-Ga pair can be considered as a Lewis acid/base site pair. Upon photoexcitation ( $h\nu$ ) such pairs can trap electron-hole pairs as shown in Figure 6.1 (b) forming  $N_4^+$  and  $Ga_4^-$  (or  $In_4^-$ , respectively):



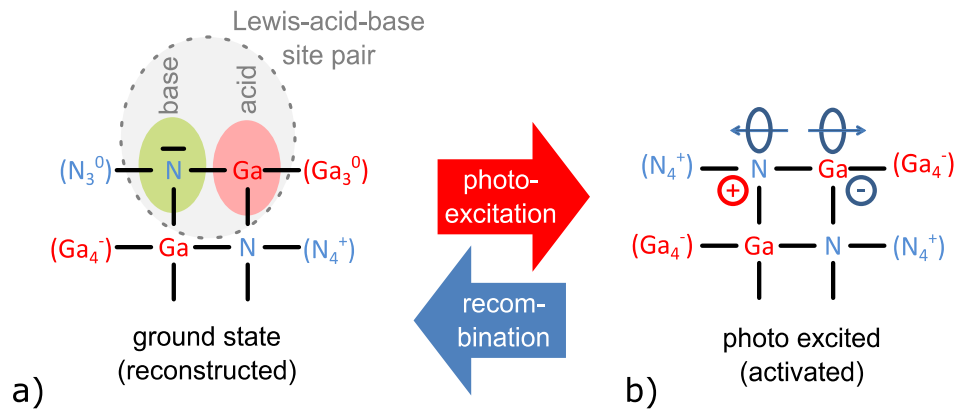
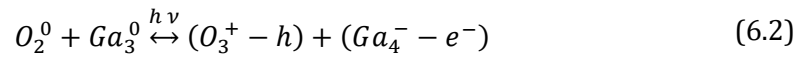


Figure 6.1. (a) Tetrahedral bulk bonding and re-constructed surface bonding at lateral  $(1\bar{1}00)$  surfaces of III-nitride nanowires. The colouring indicates formation of Lewis acid-base pairs; (b) photo-activated state of a III-nitride surface following photo-generation in the bulk. The circles with plus and minus signs denote a photogenerated electron-hole pair.

InGaN/GaN surfaces exposed to ambient air are likely to form some native oxide on the surface [27]. At this point it is relevant to note that Lewis acid-base pairs can also form on oxidized surfaces. The corresponding transformations between oxide states are shown in Figure 6.1 (c) and (d) and can be expressed in 8-N terms as:



Similar to non-oxidized surfaces, neighbouring oxygen and gallium atoms on oxidized surfaces can interchange between the ground states of reconstructed Lewis acid-base pairs and photo excited states with two dangling bond radicals as depicted in Figure 6.2.

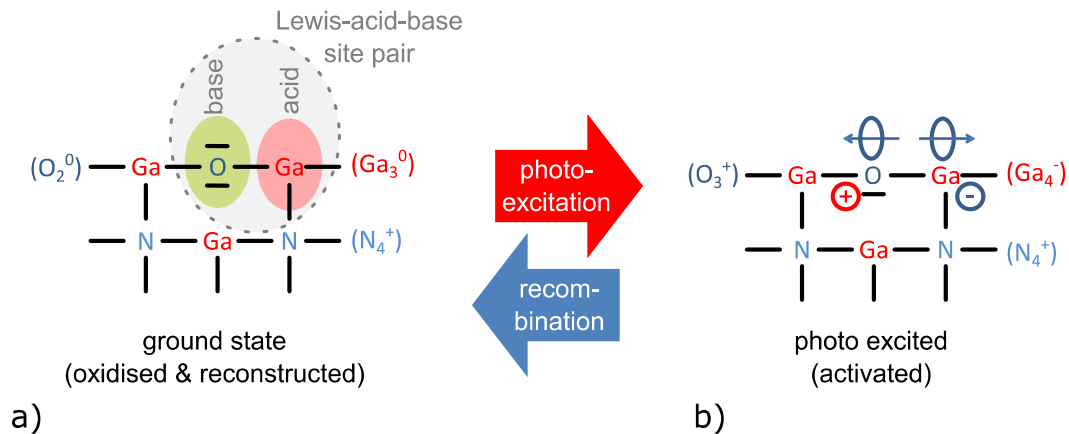


Figure 6.2. (a) Lewis acid base pair formed by Ga and an embedded oxygen at lateral ( $1\bar{1}00$ ) surfaces of III-nitride nanowires. (b) photo-activated state of an oxidised III-nitride surface after photo-excitation.

The transition from a photo-excited state back to the ground state, as indicated in Figure 6.1 and Figure 6.2 or in equations (6.1) and (6.2), is reversible. A contribution to the PL is expected when the transition is accompanied by the emission of a photon.

Adsorption processes on N-Ga pairs can take place both in their ground and excited states. Depending on their excitation state, adsorbate-specific chemical bonding processes are possible. In Figure 6.3 adsorption processes involving the previously discussed adsorbates are illustrated. In Figure 6.3 (a) the ground state is shown. Upon exposure to N<sub>2</sub>, Ga can bond to the lone pair electrons of the N<sub>2</sub> molecule which is shown in Figure 6.3 (b). In the next Figure 6.3 (c) the interaction of water molecules with the Ga-N sites is shown. Due to auto-protolysis of water, forming protons and hydroxyl ions, water can passivate the N-Ga sites. A detailed discussion will be given in the next chapter. The chemisorption processes for O<sub>2</sub>, NO<sub>2</sub> and O<sub>3</sub> is illustrated in Figure 6.3 (d) - (e). They require the trapping of electrons from the InGaN conduction band onto these high-electron affinity adsorbates (electron affinities:  $E_{A,O_2} = 0.488\text{eV}$ ,  $E_{A,NO_2} = 2.173\text{eV}$ ,  $E_{A,O_3} = 2.103\text{eV}$ ) [104,105].

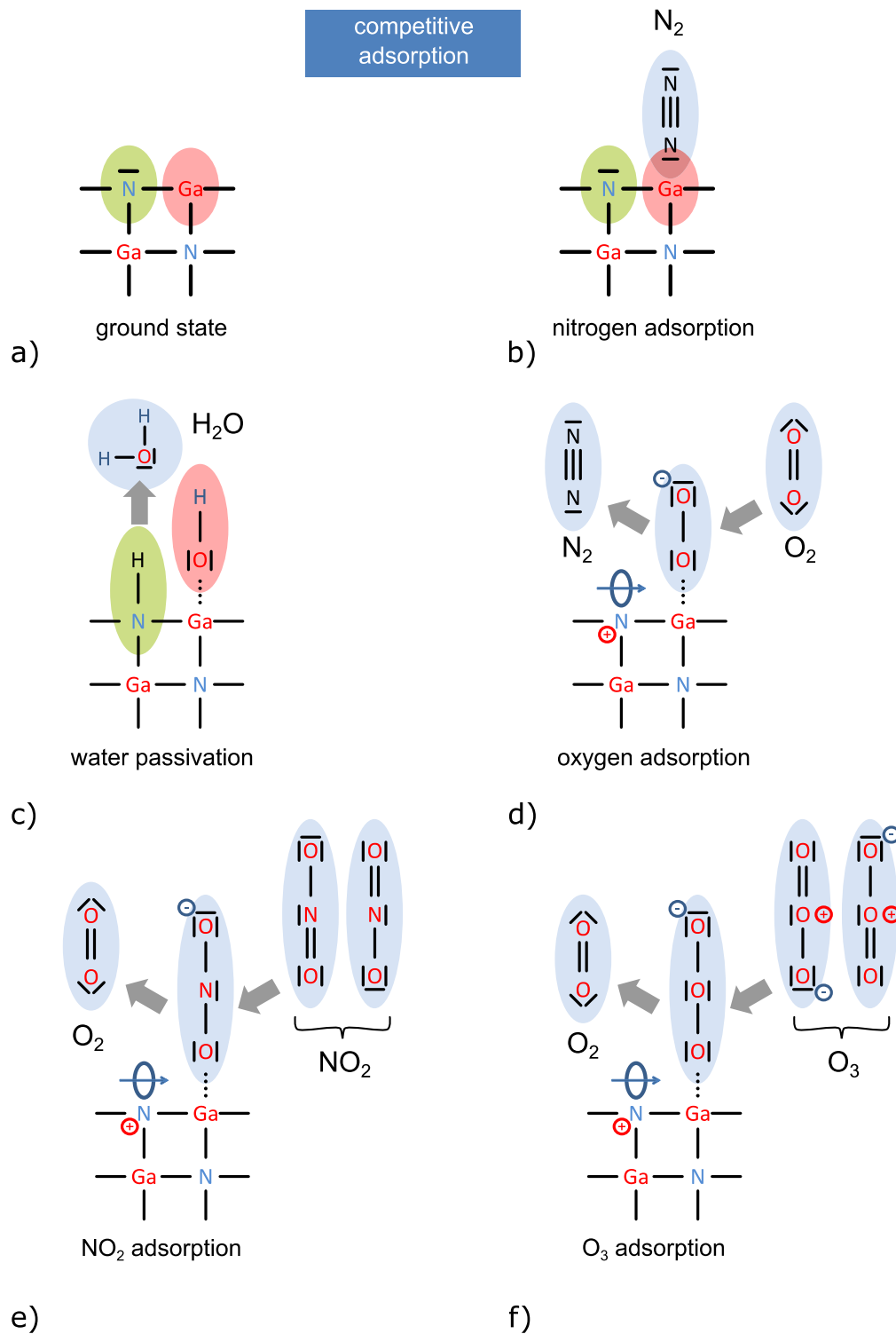


Figure 6.3. Adsorption at non-polar III-nitride surfaces: (a) ground state forms a Lewis-acid-base site pair (b)  $\text{N}_2$ -physisorption (c) water passivation (c) oxygen adsorption replacing  $\text{N}_2$  (e)  $\text{NO}_2$  adsorption replacing  $\text{O}_2$  f)  $\text{O}_3$  adsorption replacing  $\text{O}_2$

## 6.2 Water adsorption at III-nitride surfaces

Similar to the molecular interpretation of the competitive adsorption processes of oxidising air contaminants, H<sub>2</sub>O adsorption explanations will be given exemplarily for GaN surfaces. However these explanations remain principally valid when replacing Ga with In and even N with surface oxygen and for details on an oxidised InGaN/GaN the reader is referred to the last section about competitive adsorption. The situation of the interaction with water starts from the same assumptions. The key element in the proposed molecular model for the water adsorption process is the transition of a neighbouring Ga-N pair from a reconstructed ground state into a photo-activated state. Both states of the surface featuring tetrahedral bulk bonding are schematically visualized for a non-polar ( $\bar{1}\bar{1}00$ ) nanowire lateral surface in Figure 6.1 or in the case for an oxidized surface in Figure 6.2.

The GaN nanowire can have a reconstructed surface in the ground state where Ga and N (In) have three bonds to neighbours in the bulk of the nanowire. Surface N atoms have excess electrons whereas In/Ga exhibit electron deficiencies making neighbouring Ga(In)-N partners Lewis-acid-base-pairs (see Figure 6.1 (a)). Upon photoexcitation this pair can trap an electron-hole pair, thus forming a pair of dangling bonds at the surface as depicted in Figure 6.1 (b).

A high dangling bond concentration makes chemical interactions with adsorbates more likely. In the case of water a possible scenario is shown in Figure 6.4. Here a physisorbed water molecule can transfer one electron from its lone-pair orbitals to the  $N_4^+$  surface atom and subsequently extract an electron from a neighbouring  $Ga_4^-$  or  $In_4^-$  atom. In this way a photo generated electron hole pair has non-radiatively recombined yielding a reduced PL.

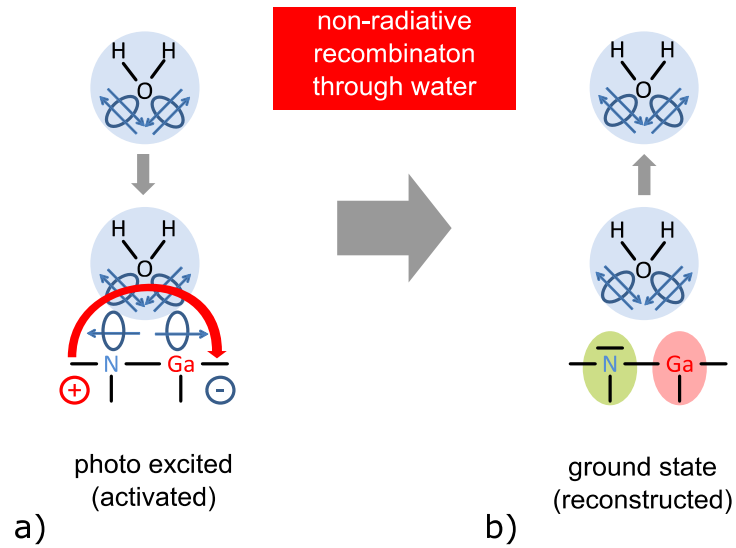


Figure 6.4. (a) Adsorption of a  $\text{H}_2\text{O}$  molecule on a photo-activated Lewis acid-base surface site. The red arrow indicates the transfer of a photogenerated hole within a photo-activated Lewis acid-base pair across the lone pair orbitals of an adsorbed  $\text{H}_2\text{O}$  molecule; (b) state after electron-hole recombination and surface reconstruction.

As experimental data show,  $\text{H}_2\text{O}$  also promotes PL enhancement especially under higher-temperature- and higher light-intensity conditions. In Figure 6.5 a sequence of steps is illustrated where adsorbing water molecules dissociate passivate surface recombination centres.

UV light is able to photo-electrochemically dissociate water into reactive intermediate ions ( $\text{H}^+$  and  $\text{OH}^-$  ions) [106,107]. Due to the fact that the position of the band edges of InGaN fit to the respective redox levels of water [107,108] a charge transfer between ions and photo-activated InGaN surfaces is promoted. This results in N-H and Ga(In)-OH passivated surfaces as shown in Figure 6.5 (b). In this situation trapping additional photogenerated electron-hole pairs on the surface is prevented and the non-radiative recombination channel over such surface sites is blocked. An enhanced PL is therefore expected.

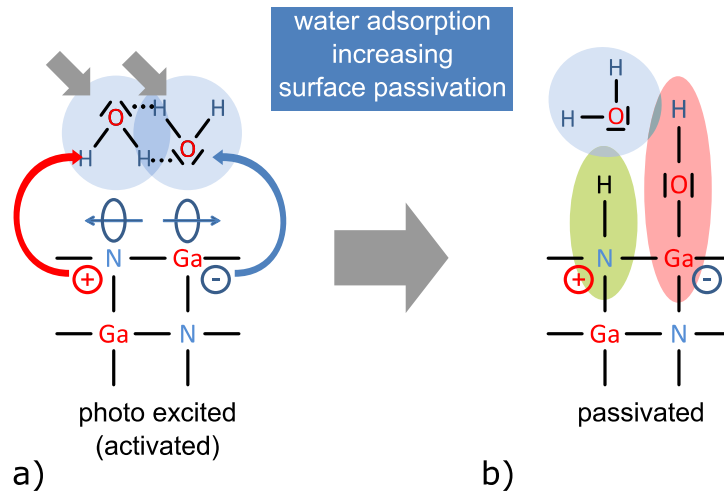


Figure 6.5. (a) Water adsorption on a photo-activated N-Ga (In-Ga) site pair. (b) The passivated state (N-H and Ga(In)-OH) disables surface recombination of photogenerated electron hole pairs which leads to an increased PL yield.

Figure 6.6 (a,b) show the reverse process of desorbing water from the surface and reducing the surface termination, thus promoting surface recombination and PL quenching. In this process the bonded  $\text{H}^+$  and  $\text{OH}^-$  radicals can recombine by inserting an electron-hole pair to the conduction band. The radicals can re-form a water molecule and desorb from the surface leaving a reconstructed surface behind. The re-injection of the formerly bound electron-hole pair increases the concentration of electron-hole pairs in the bulk, thus enhancing the PL yield for a short period of time. On a longer time scale, however, the PL is expected to be quenched as the surface atoms are now free again for supporting non-radiative recombination processes. This is in agreement with experimental data that shows that two counteracting processes are operative after switching from wet to dry background gas, a fast enhancing and a slow quenching transient.

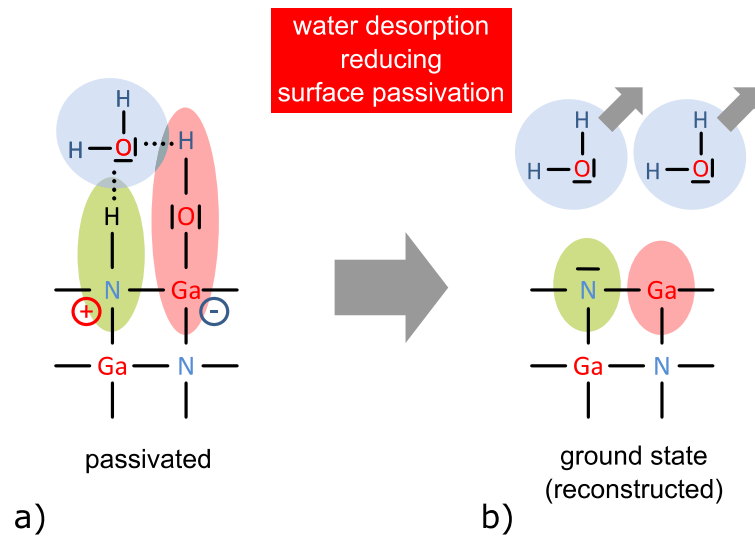


Figure 6.6. (a) shows the water passivated surface state limiting surface recombination. (b) N-H and Ga(In)-OH complex can convert back to water and desorb from the Ga(In)N surface. In the ground state the surface states can act as recombination centres reducing the overall PL response.

The process described above constitutes a reversible photo-electrochemical oxidation process of the InGaN/GaN surface. As water splits into protons and hydroxyl ions the oxidation in this case is caused by  $\text{OH}^-$  ions forming Ga-OH as oxidized species.

As indicated in Figure 6.5, one  $\text{H}_2\text{O}$  molecule is consumed in the passivation process. The second molecule is able to interact with polar H- and OH-groups. A possible scenario could be that the passivation layer acts as a starting layer for further adsorptions on top. This is the so-called Brunauer-Emmet-Teller (BET) adsorption [66] which may build up multi-layer water adsorbates. In this latter state unconsumed  $\text{H}_2\text{O}$  molecules may form the starting layer of a possible multi-layer BET adsorbate [66]. A limiting form of such a BET adsorbate is a macroscopic volume of water in contact with a “wet” oxidized III-nitride surface. Depending on the pH value of the liquid electrolyte, either  $\text{H}_3\text{O}^+$  or  $\text{OH}^-$  ions are available which may exchange protons with the surface Ga(In) OH groups, thus transforming them into  $\text{Ga} - \text{OH}_2^+$  or  $\text{Ga} - \text{O}^-$  surface groups. In this way dipole layers of different sign and magnitude can be formed at the solid-liquid interface, which act as an effective gate voltage and which account for the established pH-sensitivity of III-nitride surfaces [109].

### 6.3 Surface oxidation processes and hydrocarbon response

It has been observed before that ethanol promotes the PL of InGaN/GaN transducers. The main motivation of the research in this section was finding an explanation of the PL enhancing mechanism of ethanol. As both water and ethanol enhance the PL, a straight-forward hypothesis was that the reason for the PL enhancement is rooted in a chemical similarity of the two molecules. An interesting similarity of water and ethanol is that both can undergo auto-protolysis reactions. In the case of ethanol, the auto-protolysis reaction can be expressed as [110,111]:



Here, R denotes the C-chain rest of the alcohol without the hydroxyl group. The auto-protolysis describes a process where two molecules of the same kind exchange a proton. This would be a process completely equivalent to the auto-protolysis of water



where two water molecules transform into hydroxide ( $\text{OH}^-$ ) and hydroxonium ( $\text{H}_3\text{O}^+$ ) ions by exchanging a proton.

The auto-protolysis hypothesis agrees with the observations made on ethanol diluted in synthetic air. Here we have observed an enhancing PL response at high temperatures and a mixed quenching/enhancing response at room temperature; i.e. behaviour completely analogue to the one observed for water vapour diluted in SA. Dissimilar to the observations made on water vapour, PL enhancement effects with ethanol could not be observed in nitrogen backgrounds. We therefore conclude that oxygen is only a facilitator of PL enhancements effects in water but a key enabler in the case of alcohols. As a consequence, alcohols do not seem to undergo the same kinds of photo-electrochemical auto-protolysis reactions on InGaN/GaN surfaces as water.

Previous measurements on MEMS pellistor gas sensors revealed that hydrocarbons - with the exception of methane - start to undergo combustion reactions in the temperature range between 200°C-300°C on flat, thin-film catalysers [112]. Here, UV-illumination lowers the onset of surface oxidation processes to temperatures below 200°C.

Combustion products of hydrocarbons are water besides CO and CO<sub>2</sub>. CO<sub>2</sub> only showed a very weak or negligible PL response, by contrast, water has been identified as a key enabler of PL enhancement effects. It therefore appears plausible to propose that the enhancement effects observed with hydrocarbons are caused in an indirect way, triggered by the consumption of quenching oxygen adsorbates and the adsorption of reaction water. In Figure 6.6 (a) the PL response of the tested hydrocarbons at a constant concentration of 2000 ppm is shown. In Figure 6.6 (b) this response is compared to the number of oxygen adsorbates removed and the numbers of water adsorbates created in case these hydrocarbons undergo full combustion. The maximum response correlates with this number for hydrocarbon with only single C-C bonds (blue and red line). However, the series with three C atoms but increasing bond order shows an anti-correlated behaviour with respect to the expected number of oxygen and water adsorbates (Figure 6.6 (b). This observation suggests that full combustion does not take place at moderately heated and UV illuminated InGaN/GaN surfaces. In contrast, only species-specific, partial reaction products seem to be formed.

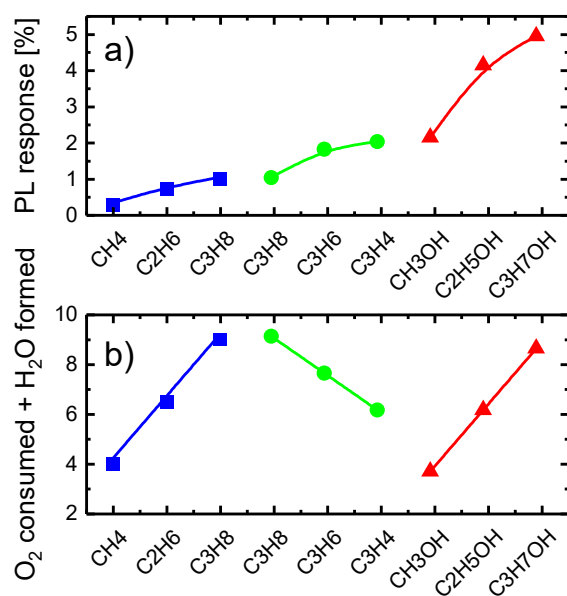


Figure 6.7. (a) enhancing PL response of InGaN/GaN NWAs when exposed towards 2000 ppm of different hydrocarbons in a background of synthetic air; (b) number of PL-quenching O<sub>2</sub> adsorbates consumed plus numbers of PL-enhancing H<sub>2</sub>O adsorbates formed in case the hydrocarbon species on the abscissa are completely converted into their final combustion products.

The reaction equations in Figure 6.8 and Figure 6.9 show how methanol and methane combust into  $\text{CO}_2$  and  $\text{H}_2\text{O}$ . In both cases the reaction pathways include the intermediate formation of  $\text{H}_2$  which can easily be desorbed. In case intermediate  $\text{H}_2$  molecules do indeed desorb, the number of water adsorbates is reduced and the PL enhancement effect is lowered as well.

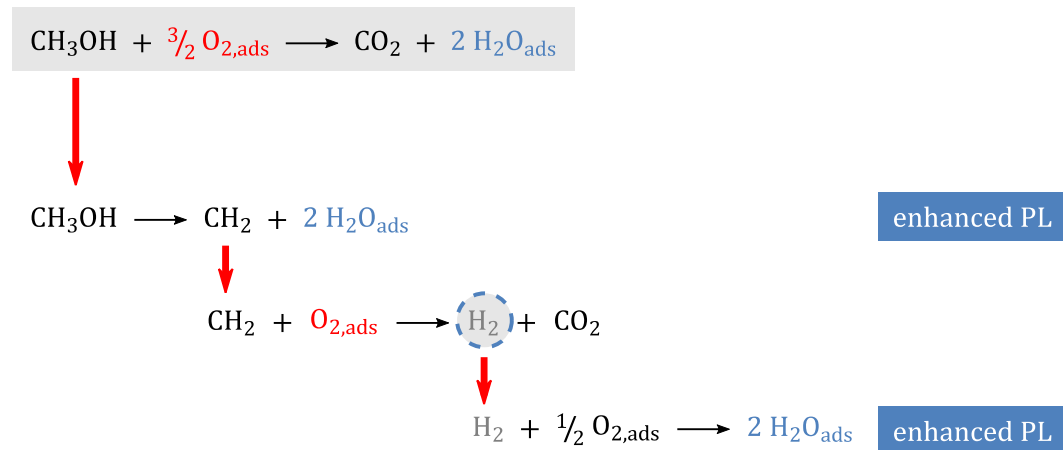


Figure 6.8. Reaction path for methanol into  $\text{CO}_2$  and  $\text{H}_2\text{O}$ . The intermediate  $\text{H}_2$  molecule may desorb which lowers the amount of PL enhancing water molecules in the equation.

In the case of the reaction pathway of methane (Figure 6.9) a complete desorption of the intermediate  $\text{H}_2$  molecules would result in zero  $\text{H}_2\text{O}$  production and therefore an unaltered PL. At elevated temperatures this effect becomes less likely and more intermediate  $\text{H}_2$  are getting combusted forming more water molecules, thus enhancing the PL.

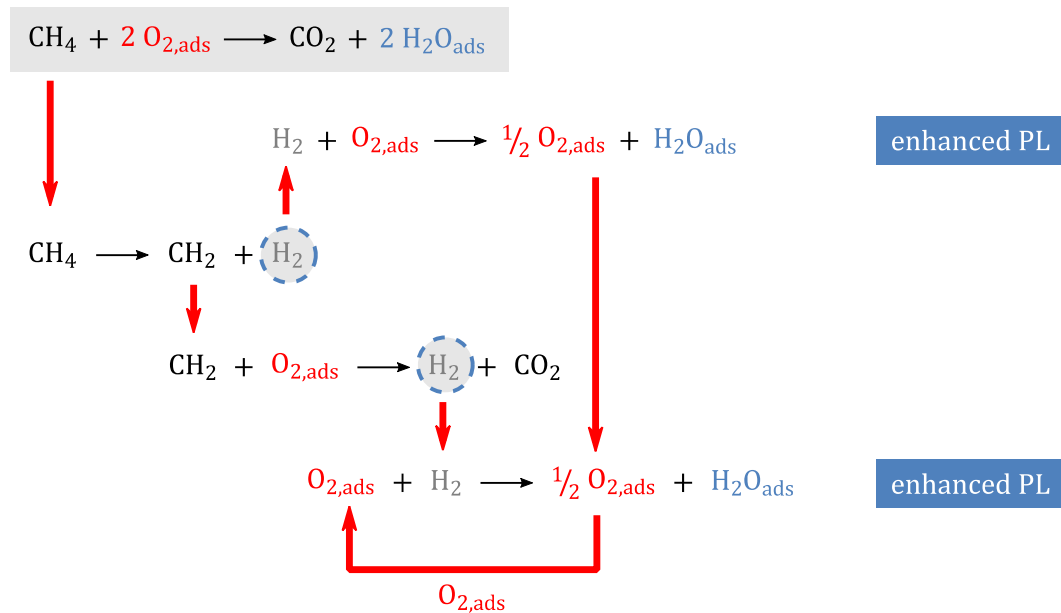


Figure 6.9. Reaction path for methane into  $\text{CO}_2$  and  $\text{H}_2\text{O}$ . Similar to the reaction path of methanol, the intermediate  $\text{H}_2$  molecule may desorb which lowers the amount of PL enhancing water molecules in the equation.

## 6.4 Modelling the chemical sensitivity of InGaN/GaN nanowires

In the following a model is described which allows the chemical sensitivity of photoluminescent InGaN/GaN heterostructure nanowires to be quantitatively analysed. The model assumes that the intrinsic photoluminescence (PL) of these nanowires is partially quenched by a non-radiative recombination channel leading through native surface sites which naturally develop on pure and naturally oxidised InGaN/GaN surfaces. Chemical sensitivity is explained by adsorbate-induced changes in the electron- and hole-trapping cross sections of these native surface sites. As the model presented below combines Langmuir adsorption with non-radiative surface recombination, we name this model “LAR” – Langmuir adsorption and recombination model.

Specifically, this model assumes that  $e^- - h^+$  pairs are generated in the InGaN wells by near-violet light illumination. The generated mobile charge carriers subsequently recombine in pairs emitting longer-wavelength photons which are observable as

green luminescence light. Once photo-generated, charge carriers can reach the surface and become trapped with some probability at the native surface sites of the InGaN wells. The trapped charge carriers subsequently can either be thermally re-emitted to conduction and valence bands of the InGaN well or recombine in pairs in a non-radiative manner by the transfer of electrons from occupied electron trapping to nearby occupied hole trapping sites. A possible candidate for such close pairs of electron and hole traps are the previously discussed Lewis-acid-base pair (LAB) sites. In principle, however, other types of defects may play this role as well.

As will be shown below, surface trapping of electrons and holes requires small thermal activation energies in the range of tens of milli-electron-volts. Therefore, the intrinsic PL is high at very low temperatures and becomes thermally quenched as room temperature and temperatures beyond are approached. Operating InGaN/GaN nanowires at such elevated temperatures in a reactive gas atmosphere, the surrounding gas species may adsorb on the nanowire surfaces, thus modifying their electron- and hole trapping properties. These latter effects make the intrinsic PL chemically sensitive. Gas sensing experiments have shown that such adsorbate interactions can cause both PL quenching ( $O_2$ ,  $NO_2$ ,  $O_3$ ) as well as PL enhancement (dissociative adsorption of water vapour).

#### 6.4.1 Qualitative considerations

The above processes are visualized in a schematic manner in Figure 6.10. Shown there are two vertical cross sections through a nanowire. Whereas the left-hand part visualizes those processes leading to thermal quenching, the right-hand part focusses on adsorbate processes leading to changes in the electron and hole trapping cross sections of the native LAB centres. Also indicated in the bottom panels of Figure 6.10 is the necessity of compensating hole charges in the sub-surface regions in case electron-trapping proceeds at a higher rate than hole trapping.

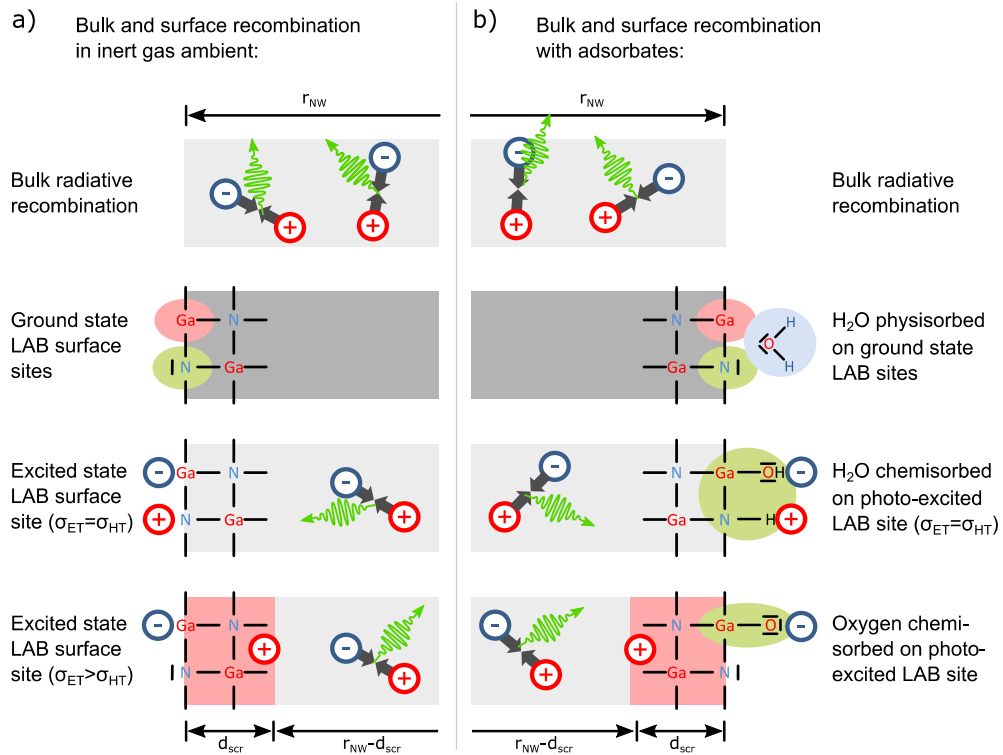


Figure 6.10. Cross section through an illuminated InGaN/GaN nanowire. Left-hand side: processes leading to thermal PL quenching through native LAB sites; right-hand side: modification of electron and hole trapping cross sections of native LAB sites through adsorbate binding.

Attempting to arrive at a quantitative description of these processes, rate equations for the above processes need to be formulated and these equations need to be solved. To arrive at such equations, we start with some qualitative considerations which build on the processes visualized above. The key message is that the transfer of electrons and holes to native surface sites, surface adsorbates and sub-surface positive space charge region reduces the bulk electron and hole densities thus reducing the radiative recombination rate and hence the PL intensity. Since the InGaN material is an n-type semiconductor, luminescence is mainly limited by the hole density, as holes are the minority charge carriers. Overall charge neutrality is maintained by balancing charges between surface sites, adsorbates and sub-surface space charge region, leaving the bulk region neutral and the free charge carrier densities  $n_{bulk} = p_{bulk}$  balanced under all conditions.

While in the idealized case of zero surface recombination electro-neutrality is trivially maintained as electrons and holes are generated in pairs and recombine in pairs ( $n_0 = p_0$ ), the situation gets more complicated when trapping and recombination processes are allowed to occur at InGaN nanowire surfaces. Suppose that electrons and holes are trapped at equal rates at native recombination centres at the nanowire surface, the bulk electron and hole densities are lowered relative to the zero-surface recombination case. Charge neutrality is still maintained inside the bulk ( $n = p$ ) as electrons and hole densities are reduced symmetrically and as the areal densities of negatively charged electron traps  $n_{ET}^{neg}$  and positively charged hole trapping centres  $n_{HT}^{pos}$  at the surface appear equally ( $n_{ET}^{neg} = n_{HT}^{pos}$ ). Charge neutrality in this symmetrical case is maintained separately both inside the bulk and at the surface. The more probable case is with unequal rates for electron and hole-trapping. When assuming that holes are trapped at a lower rate than electrons, the hole density in the bulk is initially higher than the electron density. As concomitantly, more negatively charged electron traps are generated at the surface than positively charged hole traps ( $n_{ET}^{neg} > n_{HT}^{pos}$ ), electrical fields are generated that attract positive charge carriers. In this region a positively charged space charge region is created which is sufficiently large to shield the bulk from the negative excess charge on the surface. This region may be composed by both, positively ionized donor atoms and by mobile photogenerated holes. In equilibrium the density of holes and electrons remaining in the bulk is lowered and therefore the number of bi-molecular radiative recombination processes is reduced. Overall charge neutrality is maintained by the balancing of charges originating from the native surface recombination centres and the charge of positive sub-surface space charge region. In the case of additional gas adsorption on the surface we assume oxidizing gas species ( $O_2$ ,  $NO_2$ ,  $O_3$ ) for definiteness. As all these gases have a high electron affinity thus will predominantly trap electrons from the bulk and further reduce the electron density. As a consequence the sub-surface space charge layer is increased, shielding the bulk from the additional negative charges on the surface. As in this process both the bulk electron and hole densities is symmetrically reduced, thus the output of luminescence photons is further reduced.

## 6.4.2 Governing equations of the recombination model

Turning these considerations into quantitative predictions that can be compared to experiment, rate equations need to be formulated and to be solved for the limit of steady-state sensor operation. Following the considerations above these equations will involve four key time constants: the radiative lifetime of the charge carriers in the bulk  $\tau_{rad}$ , the lifetimes with regard to electron- and hole trapping at surface sites  $\tau_{ET}$  and  $\tau_{HT}$ , respectively, and the lifetime of non-radiative recombination  $\tau_{nr}$  at the surface. In the following a set of rate equations will be developed following the scenarios illustrated in Figure 6.10.

### Radiative recombination

First, an idealized form of nanowire is considered, in which photogenerated electrons and holes hitting the surface are elastically reflected into the interior, thus leaving radiative recombination as the only recombination channel. For simplicity it is assumed that the number of photogenerated charge carriers is large compared to the number of intrinsic charge carriers. In this case the densities of photogenerated electrons and holes,  $n$  and  $p$ , are determined by the optical generation rate  $g_{LED}$  and the bimolecular recombination rate  $\gamma_{lum}$  of the charge carriers:

$$\frac{dn(t)}{dt} = \frac{dp(t)}{dt} = g_{LED} - \gamma_{lum} n(t)p(t) \quad (6.5)$$

The generation rate  $g_{LED}$  depends on the input optical power  $P_{opt}$  and on the rate at which input photons are absorbed inside the InGaN well regions. The recombination rate  $\gamma_{lum}$  is indirectly proportional to the radiative lifetime  $\tau_{rad}$  of the charge carriers multiplied by the volume of the luminescent InGaN region  $V_{well}$ :

$$\gamma_{lum} = \frac{V_{well}}{\tau_{rad}} \quad (6.6)$$

As electrons and holes are produced in pairs and as these recombine in pairs, charge neutrality is trivially maintained.

Assuming illumination conditions comparable to those used in our experiments, estimates of the time-averaged numbers of electrons and holes inside the well regions

can be obtained. With a radiative lifetime of  $\tau_{rad} \approx 10^{-10}$  s [113], the time-averaged numbers of electrons and holes in the InGaN well region are in the order of

$$N_0 = P_0 < 0.1 \quad (6.7)$$

i.e. far less than one electron per nanowire. On a single nanowire level, one is therefore looking at sequences of elementary processes of generation, radiative recombination, charge-carrier trapping and bi-molecular non-radiative surface recombination. Due to the short lifetime, however, roughly  $10^9 - 10^{11}$  luminescence photons will be observed within one second, which means that on the time scale of stationary experiments the statistics of large numbers and of smoothly varying distributions of charge carriers and electrical fields still appears to be justifiable. This kind of statistical averaging is further amplified by the fact that experimental observations are performed on large arrays of nanowires, in the order of  $10^9$  to  $10^{10}$  nanowires/cm<sup>2</sup>.

### 6.4.3 Non-radiative recombination through intrinsic surface sites

When the assumption of elastically reflecting surfaces is dropped, additional carrier trapping processes at the surface need to be considered:

$$\frac{dn}{dt} = g_{LED} - \frac{V_{well}}{\tau_{rad}} n(t)p(t) - \frac{n_S(t)}{\tau_{ET}} \quad (6.8)$$

$$\frac{dp}{dt} = g_{LED} - \frac{V_{well}}{\tau_{rad}} n(t)p(t) - \frac{p_S(t)}{\tau_{HT}} \quad (6.9)$$

In these equations  $n_S$  and  $p_S$  are the surface concentrations of charge carriers

$$n_S = n_{bulk} \exp\left[-\frac{qV_S}{k_B T}\right] \quad (6.10)$$

$$p_S = p_{bulk} \exp\left[\frac{qV_S}{k_B T}\right] \quad (6.11)$$

with  $qV_S$  standing for the surface band bending;  $\tau_{ET}$  and  $\tau_{HT}$ , in turn, are the carrier lifetimes controlling electron and hole trapping at the surface:

$$\tau_{ET}(\sigma_{ET}) = \left[ \frac{S_{well}}{V_{well}} v_{th} \sigma_{ET} n_{ET}^{neut} \right] \quad (6.12)$$

$$\tau_{HT}(\sigma_{HT}) = \left[ \frac{S_{well}}{V_{well}} v_{th} \sigma_{HT} n_{HT}^{neut} \right] \quad (6.13)$$

These latter time constants depend on the cross sections  $\sigma_{ET}$  and  $\sigma_{HT}$  for electron and hole trapping at neutral surface sites on the InGaN surface  $S_{well}$ , which are denoted  $n_{ET}^{neut}$  and  $n_{HT}^{neut}$ , respectively. For simplicity we assume that these neutral sites constitute a fraction  $f_{neut}$  of all LAB sites at the surface. This latter parameter  $f_{neut}$  will later reveal from experiment.

Once trapped, charged centres will be built up at the surface:

$$\frac{dn_{ET}^{neg}}{dt} = \frac{V_{well}}{S_{well}} \frac{n_S(t)}{\tau_{ET}} - S_{well} \frac{n_{ET}^{neg} n_{HT}^{pos}}{\tau_{nr}} \quad (6.14)$$

$$\frac{dn_{HT}^{pos}}{dt} = \frac{V_{well}}{S_{well}} \frac{p_S(t)}{\tau_{HT}} - S_{well} \frac{n_{ET}^{neg} n_{HT}^{pos}}{\tau_{nr}} \quad (6.15)$$

In these latter equations  $n_{ET}^{neg}$  and  $n_{HT}^{pos}$  are the areal densities of electron- and hole traps which reside in their charged states and  $\tau_{nr}$  is the lifetime with which these states disappear in bi-molecular, non-radiative recombination processes. These latter processes likely proceed by electron tunnelling from negatively charged electron traps to a nearby positively charged hole traps. Because of the relatively large InGaN band gap we have neglected in equations (6.14) and (6.15) the possibility of thermal re-emission of surface-trapped charge carriers back to the conduction and valence bands inside the InGaN wells.

In the likely case that electron trapping proceeds at different rates than hole trapping, charge imbalances evolve in the bulk and at the surfaces. The imbalances generate electrical fields which shield the well interior from the net electrical charges residing on the well surface. Assuming a situation in which electron trapping exceeds hole trapping the negative surface charge attracts positive charge carriers building up positive space charge region. The space charge region is composed by two components: First the positively ionized donator atoms and second the mobile photogenerated

holes. For lower donor concentration one can neglect the positively charged donor atoms and assume that the space charge region is mainly built up by mobile charge carriers.

With the bulk electron densities being reduced to the level  $n_1 = p_1 = n_0 - \Delta n$  determined by the demands of those traps with the larger cross sections, the emission rate of luminescence light can be calculated:

$$n_{ph} = \frac{V_{well}}{\tau_{rad}} (n_0 - \Delta n)^2 \approx \frac{V_{well}}{\tau_{rad}} n_0^2 \left(1 - 2 \frac{\Delta n}{n_0}\right) \quad (6.16)$$

Here  $n_0$  is the charge carrier density in the absence of surface recombination. In this latter equation we have further assumed that  $\Delta n \ll n_0$ .

#### 6.4.4 Adsorbate effects on surface recombination

In case gases additionally adsorb on the native surface sites, the areal densities of native recombination centres are reduced and a fraction of them is replaced by surface sites with different trapping cross sections:

$$\frac{dn}{dt} = g_{LED} - \gamma_{lum} n(t)p(t) - n_S(t) \frac{V_{well}}{S_{well}} [\sigma_{ET}(N_{ET}^{neut} - N_{ads}^{neut}) + \sigma_{ET,ads} N_{ads}^{neut}], \quad (6.17)$$

$$\frac{dp}{dt} = g_{LED} - \gamma_{lum} n(t)p(t) - p_S(t) \frac{V_{well}}{S_{well}} [\sigma_{ET}(N_{HT}^{neut} - N_{ads}^{neut}) + \sigma_{HT,ads} N_{ads}^{neut}]. \quad (6.18)$$

Rearranging terms on the right-hand sides, it is found that the effects of adsorption can be reduced to changes in the average cross sections of surface sites which are coverage  $\theta$  dependent:

$$\sigma_{ET}(\theta) = \sigma_{ET}(\theta = 0) \left[1 + \theta \frac{g_{neut}}{f_{neut}} \left(\frac{\sigma_{ET,ads}}{\sigma_{ET}} - 1\right)\right] \quad (6.19)$$

$$\sigma_{HT}(\theta) = \sigma_{HT}(\theta = 0) \left[1 + \theta \frac{g_{neut}}{f_{neut}} \left(\frac{\sigma_{HT,ads}}{\sigma_{HT}} - 1\right)\right] \quad (6.20)$$

In these latter equations  $g_{neut}$  is the fraction of adsorbates that have remained neutral after adsorption and thus maintained their capability of trapping mobile electrons or holes. As the factor  $f_{neut}$ , the parameter  $g_{neut}$  will reveal later from experiment. For the moment we note that adsorbate binding can both enhance or reduce the cross sections of the native surface sites, thus allowing both PL quenching and PL enhancement to occur.

Similarly, equations (6.14) and (6.15) need to be modified in the adsorption case. The important result of equations (6.19) and (6.20) is that in the adsorbate case the same set of equations as in the non-adsorbate case can be used, if it is realized that the electron and hole lifetimes  $\tau_{ET}$  and  $\tau_{HT}$  both have become functions depending on the adsorbate coverage  $\theta$ .

With the help of these coverage-dependent lifetimes the gas response  $R_{gas}$  of the InGaN nanowires can be obtained by comparing the levels of luminescence light output  $n_{ph}$  under gas exposure and under clean-air  $n_{ph,nr}$  or reference conditions  $n_{ph,ads}$ :

$$R_{gas} = \frac{n_{ph,ads} - n_{ph,nr}}{n_{ph,nr}} \quad (6.21)$$

#### 6.4.5 Steady-state solutions

To obtain results which can be compared to experimental data, steady-state solutions to the above equations need to be found. Putting all time derivatives in equations (6.8), (6.9) and equations (6.14), (6.15) equal to zero, solutions for  $n$  and  $p$  can be found:

$$n = \frac{1}{2} \frac{\tau_{rad}}{V_{well} \tau_{HT}} \exp\left(\frac{q V_S}{k_B T}\right) \left[ \sqrt{1 + 4 V_{well} g_{LED} \tau_{rad} \left(\frac{\tau_{ET} \tau_{HT}}{\tau_{rad}^2}\right)} - 1 \right] \quad (6.22)$$

$$p = \frac{1}{2} \frac{\tau_{rad}}{V_{well} \tau_{ET}} \exp\left(-\frac{q V_S}{k_B T}\right) \left[ \sqrt{1 + 4 V_{well} g_{LED} \tau_{rad} \left(\frac{\tau_{ET} \tau_{HT}}{\tau_{rad}^2}\right)} - 1 \right] \quad (6.23)$$

The occurrence of surface band bending terms in these results implies that the compensation of charge imbalances imposes a radial dependence on the charge carrier concentrations not initially foreseen. This is not a serious problem as only the bulk concentrations  $n_{bulk}$  and  $p_{bulk}$  are of concern when the output of luminescence light needs to be predicted:

$$n_{bulk} = p_{bulk} = \frac{1}{2} \frac{\tau_{rad}}{V_{well} \tau_{HT}} \left[ \sqrt{1 + 4 V_{well} g_{LED} \tau_{rad} \left( \frac{\tau_{ET} \tau_{HT}}{\tau_{rad}^2} \right)} - 1 \right] \quad (6.24)$$

The magnitude of the surface band bending  $qV_s$  (equations (6.10) and (6.11)) reveals from the fact that under stationary conditions electrons and holes need to be trapped at equal rates at the surface to maintain stationarity. From equations (6.8) and (6.9) one obtains:

$$\frac{n_s}{\tau_{ET}} = \frac{p_s}{\tau_{HT}} \quad (6.25)$$

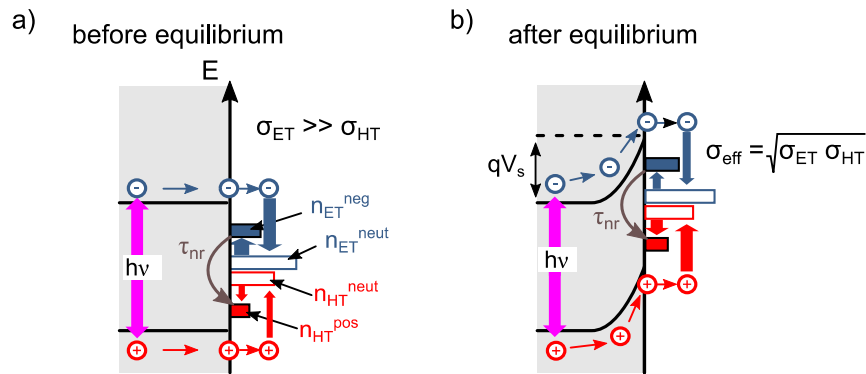
and with equations (6.22) and (6.23):

$$qV_s(\theta) = \frac{k_B T}{2} \ln \left[ \frac{\sigma_{ET}(\theta)}{\sigma_{HT}(\theta)} \right] \quad (6.26)$$

By inserting this latter result into equations (6.22) and (6.23) and considering that the time constants for electron and hole capturing are a function of the trapping cross sections, one finds that the trapping cross section only come in combination. This can be interpreted that the surface band bending changes the microscopic trapping cross sections  $\sigma_{ET}(\theta)$  and  $\sigma_{HT}(\theta)$  can be combined into a single effective value, given by the geometric mean of both values:

$$\sigma_{eff}(\theta) = \sqrt{\sigma_{ET}(\theta) \sigma_{HT}(\theta)} \quad (6.27)$$

This effect is illustrated in Figure 6.11.



Surface band bending - Balancing of trapping and recombination processes

Figure 6.11 Development of equilibrium band bending leading to charge equilibrium between surface and sub-surface regions and equal electron- and hole trapping rates at surface electron and hole trap states.

This latter result emphasizes the rate balancing role of the surface band bending and of the inversion layers built up in the sub-surface regions to compensate any imbalances in the surface charge densities. Figure 6.12 shows a sample evaluation of equation (6.26) which demonstrates that the effects of surface band bending remain moderate even in case large imbalances in cross sections should occur.

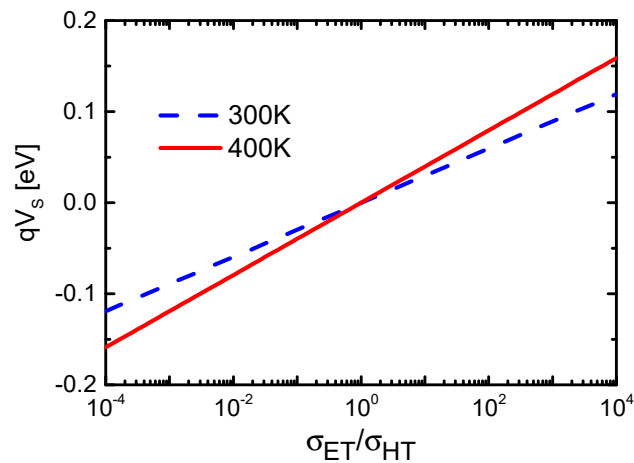


Figure 6.12 Surface band bending as a function of the ratio of electron- and hole trapping cross sections. Extreme differences in electron and hole trapping cross sections only lead to moderate levels of surface band bending.

The electrostatically balanced bulk concentrations of charge carriers, finally, determine the luminescence light output:

$$n_{ph}(\theta) = \frac{1}{4} \frac{V_{well}}{\tau_{rad}} \left( \frac{\tau_{rad}^2}{\tau_{ET}\tau_{HT}} \right) \left[ \sqrt{1 + 4 V_{well} g_{LED} \tau_{rad} \left( \frac{\tau_{ET}\tau_{HT}}{\tau_{rad}^2} \right) - 1} \right]^2 \quad (6.28)$$

Using equation (6.21) the final formula for the observable gas response can be found:

$$R_{gas}(\theta) = \frac{1}{\left[ 1 + \frac{g_{neut}}{f_{neut}} \left( \frac{\sigma_{eff}(\theta)}{\sigma_{eff(0)}} - 1 \right) \right] \left[ 1 + \frac{g_{neut}}{f_{neut}} \left( \frac{\sigma_{eff}(\theta)}{\sigma_{eff(0)}} - 1 \right) \right]} \quad (6.29)$$

## 6.4.6 Comparison to experiment

### Thermal quenching of photo-luminescence

In the set of governing equations developed above, it has been assumed that the radiative recombination of charge carriers does not have any temperature dependence at all. The data points in Figure 6.13, however, do show that the intrinsic luminescence of InGaN/GaN nanowires does exhibit a strong temperature dependence. Within the LAR model developed above such a temperature dependence can be accounted for by considering that photo-generated charge carriers have to surmount small energetic barriers to reach the surface and to become trapped inside a pair of closely neighbouring electron- and hole trap states. The temperature dependence is introduced by making the effective trapping cross section  $\sigma_{eff}$  temperature-dependent by introducing a Boltzmann term:

$$\sigma_{eff}(T) = \sigma_t \exp \left[ -\frac{q V_b}{k_B T} \right] \quad (6.30)$$

In this latter equation the cross section  $\sigma_t = 10^{-15} \text{cm}^2$  is an often-assumed reference value for charge carrier trapping into neutral defect centres [114].

Fitting equation (6.30) to the experimental data it is found that a small amount of activation energy of

$$q V_b = 0.02 \text{ eV} \quad (6.31)$$

for the effective trapping cross section is required for a good alignment of experimental data with calculated values in Figure 6.13.

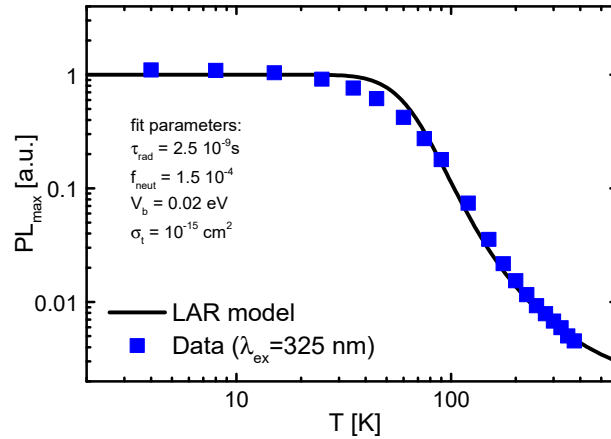


Figure 6.13 Temperature quenching of the PL intensity. Square points represent measured data. Solid lines represent a fit to equation (6.28) with the parameters listed in the inset.

The introduction of this Boltzmann term can be interpreted in different ways. One possible interpretation is to assume that the trapping process requires small amounts of energy to change bond configuration of trapping centres. The energy levels of some milli-electron volts may also indicate a phonon assisted trapping process. Another explanation is that the neglect of the thermal re-emission of trapped charge carriers is not entirely justified. The introduction of a thermal re-emission factor, containing a Boltzmann term, into the rate equation could possibly explain a temperature-dependent photon emission rate. When the trapping states are close to those of the band edges, as reported in [115], the small activation energy of few milli-electron-volts can be explained. Further, re-emission of trapped charge carriers into the bulk could explain why the model requires longer life times  $\tau_{rad} > 2.5 \cdot 10^{-9}$  s of photogenerated electrons and holes as reported in literature [113].

With regard to the absolute magnitude of the surface charges, the relevant observation is that the experimentally observed thermal quenching data can be fitted by assuming a fraction of

$$f_{neut} \approx 4 \times 10^{-4} \quad (6.32)$$

of neutral LAB pairs on the surface, which is only a small fraction of all potentially possible LAB pairs on the surface ( $n_{LAB} \approx 2 \times 10^{15} \text{ cm}^{-2}$ ). With surface trapping and non-radiative recombination processes predominantly converting electron traps between their neutral and negatively charged states, the assumption of equal areal densities of neutral electron- and negatively charged electron traps appears to be plausible. Putting  $f_{neg} \approx f_{neut}$  one obtains a surface charge density of

$$Q_S^{neg} \approx 10^{12} \frac{q}{\text{cm}^2} \quad (6.33)$$

which with the help of Poisson's equation converts into a surface electrical field of

$$E_S \approx 10^5 \frac{V}{\text{cm}} \quad (6.34)$$

i.e into a value close to the Weisz limitation [116].

### 6.4.7 Adsorbate effects on photo-luminescence

Equation (6.29) shows that the gas response is dependent on the adsorbate coverage  $\theta(p_{gas})$  of the surfaces. As described above these coverages follow Langmuir isotherms over large ranges of gas partial pressure  $p_{gas}$ :

$$R_{gas}(p_{gas}) = \alpha_{sat}(T)\theta(p_{gas}, T) \quad (6.35)$$

As already discussed all those functional dependences  $\theta(p_{gas})$  for the different gases, the focus in this section is on the limiting values of gas response which arise in the limit of  $\theta = 1$  and on those pieces of information derive that the temperature dependencies of  $\alpha_{sat}(T)$ . As a first result we show in Figure 6.14 the experimentally determined values of  $\alpha_{sat}(T)$  (data points) which have been obtained by exposing InGaN/GaN nanowires to high concentrations of  $\text{O}_2$ ,  $\text{NO}_2$ ,  $\text{O}_3$  and  $\text{H}_2\text{O}$ . Also shown in Figure 6.14 are fits to equation (6.29). The key information that derives from these fits are those energy barriers that need to be surmounted as electrons or holes are

being transferred from the bulk to their respective surface trapping centres. The values of these activation energies are shown in Figure 6.15 (a). These values are all positive except for H<sub>2</sub>O. Positive values indicate that the surface barriers are electron barriers which impede the flow of electrons to the InGaN surface. The negative barrier in the case of H<sub>2</sub>O indicates that holes are attracted to the surface at larger rates than electrons and that, therefore, the flow of holes to the surface is being impeded.

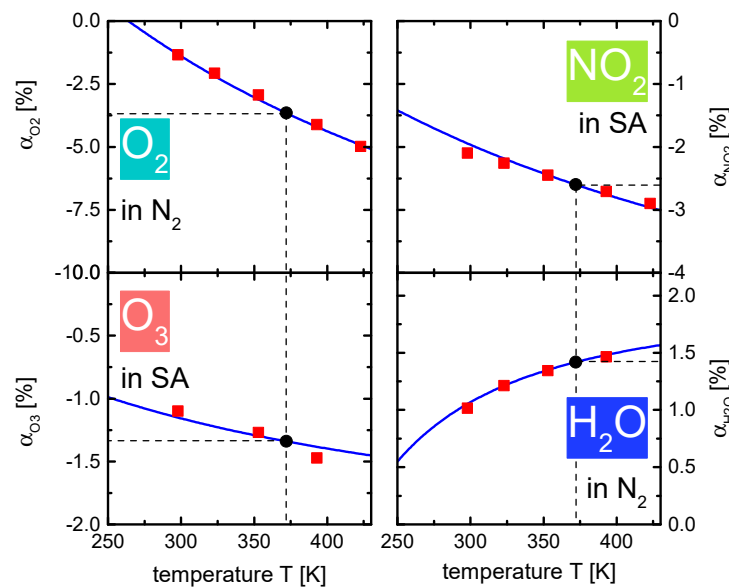


Figure 6.14 Saturated values of gas response as obtained on InGaN/GaN nanowire arrays. Data points represent maximum response values obtained from LAR fits to concentration-dependent gas response data. Solid lines are response values calculated using equation (6.29) of the LAR model.

The most interesting piece of information that reveals from these fits are the magnitudes of the surface energy barriers. Figure 6.15 lists these fitted values: in Figure 6.15 (a) the activation energies for the trapping cross section are listed, and in Figure 6.15 (b) the effective trapping cross section are shown. The fitted activation energies reveal important differences between the native surface sites (LAB), on the one hand, and LABs modified either by adsorption of oxidising gases or water vapour, on the other hand. Whereas for oxidising gases positive barrier energies are revealed, barrier energies become negative in the case of H<sub>2</sub>O. This difference is also reflected in the effective cross section  $\sigma_{eff}$  plotted in Figure 6.15 (b). Whereas oxidising gases

have increasingly higher cross sections than LABs, the converse is true in the case of  $\text{H}_2\text{O}$  which whose mean cross section values are lowered.

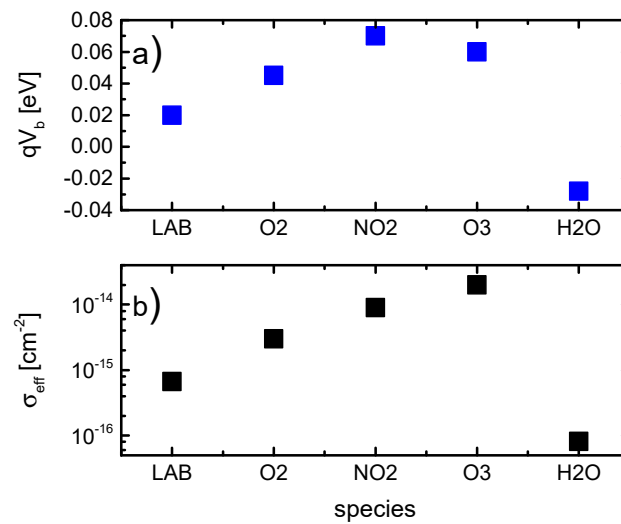


Figure 6.15 a) magnitude of surface barriers as derived from the fits in Figure 6.14; b) ratios of electron-to-hole trapping cross sections as derived from the data of a) and from equation (6.27).



## 7 Summary and Outlook

### 7.1 Summary

In this work gas sensing systems based on InGaN/GaN nanowire transducers (NWA) have been studied. These opto-chemical transducers respond to adsorbed gases via changes in the photoluminescence yield. It was shown that such systems are robust and stable and that these can be used at temperatures ranging from room temperature to over 150°C. In the context of this work the mechanism of the underlying surface sensing reactions has been investigated. Based on experimental data several models explaining the sensing mechanism have been developed.

#### Langmuir-adsorption and surface recombination

The results showed that InGaN/GaN transducers respond with a reduced PL when exposed to oxidizing gases such as O<sub>2</sub>, NO<sub>2</sub> or O<sub>3</sub>. Adsorbates formed on the non-polar III-nitride surfaces effectively trap photogenerated charge carriers from the NWA bulk. A Langmuir-adsorption and surface recombination model (LAR) of the PL response was developed that can successfully reproduce the experimentally determined calibration curves, i.e. the PL response as a function of the applied gas concentration. The key parameter of the Langmuir adsorption component that determines the positions of the centres of the sensitivity windows, i.e. those gas concentrations at which 50% of the saturation response can be observed, is the Langmuir adsorption energy  $E_{ads}$ .  $E_{ads}$  values were found to be gas-species-dependent when compared at a common transducer temperature. For each gas  $E_{ads}$  was additionally found to be temperature-dependent. Successful fits to the LAR model require  $E_{ads}$  to rise approxi-

mately linearly with the transducer temperature, thus indicating a tightening adsorption as the transducer temperature is raised. Measurements of water vapour in nitrogen background revealed similar LAR characteristics. In contrast to the oxidising gases, water vapour consistently produced enhanced PL responses under conditions of equilibrium adsorption.

The LAR model was further expanded to explain the non-radiative recombination rate parameter. In this model, electron and hole trapping centres at native or extrinsic surface states are assumed. The cross section of these centres determines the lifetime of the charged surface states, which in turn influences the total number of charge carriers in the bulk and thus the radiative recombination rate. It was found that for successful fitting of the experimental data a temperature activation factor for the capture cross section is required. This model explains both, the observed temperature induced quenching of the PL and the temperature-dependent maximum gas response values to the test gas species.

### Competitive adsorption

The experimental data on the oxidising gas response revealed that the macroscopically observable Langmuir adsorption energy scales linearly with the absolute transducer temperature:  $E_{ads} \sim T$ . This temperature scaling of the adsorption energy was explained in terms of a model of competitive adsorption. Key assumption in this model is that the different oxidising gases compete for one and the same kinds of adsorption sites on the III-nitride surfaces. Within such a competitive scenario, competing gases A and B both follow conventional Langmuir adsorption isotherms, however, with effective adsorption energies being weighted averages of the molecular adsorption energies  $E_{ads,A}$  and  $E_{ads,B}$ , which the two gases would have in a non-competitive scenario. Over the entire experimentally observed temperature range, the effective adsorption energies were found to be smaller than the molecular adsorption energies  $E_{ads,A}$  and  $E_{ads,B}$  and to vary approximately linearly with the transducer temperature. At temperatures above the experimentally accessible temperature range, the effective adsorption energies are predicted to saturate at their non-competitive, species-dependent values  $E_{ads,A}$  and  $E_{ads,B}$ . Chemical bond considerations support this model of competitive adsorption as all gases tested may undergo chemical reactions with non-

---

polar InGaN/GaN surfaces. When such surfaces are fully reconstructed the Ga(In)-N nearest neighbours form Lewis acid base pairs that can form weak bonds with nitrogen lone pair orbitals. Upon photoexcitation the Ga(In)-N atoms form radicals with dangling bonds which can form – in a competitive manner - cross-linking bonds to H<sub>2</sub>O, O<sub>2</sub>, O<sub>3</sub>, NO<sub>2</sub> adsorbates.

### Complex water adsorption

Water adsorbates were observed to play a double role on non-polar III-nitride surfaces. Depending on the operation conditions, adsorbed water molecules can act as surface recombination centres when the transducers are operated at low temperature and/or under low excitation light intensities. At elevated temperatures and/or high light intensities surface passivation was observed. A theoretical model that can reproduce this complex and time-dependent behaviour of H<sub>2</sub>O adsorbates builds on a two-component adsorbate system where the first component is a PL enhancer and the second a PL quencher. Chemically, the first species was associated with single H<sub>2</sub>O adsorbates with the H<sub>2</sub>O lone pair orbitals supporting surface recombination processes and thus are PL quenching. The second species was associated with pairs of water molecules that had become photo-electrochemically split into OH<sup>-</sup> and H<sub>3</sub>O<sup>+</sup> ions. These ions can reversibly bind to photo-activated Lewis acid-base pairs, thus passivating them as recombination centres. It was further argued that such passivated surfaces may act as starting layers for multilayer BET adsorption, which also explains the observed pH sensitivity of GaN/InGaN NWAs when operated in liquid environments [117].

### Hydrocarbon response:

Experiments with hydrocarbon species showed that these hardly produce any PL response as long as they are diluted in N<sub>2</sub>. However, when these same gases are diluted in synthetic air, a clear enhancing gas response becomes apparent. As increased transducer temperatures promote this kind of PL response, a thermally activated process is indicated. Surface oxides form spontaneously on III-nitride surfaces as these are exposed to ambient air and are most likely crucial in the PL response. With surface

oxides and adsorbed oxygen playing key roles, it appears that hydrocarbons are detected in an indirect manner similar to the surface combustion processes taking place on conventional resistive MOX gas sensors [7,118]. As such surface combustion processes produce H<sub>2</sub>O adsorbates in addition to desorbing CO<sub>2</sub> molecules, the enhancing hydrocarbon response can be explained as arising from water-related surface passivation effects.

## 7.2 Outlook

### 7.2.1 Multifunctional fuel cell application in aircrafts

As mentioned in the introduction of this thesis, an investigation towards sensor systems for aircraft use has been the driving force behind this work. The results and the experience gained in studying the above-described III-nitride based opto-chemical sensor systems suggest that such sensor systems might indeed be useful to monitor and control fuel cell based auxiliary power units (APU) in aircrafts. At the same time these results have also shown that a number of issues still need to be resolved to fully arrive at this goal.

#### Fulfilled requirements

(i) Sensitivity towards target chemicals

The most important requirement of a gas sensor system for fuel cell systems is the capability of sensing the analytes of interest. The InGaN/GaN opto-chemical transducers are able to fulfil all those requirements. An interesting application of III-nitride opto-chemical sensors is making use of the pH-sensitivity of III-nitride transducers as reported in ref. [109,117]. In order to be acceptable in the cabin as sanitary water, the pH level of the fuel cell output water needs to lie within a narrow range which can be monitored using the opto-chemical sensors.

An important gas sensing application is the monitoring of the O<sub>2</sub> concentration in the fuel cell output gas to determine whether the oxygen concentration is low enough for fuel tank inertisation. The transducer used in this thesis for detecting oxidising gases

was able to measure oxygen in a wide concentration range from approx. 100 ppm to almost 20% before going into saturation. According to ref. [119] a reduction of the oxygen level from the naturally occurring 21% to about 12% results in a non-ignitable mixture for a fuel vapour concentration of 25%. The III-nitride oxygen sensor is therefore suited for this application.

The second gas sensing task is hydrogen detection for controlling the fuel cell system. As reported in ref. [31] the III-nitride NWA, similar to the ones investigated in this project, can be used as hydrogen sensors when the nanowire surface is platinum coated. The mechanism is based on hydrogen dissociation on catalytically acting platinum surfaces, followed by diffusion of atomic hydrogen through the Pt coating to the interface of the nanowire surface with the platinum. A hydrogen termination of the surface increases the surface band bending and reduces the surface recombination rate of photogenerated charge carriers. The platinum-coated transducer showed, according to ref. [31], a gas response suitable for the fuel cell application. There are many other hydrogen sensitive transducers with a similar principle of hydrogen dissociation and diffusion at platinum or palladium coatings [35,120–122]. An opto-chemical sensor system, however, offers the decisive advantage of media separation.

(ii) Media separation

Conventional hydrogen sensors mainly use an electrical readout principle, e.g. currents through a Pt gated field effect transistor or resistance measurements inside pellistors. The sensor itself or the electrical readout may act as a potential ignition source when measuring combustible gas mixtures. An optical system like the one investigated in this work could be applied in situations where explosive gas ambient is expected to occur, as it is the case in hydrogen fuel cells. The hydrogen lower explosive limit (LEL) is approx. 4% at 21% oxygen level. In kerosene tanks of aircrafts the LEL is in the same concentration range depending on the oxygen content. Therefore an oxygen sensor for monitoring the tank inertisation based on an optical readout could reduce the risk of explosion of the gas mixture.

## Problems and potential solutions

In the course of the gas sensing experiments performed in this work, a number of problems became apparent which limit the applicability of the present versions of PL sensor setups. In order to fulfil requirements of a fuel cell APU system, the following improvements still need to be made:

### (i) Temperature dependence

Sensitivity towards temperature changes is a problem that can be found in almost any kind of semiconductor sensor. The NWA transducer is no exception and its gas response shows a severe temperature dependence. As ambient temperatures in aircraft applications may change dramatically, ranging from  $-55^{\circ}\text{C}$  up to  $+50^{\circ}\text{C}$ , temperature compensation techniques are mandatory. A reliable sensor signal can only be obtained either by controlling the sensor operation temperature and setting it to a constant level, or by signal processing that corrects the PL signal for the ambient temperature changes. The first method was implemented in both PL sensing setups studied in this thesis. The heating device of the transducer has to be designed in a way that it does not act as a potential ignition source for explosive gas mixtures and should therefore be implemented in way that the flame point temperature cannot be reached in the gas atmosphere.

The absolute PL intensity may serve as a thermometer when a second transducer or a part of the gas sensing transducer is shielded from changing gas atmosphere.

### (ii) Gas cross sensitivity

The uncoated transducer shows cross sensitivity towards oxidizing gases and, to a much lesser extent, also to hydrocarbons. The cross sensitivity towards hydrocarbons only occurs in an oxygen-rich environment and at elevated temperatures. When measuring the oxygen content of the fuel cell exhaust, hydrocarbons are not expected and may therefore be neglected. However, when measuring the oxygen content in the kerosene tank, cross sensitivity towards fuel components are expected. Further measurements are required in order to determine whether the presently observed levels of cross sensitivity are tolerable in this application. Choosing sufficiently low sensor operation temperatures could reduce the hydrocarbon cross sensitivities to acceptable levels.

(iii) Water cross sensitivity

A cross contaminant that definitely has to be taken into account is water vapour. As extensively described in the results section, adsorbed water vapour can promote or reduce the baseline PL of the NWA. There are two potential sources for water cross contamination in oxygen gas sensing. First, water is produced by the fuel cell itself as a reaction product and secondly water vapour also occurs in the ambient air with concentrations depending on weather, temperature and flight altitude. Water-invariant transducers are required for this purpose. One way of dealing with this problem is implementing water vapour repellent membranes as described in ref. [123].

(iv) Speed of response/ recovery time

In the gas sensing tests reported above, well-defined gas flows had been used and a precise knowledge about target gas on and off times had been available. In this way, gas response and recovery time constants have been found to range in the order of minutes. The origin of this relatively slow response partially arises from the measurement setups and partially from the NWA transducers themselves. In comparative gas sensing tests on room-temperature-operated MOX materials, it was found that the speed of recovery can be enhanced by using forced flow conditions. Such flows were established using a nozzle that directly blows gas onto the MOX sensors [67,96], a method which appears to be applicable to NWA transducers as well.

Further, in order to arrive at improved versions of NWA transducers, current research uses electron beam lithography for manipulating growth substrates of InGaN/GaN nanowire arrays. The samples measured in this work have been produced using the self-assembling growth process. This process produces a high density of nanowires with broad distributions of NWA lengths and diameters. When controlling the layout of nucleation sites, more uniform nanowire arrays can be produced. It is expected that narrower distributions of NWA sizes will have a positive impact on the speed and uniformity of the gas response. In particular, nanowires grown on lithographically manipulated substrates can be made to grow nanowire arrays with larger inter-wire distances, which improves their gas access.

## 7.2.2 Further investigations

Future progress in the production of NWA arrays may offer new possibilities to re-address these issues. A number of those opportunities are addressed below.

### (i) LAR model adaptations

In the developed recombination model some assumptions were made which may be reconsidered for an improved version of the model. In the rate equations, a bi-molecular recombination process proportional to the number of electrons and holes is assumed. However, the InGaN material is n-type doped in the order of  $10^{-17} \text{ cm}^{-3}$  and due to the low photogeneration of positive charge carriers, a primarily hole-limited, monomolecular-like recombination could be justified and potentially simplify the equations. Additionally, the model in this thesis was only able to mimic the experimental data by introducing temperature-dependent capture cross-sections. With the introduction of a thermal re-emission rate of the trapped surface charge, the model could be supplemented by an explanation of the temperature dependence, which keeps the capture cross-sections constant.

### (ii) High temperature behaviour

Due to design and material limitations inherent in the PL-setups, the gas sensing tests on the InGaN/GaN transducers in this work had to be confined to the temperature range extending from room-temperature to approx.  $150^\circ\text{C}$ . The findings reported above suggest that it might be worthwhile to extend gas sensing experiments to temperatures higher than  $150^\circ\text{C}$ . It is expected that due to naturally occurring oxides on InGaN/GaN surfaces, the InGaN/GaN transducer will show MOX character at elevated temperatures. At these temperature levels it is expected that combustion processes occurring on the oxide surfaces will dominate the sensing mechanism. The limit for higher temperatures however is ultimately set by the photoluminescence yield of the nanowires. This thermal quenching limit of the gas sensing performance has not yet been reached in the current thesis.

### (iii) Investigation of uniform samples or single nanowire samples

The samples used in this thesis were grown on macroscopically large areas of approx.  $1 \text{ cm}^2$ . As mentioned in the previous section, it appears to be possible to produce

structured silicon substrates by means of e-beam lithography which influences the pattern of nanowire growth. As already stated this could potentially increase the speed of the sensor response. As the nanowires can be grown in a more or less free-standing configuration, microscope fluorescence techniques can be employed for probing single nanowires. In the current configuration an integrated PL signal is measured probing macroscopic areas containing many thousands of nanowires with large statistical variations in nanowire sizes and shapes. As a consequence, it is difficult to find out how the nanowire composition influences the gas sensing mechanism. Probing single, isolated nanowires would clearly resolve this issue.

(iv) Spectroscopic investigation during gas sensor operation

Single nanowires or highly uniform nanowire arrays would enable sharper PL spectra. As in this thesis only broad integrated luminescence spectra were detected, the possible existence of analyte-specific shifts in these spectra could not be detected. Additionally time resolved measurements could be employed to those samples, giving additional information about the bulk material and its surface reactions.

(v) New concepts employing InGaN/GaN NWAs

In some kinds of gas sensors, or in analytical laboratory equipment, a combination of several gas sensing principles helps to increase the device' performance. A popular example is the combination of a gas chromatograph with a mass spectrometer, so-called GC-MS, which are standard instruments for gas analysis in the lab.

For InGaN/GaN nanowires a similar technique could be employed as for instance combining InGaN/GaN NWA with an ion mobility spectrometer (IMS). IMS, in effect, are time-of-flight mass spectrometers that are able to operate at normal ambient pressure and which thus obviate the use of bulky and expensive vacuum equipment. In such a NWA/IMS combination the water splitting effect at illuminated InGaN/GaN surfaces could be used to produce atomic hydrogen or  $\text{H}_3\text{O}^+$  ions, which could then be used to charge up more complex analyte molecules with proton affinities higher than water. The produced analyte ions could then be analysed with regard to their ion mobility in an ion drift tube as in a standard IMS. The key advantage of using InGaN/GaN NWAs as an ion source would be replacing the radioactive ionisation,

which is used in nowadays IMS instruments and which severely limits their applicability. [124]

---

## Bibliography

- [1] R.A. Raguso, Wake Up and Smell the Roses: The Ecology and Evolution of Floral Scent, *Annu. Rev. Ecol. Evol. Syst.* 39 (2008) 549–569. doi:10.1146/annurev.ecolsys.38.091206.095601.
- [2] W.F. Brinkman, D.E. Haggan, W.W. Troutman, A history of the invention of the transistor and where it will lead us, *IEEE J. Solid-State Circuits.* 32 (1997) 1858–1865. doi:10.1109/4.643644.
- [3] N. Barbour, G. Schmidt, Inertial sensor technology trends, *IEEE Sens. J.* 1 (2001) 332–339. doi:10.1109/7361.983473.
- [4] D.K. Shaeffer, MEMS inertial sensors: A tutorial overview, *IEEE Commun. Mag.* 51 (2013) 100–109. doi:10.1109/MCOM.2013.6495768.
- [5] A.J.P. Theuwissen, CMOS image sensors: State-of-the-art, *Solid. State. Electron.* 52 (2008) 1401–1406. doi:10.1016/J.SSE.2008.04.012.
- [6] M. Bigas, E. Cabruja, J. Forest, J. Salvi, Review of CMOS image sensors, *Microelectronics J.* 37 (2006) 433–451. doi:10.1016/J.MEJO.2005.07.002.
- [7] N. Barsan, D. Koziej, U. Weimar, Metal oxide-based gas sensor research: How to?, *Sensors Actuators B Chem.* 121 (2007) 18–35. doi:10.1016/j.snb.2006.09.047.
- [8] M. Erfan, Y.M. Sabry, B. Mortada, K. Sharaf, D. Khalil, Mid infrared MEMS FTIR spectrometer, in: W. Piyawattanametha, Y.-H. Park (Eds.), *International Society for Optics and Photonics*, 2016: p. 97600K. doi:10.1117/12.2210973.
- [9] E.L. Holthoff, D.A. Heaps, P.M. Pellegrino, Development of a MEMS-Scale Photoacoustic Chemical Sensor Using a Quantum Cascade Laser, *IEEE Sens. J.* 10 (2010) 572–577. doi:10.1109/JSEN.2009.2038665.
- [10] K. Schjolberg-Henriksen, O. Schulz, A. Ferber, S. Moe, M. Lloyd, G. Muller, K.-H. Suphan, D.T. Wang, R.W. Bernstein, Sensitive and Selective Photoacoustic Gas Sensor Suitable for High-Volume Manufacturing, *IEEE Sens. J.* 8 (2008) 1539–1545. doi:10.1109/JSEN.2008.923588.
- [11] B. Bierer, J. Kneer, J. Wöllenstein, S. Palzer, MEMS based metal oxide sensor for

- simultaneous measurement of gas induced changes of the heating power and the sensing resistance, *Microsyst. Technol.* 22 (2016) 1855–1863. doi:10.1007/s00542-016-2862-y.
- [12] S. Capone, A. Forleo, L. Francioso, R. Rella, P. Siciliano, J. Spadavecchia, D.S. Presicce, A.M. Taurino, Solid state gas sensors: state of the art and future activities, *J. Optoelectron. Adv. Mater.* 5 (2003) 1335–1348.
- [13] J.I. Pankove, E.A. Miller, J.E. Berkeyheiser, GaN electroluminescent diodes, in: 1971 Int. Electron Devices Meet., IRE, 1971: pp. 78–78. doi:10.1109/IEDM.1971.188400.
- [14] S. Nakamura, GaN Growth Using GaN Buffer Layer, *Jpn. J. Appl. Phys.* 30 (1991) L1705–L1707. doi:10.1143/JJAP.30.L1705.
- [15] H. Amano, N. Sawaki, I. Akasaki, Y. Toyoda, Metalorganic vapor phase epitaxial growth of a high quality GaN film using an AlN buffer layer, *Appl. Phys. Lett.* 48 (1986) 353–355. doi:10.1063/1.96549.
- [16] H. Amano, M. Kito, K. Hiramatsu, I. Akasaki, P-Type Conduction in Mg-Doped GaN Treated with Low-Energy Electron Beam Irradiation (LEEBI), *Jpn. J. Appl. Phys.* 28 (1989) L2112–L2114. doi:10.1143/JJAP.28.L2112.
- [17] Nobelprize.org, The Nobel Prize in Physics 2014, (2014). [https://www.nobelprize.org/nobel\\_prizes/physics/laureates/2014/](https://www.nobelprize.org/nobel_prizes/physics/laureates/2014/) (accessed March 29, 2018).
- [18] R.S. Pengelly, S.M. Wood, J.W. Milligan, S.T. Sheppard, W.L. Pribble, A Review of GaN on SiC High Electron-Mobility Power Transistors and MMICs, *IEEE Trans. Microw. Theory Tech.* 60 (2012) 1764–1783. doi:10.1109/TMTT.2012.2187535.
- [19] M.A. Sanchez-Garcia, E. Calleja, E. Monroy, F.J. Sanchez, F. Calle, E. Muñoz, R. Beresford, The effect of the III/V ratio and substrate temperature on the morphology and properties of GaN- and AlN-layers grown by molecular beam epitaxy on Si(1 1 1), *J. Cryst. Growth.* 183 (1998) 23–30. doi:10.1016/S0022-0248(97)00386-2.
- [20] M. Yoshizawa, A. Kikuchi, N. Fujita, K. Kushi, H. Sasamoto, K. Kishino, Self-organization of GaN/Al<sub>0.18</sub>Ga<sub>0.82</sub>N multi-layer nano-columns on (0001)

- 
- $\text{Al}_2\text{O}_3$  by RF molecular beam epitaxy for fabricating GaN quantum disks, *J. Cryst. Growth*. 189–190 (1998) 138–141. doi:10.1016/S0022-0248(98)00188-2.
- [21] E. Calleja, M.A. Sánchez-García, F.J. Sánchez, F. Calle, F.B. Naranjo, E. Muñoz, U. Jahn, K. Ploog, Luminescence properties and defects in GaN nanocolumns grown by molecular beam epitaxy, *Phys. Rev. B*. 62 (2000) 16826–16834. doi:10.1103/PhysRevB.62.16826.
- [22] T. Kehagias, G.P. Dimitrakopoulos, P. Becker, J. Kioseoglou, F. Furtmayr, T. Koukoulou, I. Häusler, A. Chernikov, S. Chatterjee, T. Karakostas, H.-M. Solowan, U.T. Schwarz, M. Eickhoff, P. Komninou, Nanostructure and strain in InGaN/GaN superlattices grown in GaN nanowires, *Nanotechnology*. 24 (2013) 435702. doi:10.1088/0957-4484/24/43/435702.
- [23] J. Kioseoglou, T. Pavloudis, T. Kehagias, P. Komninou, T. Karakostas, C.D. Latham, M.J. Rayson, P.R. Briddon, M. Eickhoff, Structural and electronic properties of GaN nanowires with embedded  $\text{In}_x\text{Ga}_{1-x}\text{N}$  nanodisks, *J. Appl. Phys.* 118 (2015) 034301. doi:10.1063/1.4926757.
- [24] S. Strite, H. Morkoc, GaN, AlN, and InN: a review, *J. Vac. Sci. Technol. B*. 10 (1992) 1237–1266. doi:10.1116/1.585897.
- [25] J. Schalwig, G. Müller, O. Ambacher, M. Stutzmann, Group-III-Nitride Based Gas Sensing Devices, *Phys. Status Solidi*. 185 (2001) 39–45. doi:10.1002/1521-396X(200105)185:1<39::AID-PSSA39>3.0.CO;2-G.
- [26] J. Schalwig, G. Müller, M. Eickhoff, O. Ambacher, M. Stutzmann, Group III-nitride-based gas sensors for combustion monitoring, *Mater. Sci. Eng. B*. 93 (2002) 207–214. doi:10.1016/S0921-5107(02)00050-8.
- [27] J. Schalwig, G. Müller, M. Eickhoff, O. Ambacher, M. Stutzmann, Gas sensitive GaN/AlGaN-heterostructures, *Sensors Actuators B Chem.* 87 (2002) 425–430. doi:10.1016/S0925-4005(02)00292-7.
- [28] C. Pfüller, O. Brandt, F. Grosse, T. Flissikowski, C. Chèze, V. Consonni, L. Geelhaar, H.T. Grahn, H. Riechert, Unpinning the Fermi level of GaN nanowires by ultraviolet radiation, *Phys. Rev. B*. 82 (2010) 045320. doi:10.1103/PhysRevB.82.045320.
- [29] G. Müller, J. Schalwig, P. Kreisl, A. Helwig, E. Obermeier, O. Weidemann, M.

- Stutzmann, M. Eickhoff, High-temperature operated field-effect gas sensors, in: C.A. Grimes (Ed.), *Encycl. Sensors*, American Scientific Publishers, Stevenson Ranch, 2006: pp. 1–28.
- [30] J. Teubert, P. Becker, F. Furtmayr, M. Eickhoff, GaN nanodiscs embedded in nanowires as optochemical transducers, *Nanotechnology*. 22 (2011) 275505. doi:10.1088/0957-4484/22/27/275505.
- [31] S. Paul, A. Helwig, G. Müller, F. Furtmayr, J. Teubert, M. Eickhoff, P. Sumit, Optochemical sensor system for the detection of H<sub>2</sub> and hydrocarbons based on InGaN/GaN nanowires, *Sensors Actuators B Chem.* 173 (2012) 120–126. doi:10.1016/j.snb.2012.06.022.
- [32] H. Nojumi, I. Dincer, G. Naterer, Greenhouse gas emissions assessment of hydrogen and kerosene-fueled aircraft propulsion, *Int. J. Hydrogen Energy*. 34 (2009) 1363–1369. doi:10.1016/j.ijhydene.2008.11.017.
- [33] J. Teubert, S. Paul, A. Helwig, G. Müller, M. Eickhoff, Group III-Nitride Chemical nanosensors with optical readout, in: C.-D. Kohl, T. Wagner (Eds.), *Gas Sens. Fundam.*, Springer Berlin Heidelberg, 2014: pp. 311–338. doi:10.1007/5346\_2014\_58.
- [34] I. Lundström, Hydrogen sensitive mos-structures part 1: principle and applications, *Sensors and Actuators*. 1 (1981) 403–426. doi:10.1016/0250-6874(81)80018-2.
- [35] I. Lundström, D. Söderberg, Hydrogen sensitive mos-structures part 2: characterization, *Sensors and Actuators*. 2 (1981) 105–138. doi:10.1016/0250-6874(81)80032-7.
- [36] M. Hübner, C.E. Simion, A. Haensch, N. Barsan, U. Weimar, CO sensing mechanism with WO<sub>3</sub> based gas sensors, *Sensors Actuators B Chem.* 151 (2010) 103–106. doi:10.1016/j.snb.2010.09.040.
- [37] C. Kittel, *Introduction to solid state physics*, Wiley, 2005.
- [38] S.M. Sze, M.-K. Lee, *Semiconductor devices, physics and technology*, 3rd ed., John Wiley & Sons Inc, New York, 2012.
- [39] R.H. Bube, *Photoelectronic Properties of Semiconductors*, Cambridge University Press, 1992.

- 
- [40] J. Piprek, Nitride Semiconductor Devices, WILEY-VCH Verlag, 2007.
- [41] H. Morkoc, Nitride Semiconductor Devices: Fundamentals and Applications, 1st ed., Wiley-VCH, 2013.
- [42] H. Lüth, Solid Surfaces, Interfaces and Thin Films, 5th ed., Springer International Publishing, Cham, 2015. doi:10.1007/978-3-319-10756-1.
- [43] M. Henzler, W. Göpel, Oberflächenphysik des Festkörpers, 2nd ed., Teubner Verlag, Wiesbaden, 1994.
- [44] G.A. Slack, L.J. Schowalter, D. Morelli, J.A. Freitas, Some effects of oxygen impurities on AlN and GaN, J. Cryst. Growth. 246 (2002) 287–298. doi:10.1016/S0022-0248(02)01753-0.
- [45] P. Bogusławski, J. Bernholc, Doping properties of C, Si, and Ge impurities in GaN and AlN, Phys. Rev. B. 56 (1997) 9496–9505. doi:10.1103/PhysRevB.56.9496.
- [46] W. Götz, N.M. Johnson, C. Chen, H. Liu, C. Kuo, W. Imler, Activation energies of Si donors in GaN, Appl. Phys. Lett. 68 (1996). doi:10.1063/1.115805.
- [47] J. Schörmann, P. Hille, M. Schäfer, J. Müßener, P. Becker, P.J. Klar, M. Kleine-Boymann, M. Rohnke, M. de la Mata, J. Arbiol, D.M. Hofmann, J. Teubert, M. Eickhoff, Germanium doping of self-assembled GaN nanowires grown by plasma-assisted molecular beam epitaxy, J. Appl. Phys. 114 (2013) 103505. doi:10.1063/1.4820264.
- [48] P.R. Hageman, W.J. Schaff, J. Janinski, Z. Liliental-Weber, n-type doping of wurtzite GaN with germanium grown with plasma-assisted molecular beam epitaxy, J. Cryst. Growth. 267 (2004) 123–128. doi:10.1016/J.JCRYSGRO.2004.03.024.
- [49] W. Götz, N.M. Johnson, J. Walker, D.P. Bour, R.A. Street, Activation of acceptors in Mg-doped GaN grown by metalorganic chemical vapor deposition, Appl. Phys. Lett. 68 (1996). doi:10.1063/1.116503.
- [50] H. Lu, W.J. Schaff, L.F. Eastman, C.E. Stutz, Surface charge accumulation of InN films grown by molecular-beam epitaxy, Appl. Phys. Lett. 82 (2003) 1736–1738. doi:10.1063/1.1562340.
- [51] L. Colakerol, T.D. Veal, H.-K. Jeong, L. Plucinski, A. DeMasi, T. Learmonth, P.-A.

- Glans, S. Wang, Y. Zhang, L.F.J. Piper, P.H. Jefferson, A. Fedorov, T.-C. Chen, T.D. Moustakas, C.F. McConville, K.E. Smith, Quantized Electron Accumulation States in Indium Nitride Studied by Angle-Resolved Photoemission Spectroscopy, *Phys. Rev. Lett.* 97 (2006) 237601. doi:10.1103/PhysRevLett.97.237601.
- [52] D.A.B. Miller, D.S. Chemla, T.C. Damen, A.C. Gossard, W. Wiegmann, T.H. Wood, C.A. Burrus, Band-Edge Electroabsorption in Quantum Well Structures: The Quantum-Confined Stark Effect, *Phys. Rev. Lett.* 53 (1984) 2173–2176. doi:10.1103/PhysRevLett.53.2173.
- [53] P.D. Yoder, Z. Lochner, R.D. Dupuis, Control of Quantum-Confined Stark Effect in InGaN-Based Quantum Wells, *IEEE J. Sel. Top. Quantum Electron.* 15 (2009) 1080–1091. doi:10.1109/JSTQE.2009.2014170.
- [54] S.M. Sze, K.K. Ng, *Physics of Semiconductor Devices*, John Wiley & Sons, 2006.
- [55] R. Calarco, M. Marso, T. Richter, A.I. Aykanat, R. Meijers, A. V D Hart, T. Stoica, H. Lüth, A. v.d. Hart, T. Stoica, H. Lüth, Size-dependent Photoconductivity in MBE-Grown GaN-Nanowires, *Nano Lett.* 5 (2005) 981–984. doi:10.1021/NL0500306.
- [56] M. Kocan, A. Rizzi, H. Lüth, S. Keller, U.K. Mishra, Surface Potential at as-Grown GaN(0001) MBE Layers, *Phys. Status Solidi.* 234 (2002) 773–777. doi:10.1002/1521-3951(200212)234:3<773::AID-PSSB773>3.0.CO;2-0.
- [57] T. Richter, *Elektrischer Transport in GaN-und InN-Nanodrähten*, RWTH Aachen, 2008. <http://134.130.184.8/opus/volltexte/2009/2662/>.
- [58] T. Wolkenstein, *Electronic Processes on Semiconductor Surfaces during Chemisorption*, Springer US, 1991. doi:10.1007/978-1-4615-3656-7.
- [59] K. Maier, A. Helwig, G. Müller, P. Hille, M. Eickhoff, Effect of Water Vapor and Surface Morphology on the Low Temperature Response of Metal Oxide Semiconductor Gas Sensors, *Materials (Basel).* 8 (2015) 6570–6588. doi:10.3390/ma8095323.
- [60] P. Atkins, J. de Paula, *Atkins' Physical Chemistry*, 8th ed., Oxford University Press, Oxford, 2006.
- [61] I. Langmuir, *The constitution and fundamental properties of solids and liquids.*

- 
- Part I. solids, *J. Am. Chem. Soc.* 38 (1916) 2221–2295. doi:10.1021/ja02268a002.
- [62] C. Kittel, H. Kroemer, *Thermal Physics*, 2nd ed., W. H. Freeman and Company, New York, 1998.
- [63] B. Fultz, *Phase Transitions in Materials*, Cambridge University Press, 2014.
- [64] S. Ahlers, G. Müller, T. Doll, A rate equation approach to the gas sensitivity of thin film metal oxide materials, *Sensors Actuators B Chem.* 107 (2005) 587–599. doi:10.1016/j.snb.2004.11.020.
- [65] C. Oberhüttinger, A. Hackner, G. Müller, M. Stutzmann, On the temperature dependence of the resistive and surface ionisation response of SnO<sub>2</sub> gas sensing layers, *Sensors Actuators B Chem.* 156 (2011) 563–571. doi:10.1016/j.snb.2011.01.069.
- [66] S. Brunauer, P.H. Emmett, E. Teller, Adsorption of Gases in Multimolecular Layers, *J. Am. Chem. Soc.* 60 (1938) 309–319. doi:10.1021/ja01269a023.
- [67] K. Maier, A. Helwig, G. Müller, Room-temperature dosimeter-type gas sensors with periodic reset, *Sensors Actuators B Chem.* 244 (2017) 701–708. doi:http://dx.doi.org/10.1016/j.snb.2016.12.119.
- [68] J. Zhao, L.-H. Huo, S. Gao, H. Zhao, J.-G. Zhao, Alcohols and acetone sensing properties of SnO<sub>2</sub> thin films deposited by dip-coating, *Sensors Actuators B Chem.* 115 (2006) 460–464. doi:10.1016/j.snb.2005.10.024.
- [69] H.C. Wang, Y. Li, M.J. Yang, Fast response thin film SnO<sub>2</sub> gas sensors operating at room temperature, *Sensors Actuators B Chem.* 119 (2006) 380–383. doi:10.1016/j.snb.2005.12.037.
- [70] M. Sucheá, N. Katsarakis, S. Christoulakis, S. Nikolopoulou, G. Kiriakidis, Low temperature indium oxide gas sensors, *Sensors Actuators B Chem.* 118 (2006) 135–141. doi:10.1016/j.snb.2006.04.020.
- [71] A. Helwig, G. Müller, J.A. Garrido, M. Eickhoff, Gas sensing properties of hydrogen-terminated diamond, *Sensors Actuators B Chem.* 133 (2008) 156–165. doi:10.1016/j.snb.2008.02.007.
- [72] S. Beer, A. Helwig, G. Müller, J. Garrido, M. Stutzmann, Water adsorbate

- mediated accumulation gas sensing at hydrogenated diamond surfaces, *Sensors Actuators B Chem.* 181 (2013) 894–903. doi:10.1016/j.snb.2013.02.072.
- [73] M. Hardy, M.D. Doherty, I. Krstev, K. Maier, T. Möller, G. Müller, P. Dawson, Detection of low-concentration contaminants in solution by exploiting chemical derivatization in surface-enhanced Raman spectroscopy., *Anal. Chem.* 86 (2014) 9006–12. doi:10.1021/ac5014095.
- [74] R. Vitushinsky, M. Crego-Calama, S.H. Brongersma, P. Offermans, Enhanced detection of NO<sub>2</sub> with recessed AlGa<sub>N</sub>/Ga<sub>N</sub> open gate structures, *Appl. Phys. Lett.* 102 (2013) 172101. doi:10.1063/1.4803001.
- [75] P. Offermans, R. Vitushinsky, A.D. Fabrication, NO<sub>2</sub> detection with AlGa<sub>N</sub>/Ga<sub>N</sub> 2DEG channels for air quality monitoring, *IEEE Sens. J.* 13 (2013) 2823–2827. doi:10.1109/JSEN.2013.2253767.
- [76] K. Maier, A. Helwig, G. Müller, P. Becker, P. Hille, J. Schörmann, J. Teubert, M. Eickhoff, Detection of oxidising gases using an optochemical sensor system based on Ga<sub>N</sub>/InGa<sub>N</sub> nanowires, *Sensors Actuators B Chem.* 197 (2014) 87–94. doi:10.1016/j.snb.2014.02.002.
- [77] K.P. Galvin, A conceptually simple derivation of the Kelvin equation, *Chem. Eng. Sci.* 60 (2005) 4659–4660. doi:10.1016/j.ces.2005.03.030.
- [78] N.D. Lisgarten, J.R. Sambles, L.M. Skinner, Vapour pressure over curved surfaces-the Kelvin equation, *Contemp. Phys.* 12 (1971) 575–593. doi:10.1080/00107517108205661.
- [79] O. Weidemann, M. Hermann, G. Steinhoff, H. Wingbrant, A. Lloyd Spetz, M. Stutzmann, M. Eickhoff, Influence of surface oxides on hydrogen-sensitive Pd:Ga<sub>N</sub> Schottky diodes, *Appl. Phys. Lett.* 83 (2003) 773. doi:10.1063/1.1593794.
- [80] M. Eickhoff, R. Neuberger, G. Steinhoff, O. Ambacher, G. Müller, M. Stutzmann, Wetting Behaviour of Ga<sub>N</sub> Surfaces with Ga- or N-Face Polarity, *Phys. Status Solidi.* 228 (2001) 519–522. doi:10.1002/1521-3951(200111)228:2<519::AID-PSSB519>3.0.CO;2-A.
- [81] V.M. Bermudez, J.P. Long, Chemisorption of H<sub>2</sub>O on Ga<sub>N</sub>(0001), *Surf. Sci.* 450

- 
- (2000) 98–105. doi:10.1016/S0039-6028(00)00051-0.
- [82] V.M. Bermudez, Study of oxygen chemisorption on the GaN(0001)-(1×1) surface, *J. Appl. Phys.* 80 (1996) 1190. doi:10.1063/1.362924.
- [83] V.M. Gun'ko, Competitive adsorption, *Theor. Exp. Chem.* 43 (2007) 139–183. doi:10.1007/s11237-007-0020-4.
- [84] I. Poplewska, W. Piątkowski, D. Antos, Effect of temperature on competitive adsorption of the solute and the organic solvent in reversed-phase liquid chromatography, *J. Chromatogr. A.* 1103 (2006) 284–295. doi:10.1016/j.chroma.2005.11.038.
- [85] R.J. Martin, K.S. Al-Bahrani, Adsorption studies using gas-liquid chromatography—II. Competitive adsorption, *Water Res.* 11 (1977) 991–999. doi:10.1016/0043-1354(77)90157-9.
- [86] J.M. Jacobson, J.H. Frenz, C.G. Horvath, Measurement of competitive adsorption isotherms by frontal chromatography, *Ind. Eng. Chem. Res.* 26 (1987) 43–50. doi:10.1021/ie00061a009.
- [87] MKS (MKS Instruments Inc.), MKS 179A Datasheet, (2006).
- [88] Linde, Synthetic air specifications, (n.d.). [https://produkte.linde-gase.de/gasgemische/n2o2\\_kw-frei\\_0,20\\_o2\\_n2.html](https://produkte.linde-gase.de/gasgemische/n2o2_kw-frei_0,20_o2_n2.html) (accessed July 15, 2017).
- [89] A. Georgakilas, H.M. Ng, P. Komninou, Plasma-Assisted Molecular Beam Epitaxy of III–V Nitrides, in: *Nitride Semicond.*, Wiley-VCH Verlag GmbH & Co. KGaA, 2006: pp. 107–191. doi:10.1002/3527607641.ch3.
- [90] P.G. Moses, C.G. Van de Walle, Band bowing and band alignment in InGaN alloys, *Appl. Phys. Lett.* 96 (2010) 21903–21908. doi:10.1063/1.3291055.
- [91] Roithner (Roithner Lasertechnik GmbH), UVLED-365-330-SMD datasheet, (2012) 1–7.
- [92] Hamamatsu (Hamamatsu Photonics K.K.), Photosensor Modules H5784 Series datasheet, (1998) 16–17.
- [93] NIST, <http://webbook.nist.gov/cgi/cbook.cgi?ID=C7782447&Mask=20> Oxygen, (n.d.). (accessed April 7, 2014).

- [94] A. Helwig, G. Müller, G. Sberveglieri, G. Faglia, Gas response times of nano-scale SnO<sub>2</sub> gas sensors as determined by the moving gas outlet technique, *Sensors Actuators B Chem.* 126 (2007) 174–180. doi:10.1016/j.snb.2006.11.032.
- [95] A. Helwig, G. Müller, G. Sberveglieri, G. Faglia, Catalytic enhancement of SnO<sub>2</sub> gas sensors as seen by the moving gas outlet method, *Sensors Actuators B Chem.* 130 (2008) 193–199.
- [96] A. Helwig, S. Beer, G. Müller, Breathing mode gas detection, *Sensors Actuators B Chem.* 179 (2013) 131–139. doi:10.1016/j.snb.2012.07.088.
- [97] M. Zheng, G.T. Reader, J.G. Hawley, Diesel engine exhaust gas recirculation—a review on advanced and novel concepts, *Energy Convers. Manag.* 45 (2004) 883–900. doi:10.1016/S0196-8904(03)00194-8.
- [98] K.M. Ervin, J. Ho, W.C. Lineberger, Ultraviolet photoelectron spectrum of nitrite anion, *J. Phys. Chem.* 92 (1988) 5405–5412. doi:10.1021/j100330a017.
- [99] S.E. Novick, P.C. Engelking, P.L. Jones, J.H. Futrell, W.C. Lineberger, Laser photoelectron, photodetachment, and photodestruction spectra of O<sub>3</sub><sup>-</sup>, *J. Chem. Phys.* 70 (1979) 2652–2662. doi:10.1063/1.437842.
- [100] NIST, Electron affinity, (2016). <http://webbook.nist.gov/chemistry/easer.html> (accessed October 10, 2016).
- [101] K. Maier, A. Helwig, G. Müller, P. Hille, J. Teubert, M. Eickhoff, Competitive adsorption of air constituents as observed on InGaN/GaN nano-optical probes, *Sensors Actuators B Chem.* 250 (2017) 91–99. doi:10.1016/j.snb.2017.04.098.
- [102] J. Robertson, Mott lecture: How bonding concepts can help understand amorphous semiconductor behavior, *Phys. Status Solidi.* 213 (2016) 1641–1652. doi:10.1002/pssa.201532875.
- [103] N.F.F. Mott, Electrons in disordered structures, *Adv. Phys.* 16 (1967) 49–144. doi:10.1080/00018736700101265.
- [104] NIST, Chemistry WebBook, (2016). <http://webbook.nist.gov/chemistry/> (accessed November 10, 2016).
- [105] T.-Y. Wu, Electron Affinity of Boron, Carbon, Nitrogen, and Oxygen Atoms, *Phys. Rev.* 100 (1955) 1195–1196. doi:10.1103/PhysRev.100.1195.

- 
- [106] J. Wang, L.S. Pedroza, A. Poissier, M. V. Fernández-Serra, Water Dissociation at the GaN(1010) Surface: Structure, Dynamics and Surface Acidity, *J. Phys. Chem. C*. 116 (2012) 14382–14389. doi:10.1021/jp302793s.
- [107] T. Hisatomi, J. Kubota, K. Domen, Recent advances in semiconductors for photocatalytic and photoelectrochemical water splitting, *Chem. Soc. Rev.* 43 (2014) 7520–7535. doi:10.1039/C3CS60378D.
- [108] D. Wang, A. Pierre, M.G. Kibria, K. Cui, X. Han, K.H. Bevan, H. Guo, S. Paradis, A.-R. Hakima, Z. Mi, Wafer-level photocatalytic water splitting on GaN nanowire arrays grown by molecular beam epitaxy., *Nano Lett.* 11 (2011) 2353–7. doi:10.1021/nl2006802.
- [109] J. Wallys, J. Teubert, F. Furtmayr, D.M. Hofmann, M. Eickhoff, Bias-enhanced optical pH response of group III-nitride nanowires., *Nano Lett.* 12 (2012) 6180–6. doi:10.1021/nl303021v.
- [110] D.K. Pallotti, L. Passoni, F. Gesuele, P. Maddalena, F. Di Fonzo, S. Lettieri, Giant O<sub>2</sub>-Induced Photoluminescence Modulation in Hierarchical Titanium Dioxide Nanostructures, *ACS Sensors*. 2 (2017) 61–68. doi:10.1021/acssensors.6b00432.
- [111] G. Fonrodona, C. Ràfols, E. Bosch, M. Rosés, Autoprotolysis in aqueous organic solvent mixtures. Water/alcohol binary systems, *Anal. Chim. Acta*. 335 (1996) 291–302. doi:10.1016/S0003-2670(96)00329-7.
- [112] K. Maier, A. Helwig, G. Müller, Towards MEMS Pellistor Spectrometers, *Procedia Eng.* 120 (2015) 142–145. doi:10.1016/j.proeng.2015.08.587.
- [113] P. Corfdir, P. Lefebvre, J. Ristić, P. Valvin, E. Calleja, A. Trampert, J.-D. Ganière, B. Deveaud-Plédran, Time-resolved spectroscopy on GaN nanocolumns grown by plasma assisted molecular beam epitaxy on Si substrates, *J. Appl. Phys.* 105 (2009) 013113. doi:10.1063/1.3062742.
- [114] A. Rose, *Concepts in photoconductivity and allied problems*, Wiley, London, 1963.
- [115] M. Hetzl, M. Kraut, T. Hoffmann, J. Winnerl, K. Boos, A. Zeidler, I.D. Sharp, M. Stutzmann, A systematic investigation of radiative recombination in GaN nanowires: The influence of nanowire geometry and environmental

- conditions, *J. Appl. Phys.* 124 (2018) 035704. doi:10.1063/1.5038802.
- [116] S.R. Morrison, *The Chemical Physics of Surfaces*, Springer US, Boston, MA, 1977. doi:10.1007/978-1-4615-8007-2.
- [117] S. Paul, K. Maier, A. Das, F. Furtmayr, A. Helwig, J. Teubert, E. Monroy, G. Müller, M. Eickhoff, III-nitride nanostructures for optical gas detection and pH sensing, in: T. George, M.S. Islam, A.K. Dutta (Eds.), *SPIE Defense, Secur. Sens., International Society for Optics and Photonics*, 2013: p. 87250K. doi:10.1117/12.2015221.
- [118] K. Ihokura, J. Watson, *The Stannic Oxide Gas Sensor Principles and Applications*, CRC Press, Boca Raton, 1994.
- [119] S.M. Summer, *Limiting Oxygen Concentration Required to Inert Jet Fuel Vapors Existing at Reduced Fuel Tank Pressures--final Phase*, Office of Aviation Research, Federal Aviation Administration, 2004.
- [120] J. Schalwig, G. Müller, U. Karrer, M. Eickhoff, O. Ambacher, M. Stutzmann, L. Görgens, G. Dollinger, Hydrogen response mechanism of Pt-GaN Schottky diodes, *Appl. Phys. Lett.* 80 (2002) 1222–1224. doi:10.1063/1.1450044.
- [121] K.I. Lundström, M.S. Shivaraman, C.M. Svensson, A hydrogen-sensitive Pd-gate MOS transistor, *J. Appl. Phys.* 46 (1975) 3876. doi:10.1063/1.322185.
- [122] T. Hübner, L. Boon-Brett, G. Black, U. Banach, Hydrogen sensors – A review, *Sensors Actuators B Chem.* 157 (2011) 329–352. doi:10.1016/j.snb.2011.04.070.
- [123] Pall (Pall Corporation), Supor® R-Membran, (n.d.). <http://www.pall.de/main/OEM-Media-Membranes-and-Materials/product.page?lid=grno5dat> (accessed July 29, 2017).
- [124] G.A. Eiceman, Z. Karpas, *Ion Mobility Spectrometry*, Third Edition, 2nd ed., CRC Press Inc, 2005. <http://www.amazon.de/Ion-Mobility-Spectrometry-With-CDROM/dp/0849322472> (accessed August 23, 2015).

## Danksagung

Ich möchte mich an dieser Stelle bei allen Menschen bedanken, die mich auf dem Weg der Promotion begleitet und unterstützt habe.

Als erstes möchte ich den Beteiligten der Universität Gießen danken: Prof. Martin Eickhoff für die Betreuung der Dissertation und der damit verbundenen tatkräftigen Unterstützung, Inspiration und Diskussion dieser Arbeit und der gemeinsamen Publikationen, die im Rahmen der Promotion entstanden sind. Ich danke den Mitarbeitern des Lehrstuhls: Jörg Teubert, Jörg Schörmann und Pascal Hille und allen die bei der Präparation von Proben und Mitarbeit an Veröffentlichungen beteiligt waren.

Des Weiteren bedanke ich mich bei den Kollegen von Airbus Group Innovations die mich bei der Promotion unterstützt haben: meinem Teamleiter Alois Friedberger der die Rahmenbedingen geschaffen hat diese Arbeit durchzuführen, den Kollegen Angelika Hackner, Johann Göbel, Thomas Ziemann und Wolfgang Legner welche mit ihrer großen Erfahrung oft weitergeholfen haben und Andreas Helwig, der bei vielen Experimenten Tipps und Tricks geben konnte und mich bei den Publikationen unterstützte.

Meinen ganz besonderen Dank gilt Gerhard Müller, der die Arbeit von Airbus Seite betreute. Ohne ihn wäre die Arbeit nicht möglich gewesen und ich danke ihm, dass er sein umfassendes Wissen über die Physik und Gassensorik mit mir teilte um diese Promotion zu ermöglichen.

Zu guter Letzt bedanke ich mich bei meiner Familie und bei allen Freunden, die ich in den letzten Jahren oft vernachlässigen musste.



## Erklärung

Ich erkläre: Ich habe die vorgelegte Dissertation selbstständig und ohne unerlaubte fremde Hilfe und nur mit den Hilfen angefertigt, die ich in der Dissertation angegeben habe. Alle Textstellen, die wörtlich oder sinngemäß aus veröffentlichten Schriften entnommen sind, und alle Angaben, die auf mündlichen Auskünften beruhen, sind als solche kenntlich gemacht. Ich stimme einer evtl. Überprüfung meiner Dissertation durch eine Antiplagiat-Software zu. Bei den von mir durchgeführten und in der Dissertation erwähnten Untersuchungen habe ich die Grundsätze guter wissenschaftlicher Praxis, wie sie in der „Satzung der Justus-Liebig-Universität Gießen zur Sicherung guter wissenschaftlicher Praxis“ niedergelegt sind, eingehalten.

---

Ort Datum

---

Konrad Maier